Karlsruher Institut für Technologie

TECHNISCHE UNIVERSITÄT DARMSTADT

Atomic Structure and Structural Stability of $Fe_{90}Sc_{10}$ Nanoglasses

Vom Fachbereich Material- und Geowissenschaften
der Technischen Universität Darmstadt

zur Erlangung des akademischen Titels
Doktor-Rerum-Naturalium (Dr. rer. nat.)

genehmigte Dissertation von
M.Sc. Chaomin Wang
geboren am 21. September 1986 in Anhui, China

1. Prüfer: Prof. Dr. -Ing. Horst Hahn
2. Prüfer: Prof. Dr. rer. nat. Karsten Albe

Tag der Einreichung: 22.08.2017
Tag der mündlichen Prüfung: 15.11.2017

Darmstadt 2017
D17

Atomic Structure and Structural Stability of $Fe_{90}Sc_{10}$ Nanoglasses
Chaomin Wang
Darmstadt, Techn. Univ., Diss., 2014
D 17

Erklärung zur Dissertation

Hiermit versichere ich, dass ich meine Dissertation selbständig und nur mit den angegebenen Quellen und Hilfsmitteln angefertigt habe. Diese Arbeit hat in gleicher oder ähnlicher Form noch keiner Prüfungsbehörde vorgelegen.

Darmstadt, den Datum

Chaomin Wang 21-08-2017

(Chaomin Wang)

Abstract

Nanoglasses are non-crystalline solids whose internal structure is characterized by fluctuations of the free volume. Due to the typical dimensions of the structural features in the nanometer-range and the disordered atomic structure of the interfacial regions, the atomic structure and the structural stability of nanoglasses is not yet completely understood.

Nanoglasses are typically produced by consolidation of glassy nanoparticles. Consequently, the basis for the understanding of the atomic structure of nanoglasses lies in the atomic structure of the primary glassy nanoparticles.

Using electron energy loss spectroscopy, the elemental distribution in the $Fe_{90}Sc_{10}$ primary glassy nanoparticles and in the corresponding nanoglasses produced by consolidation of these glassy nanoparticles have been studied. Due to surface segregation, Fe has been found to be enriched at the surface of the primary $Fe_{90}Sc_{10}$ glassy nanoparticles. This behavior was found to be consistent with theoretical results based on a monolayer model for surface segregation behavior of the binary liquid alloys. In addition, the heterogeneous structure of $Fe_{90}Sc_{10}$ nanoglasses with Fe enriched interfaces was also directly observed, and may be attributed to the segregation of the primary glassy nanoparticles on the surface.

Furthermore, the electron density of the isolated and loosely compacted primary glassy nanoparticles was investigated using small- and wide- angle X-ray scattering. The results indicate that the surface shells of glassy nanoparticles have an electron density that is lower than the electron density in the cores of the glassy nanoparticles. The lower electron density seems to result mainly from a lower atomic packing density of the surface shells rather than from compositional variations due to the surface segregation.

During the consolidation of the glassy nanoparticles, the inhomogeneous elemental distribution and the short-range order in the shells of $Fe_{90}Sc_{10}$ glassy nanoparticles can be transferred into the interfaces of the resulting bulk $Fe_{90}Sc_{10}$ nanoglasses. The free volume within the shells of the $Fe_{90}Sc_{10}$ glassy nanoparticles may delocalize into the interfaces between the $Fe_{90}Sc_{10}$ glassy nanoparticles resulting in interfacial regions of lower atomic packing density in the $Fe_{90}Sc_{10}$ nanoglasses.

The structural stability of $Fe_{90}Sc_{10}$ nanoglasses has been studied by means of low temperature annealing *in situ* in a transmission electron microscope, and *ex situ* in an ultra-high-vacuum tube-furnace. The analysis of both experiments showed similar results. The structure of the $Fe_{90}Sc_{10}$ nanoglasses was stable for up to 2 hours when annealed at 150 °C. Annealing of nanoglasses at higher temperatures resulted in the formation of a metastable nanocrystalline bcc-Fe(Sc) with Sc-enriched interfaces. The crystallization process of $Fe_{90}Sc_{10}$ nanoglasses was clarified and a plausible mechanism for the structural stability was proposed.

Abstrakt

Nanogläser sind nichtkristalline Festkörper, deren innere Struktur durch Schwankungen des freien Volumens gekennzeichnet ist. Aufgrund der typischen Dimensionen der Strukturmerkmale im Nanometerbereich und der ungeordneten Atomstruktur der Grenzflächenbereiche sind die atomare Struktur und die strukturelle Stabilität von Nanogläsern noch nicht vollständig verstanden.

Nanogläser werden typischerweise durch das Zusammenpressen von amorphen Nanopartikeln hergestellt. Folglich liegt die Grundlage für das Verständnis der atomaren Struktur vom Nanogläsern in der atomaren Struktur der primären amorphen Nanopartikel.

Mithilfe der Elektronenenergieverlustspektroskopie (Electron Energy Loss Spectroscopy – EELS) wurde die Elementverteilung in den primären amorphen Nanopartikeln $Fe_{90}Sc_{10}$ und im entsprechenden Nanogläser, das durch Konsolidierung dieser amorphen Nanopartikel hergestellt wurde, untersucht. Es wurde festgestellt, dass Fe an der Oberfläche der primären $Fe_{90}Sc_{10}$-Glasnanopartikel angereichert ist und Oberflächensegregationen bildet. Dieses Verhalten wurde mit theoretischen Ergebnissen begründet, die auf einem Monoschichtmodell für das Oberflächensegregationsverhalten der binären flüssigen Legierungen beruhen. Darüber hinaus wurde die heterogene Struktur der $Fe_{90}Sc_{10}$-Nanogläser mit Fe-reichen Grenzflächen ebenfalls direkt beobachtet und der Eisensegregation auf der Oberfläche der primären glasartigen Nanopartikel zugeschrieben.

Außerdem wurde die Elektronendichte der isolierten und locker verdichteten primären amorphen Nanopartikel mittels Klein- und Weitwinkelröntgenstreuung untersucht. Die Ergebnisse zeigen, dass die Oberflächen von amorphen Nanopartikeln eine Elektronendichte aufweisen, die niedriger als die Elektronendichte in den inneren Bereichen der Nanopartikel ist. Die niedrigere Elektronendichte scheint hauptsächlich aus einer niedrigeren Atompackungsdichte der Oberflächenschalen zu resultieren, als aus Zusammensetzungsvariationen aufgrund der Oberflächensegregation.

Während des Konsolidierens der amorphen Nanopartikel kann die inhomogene Elementverteilung und die Nahordnung in den Oberflächenbereichen von $Fe_{90}Sc_{10}$-amorphen Nanopartikeln in die Grenzflächen der resultierenden $Fe_{90}Sc_{10}$-Nanogläser übertragen werden. Das freie Volumen innerhalb der Oberflächenbereichen der $Fe_{90}Sc_{10}$-Glasnanopartikel kann in die Grenzflächen zwischen den $Fe_{90}Sc_{10}$-Glasnanopartikeln delokalisieren, was zu Grenzflächenbereichen mit geringerer Atompackungsdichte in den $Fe_{90}Sc_{10}$-Nanogläsern führt.

Die strukturelle Stabilität der $Fe_{90}Sc_{10}$-Nanogläser wurde durch Aufheizen/Anlassen in situ in einem Transmissionselektronenmikroskop und ex situ in einem Ultrahochvakuum-Röhrenofen untersucht. Die Analyse beider Experimente zeigte vergleichbare Ergebnisse. Die Mikrostruktur der $Fe_{90}Sc_{10}$-Nanogläser war bis zu 2 Stunden stabil, wenn sie bei 150 °C getempert/angelassen wurden. Das Tempern/Anlassen der Nanogläser bei höheren Temperaturen führte zur Bildung von metastabilem nanokristallinen bcc-Fe (Sc) mit Sc-reichen

Grenzflächen. Der Kristallisationsprozess von $Fe_{90}Sc_{10}$-Nanogläsern wurde aufgeklärt und ein plausibler Mechanismus für die strukturelle Stabilität wurde vorgeschlagen.

Acknowledgements

At the beginning, I would like to thank ***my parents*** who gave me the life, the encouragements and the supports to finish this thesis. Then I would like to express my gratitude to ***everyone who supported me during my Ph.D study***, and some special acknowledgements go to the persons as follows.

I sincerely thank my supervisor ***Prof. Dr. -Ing. Horst Hahn*** for supervising this thesis and supporting a good platform for me to obtain my degree. Without his constant guidance and suggestions, this thesis could not be finished as its present form.

Without ***Prof. Dr. Dr. h. c. Herbert Gleiter***'s introduction, I would never have the chance to do the research of nanoglasses. As a co-supervisor, his help, guidance and encouragements will be kept in my memory forever.

Dr. Yulia Ivanisenko's assistance and encouragements once helped me to pass the hard time during my study.

Dr. Di Wang and ***Dr. Xiaoke Mu*** helped me to do a lot of the TEM measurements, and ***Dr. Xiaoai Guo*** helped me to do the SAXS measurements. Without these three persons' work, I could not collect enough experimental results for the present dissertation.

I thank ***Dr. Tao Feng*** for introducing me to the IGC system and some characterization methods during my first year study.

My colleagues ***Dr. Askar Kilmametov*** and ***M. Sc. Sree Harsha Nandam*** are greatly appreciated for their many years' constant help and for sharing their happiness with me.

Mr. Martin Limbach as a lab technician helped me a lot to solve the technical problems.

Dr. Mohammad Ghafari fitted the Mössbauer spectra for me, and the fruitful discussion with him at Herbert Gleiter Institute of Nanoscience (HGI) helped me to finish this thesis easier. ***Dr. Ralf Witte*** helped me to do the Mössbauer measurements and also gave me many other assistance during my study in Institute for Nanotechnology (INT) of Karlsruhe Institute of Technology (KIT).

Dr. Sunkulp Goel who helped me to check the written English of my papers, and shared his apartment with me when I was in HGI.

Furthermore, ***Dr. Haiping Wang***, ***Dr. Renjun Du***, ***Dr. Suresh Kumar Garlapati***, ***Dr. Na Chen***, ***Dr. Zhirong Zhao-Karger***, ***Dr. Mithun Palit***, ***Dr. Robert Kruk***, ***Dr. Aaron Kobler***, ***Dr. Christian Kübel***, ***Dr. Guo Peng***, ***M. Sc. Bing Wu***, ***Miss Yini Fang***, ***M. Sc. Ming Sun***, ***Miss Chunyu Guo***, ***Dr. Liran Wang***, ***Dr. Quan Shi***, ***Mr. Pierre Denis***, ***Dr. Aline Leon***, ***Dr. Si Lan and Dr. Baoan Sun*** are all appreciated for their more or less assistance in sample preparation, measurements and/or discussion.

Mrs. Birgit Limmer and some other ***secretaries and managers from INT***, ***TU Darmstadt***, ***HGI*** are all acknowledged.

My relatives and friends, ***Hahn group in INT***, ***some technicians of INT (include the workshop and many cooperators from other groups)***, though some of their names are not listed here but their kindly help will be memorized forever.

At last, I gratefully acknowledge ***China Scholarship Council (CSC)*** and ***Chinese embassy in Frankfurt*** for supporting my study in Germany. In addition, half year scholarship supported by ***TU Darmstadt*** and half year scholarship supported by ***HGI*** are both acknowledged.

Table of Contents

List of Figures

List of Abbreviations

APD	Atomic packing density
CSRO	Chemical short-range order
CN	Coordination number
ED	Electron diffraction
EELS	Electron energy loss spectroscopy
EFTEM	Energy-filtered transmission electron microscopy
EXAFS	Extended X-ray absorption fine structure
EDX	Energy dispersive X-ray spectroscopy
FIB	Focused ion beam
G	Gibbs free energy
GNp	Glassy nanoparticles
HAADF	High angle annular dark field
HRTEM	High resolution transmission electron microscopy
IGC	Inert gas condensation
IS	Isomer shift
K	Kelvin
MG	Metallic glass
MRO	Medium-range order
MS	Mössbauer spectroscopy
MQR	Melt-quenched ribbon
NG	Nanoglass
Pa	Pascal
PAS	Positron annihilation spectroscopy
PVD	Physical vapor deposited
PDF	Pair distribution function
QS	Quadrupole splitting
R	Gas constant
RDF	Radial distribution function
SRO	Short-range order
SAXS	Small-angle X-ray scattering
STEM	Scanning transmission electron microscopy
SEM	Scanning electron microscopy

SPD	Severe plastic deformation
SSSS	Supersaturated solid solution
TSRO	Topological short-range order
TEM	Transmission electron microscopy
Tg	Glass transition temperature
UHV	Ultra-high vacuum
WAXS	Wide-angle X-ray scattering
XRD	X-ray diffraction
XANES	X-ray absorption near edge structure
X_{Fe}	Atomic fraction of the iron
bcc	Body centered cubic
q	Scattering vector
ps	Picosecond
min	Minutes
ΔH	Heat of mixing
ΔS	Entropy of mixing
°C	Degree centigrade

Motivation

Recently, a new class of nanostructured materials, has been produced by consolidation of glassy nanoparticles (GNp) into bulk materials, called nanoglasses (NGs) [1-5]. The available data suggest that the structure of NGs consists of nanometer-sized glassy regions of high density separated by interfacial regions (interfaces) of reduced density [6, 7].

The fact that NGs exhibit interesting new properties, which differ from those of the primary GNp and the corresponding melt-quenched glasses with the identical average chemical composition, has been attributed primarily to the enhanced free volume and the difference in the short-range order (SRO) within the interfaces compared to those of the adjacent glassy regions [4, 5].

Due to the significant role of the interfaces within NGs, several experimental studies and computer simulations have been conducted to investigate their atomic structure [6, 8-12]. However, it is very difficult to characterize the interfacial structure of NGs in detail due to the characteristic dimensions in the nanometer-range and their disordered atomic structure. Thus, the limited knowledge of the atomic structure of NGs and the difficulties of the structural characterization prompted us to explore some new routes to characterize their structure.

Since the interfaces of NGs are generated during the consolidation of the primary GNp, it can be expected that some features of the GNp, such as the chemical composition and the types of SRO, may be transferred into the interfaces of the NGs. Accordingly, acquiring knowledge of the atomic structure of the primary GNp is required to improve our understanding of the atomic structure of NGs.

In addition, the knowledge of the relationship between the structure of the primary GNp and that of the NG will help to design NG with desired properties. Taking Fe-M (M represents a metallic or metalloid element) metallic glasses (MGs) as an example, due to surface segregation, the concentration of M on the surfaces of the primary Fe-M GNp should be different from that of the cores. Thus, after consolidation, the M content of the surfaces is transferred into the interfaces within the Fe-M NGs. Supposing the magnetic property of the Fe-M MGs is closely related to the concentration of M, the magnetic property of the interfaces within the NGs should be different from the cores due to their different composition. As the surface segregation behavior of the primary Fe-M GNp can also be predicted using thermodynamics, the chemical composition of the interfaces can be designed according to the theoretical predication, which also implies that the magnetic property of the NGs can be designed.

Consequently, in order to improve the understanding of the atomic structure of the interfaces within NG, the atomic structure of the primary $Fe_{90}Sc_{10}$ GNp should be studied. In combination with the available studies of the structure of $Fe_{90}Sc_{10}$ NG, a modified structure model for the $Fe_{90}Sc_{10}$ NG can be proposed.

Since the properties of materials are determined by the atomic structure and the microstructure, it is important to know the structural stability of materials. For NGs, several computer simulations have been performed to investigate their structural stability [9-11]. For example, Albe et al. simulated the structural evolution of Cu-Zr NG during annealing [9], and found that the free volume within the interfaces of the as-prepared NG can delocalize, so that the volume fraction of the interfaces increases. Due to this delocalization process, the free volume localized initially in the interfaces can spread out over the entire NG sample, resulting in a structure of nearly homogeneous density distribution [9].

Fang et al. performed in-situ small- and wide- angle X-ray scattering (SAXS/WAXS) and positron annihilation spectroscopy (PAS) measurements to analyze the structural evolution of $Sc_{75}Fe_{25}$ NG as a function of time and temperature [6]. They reported the growth of the interfacial width to cease after some annealing time, and hence the formation of glasses with a homogeneous density as predicted by the computer simulation was not observed.

From a different perspective, if the nanometer-sized density fluctuations are taken as one feature of NG, then the enhanced free volume within the interfaces cannot spread out over the entire sample, which implies that the NG structure is quite stable. Nevertheless, the discrepancy between Fang's experimental results and Albe's computer simulation results indicates that the structural stability of NG is still not completed understood. In addition, since the structure of the interfaces is difficult to be characterized in detail, experimental results alone are still not enough for us to draw a conclusion about the structural stability of NG.

Accordingly, in order to enrich the evidence and understand the underlying mechanism for the structural stability of NG, in this thesis project, the structural stability of $Fe_{90}Sc_{10}$ NG was investigated by some new techniques, viz., Mössbauer spectroscopy (MS), scanning transmission electron microscopy (STEM), and electron diffraction (ED).

1 Introduction and Literature Review

1.1 The concepts of metallic glasses and nanoglasses

Traditional metallic materials are crystalline solids that are cooled from liquid into an ordered atomic structure. However, MGs are non-crystalline metallic solids that are formed by continuous cooling from the liquid state. Metallic glasses are in a metastable state, and after crystallization they can be transferred into a stable state with an ordered atomic structure [13, 14].

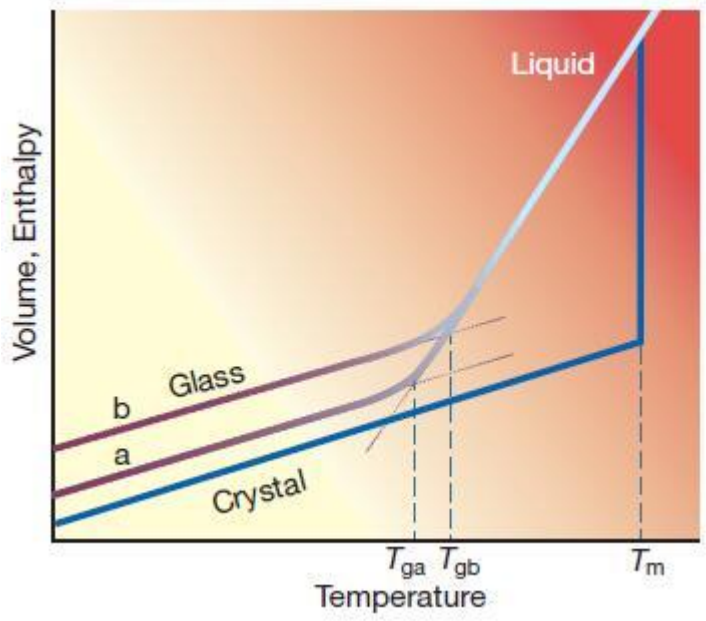

Figure 1-1. Variation of specific volume and enthalpy with temperature for a normal and a glass-forming material both cooled from the liquid. [15]

The variation of the specific volume and enthalpy versus the temperature is shown in Fig. 1-1. When the temperature rises above the melting point (T_m) of the alloys, the volume and enthalpy of the liquid alloys decreases along with the temperature. When the temperature reaches the melting point, there are two possible structural states for the liquid alloys. The alloys can either crystallize when the specific volume drops resulting in the formation of a solid alloy, or if they continue to cool, where the specific volume will decrease until some temperature, resulting in undercooled liquid alloys. At this temperature, the supercooled liquid alloy is "frozen in" with high viscosity, which is referred to as glass. This temperature is traditionally referred to as the "glass

transition" temperature, or T_g [15]. The T_g value is dependent on factors such as the cooling rate and the magnitude of the undercooling, see Fig. 1-1.

Metallic glasses are considered to be good candidates within structural applications due to their excellent mechanical properties including high strength and hardness. However, MGs do not exhibit good plastic behavior like crystalline metallic materials such as nucleation and moving dislocation under yielding because the tight atomic packing structure cannot dislocate. Consequently, MGs tend to fail catastrophically after yielding by presenting a few large, but thin shear bands and exhibit brittle behavior similar to traditional glasses [16-18]. Researchers have been looking to improve the brittleness of MGs, however, the plasticity and ductility remains insufficient.

According to the classic "free volume" [19-21] and ''shear transition zone'' [22] mechanisms for the plastic deformation behavior of MGs, creating more free volume or increasing the density fluctuations in MGs could improve the plasticity. For instance, increasing the cooling rate in solidification of MGs could increase the free volume, thus enhancing the ductility [19, 21]. In pre-deformed MGs, multiple small shear bands with enhanced free volume could act as a shear transition zone to allow the material to yield and to impede the propagation of the big shear bands, resulting in improved plasticity for the MGs [23, 24].

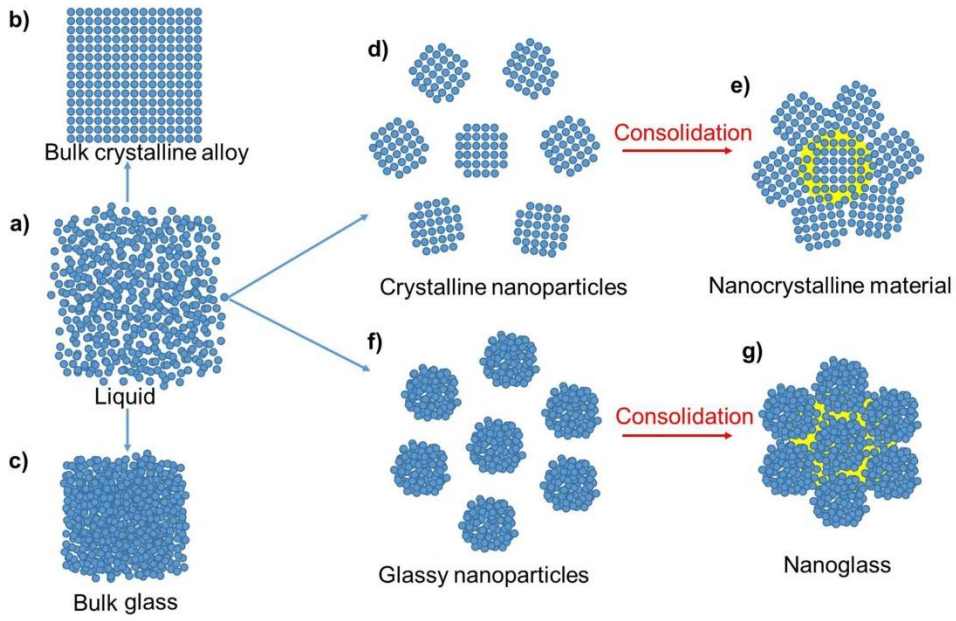

Figure 1-2. Structural comparison between the atomic structure of nanoglass and nanocrystalline materials. (a) Liquid alloy, (b) bulk crystalline alloy, (c) bulk glass, (d) crystalline nanoparticles, (e) nanocrystalline materials, (f) glassy nanoparticles, (g) nanoglass.

To introduce more free volume and interfaces into the MGs to improve the properties, a new method for producing novel MGs via consolidation of the GNp into a bulk solid material as NG was proposed by Gleiter and his colleagues in 1989 [25]. Recent molecular dynamic simulations and experimental results indicated that

the plasticity and ductility of the NGs are superior to the MGs counterparts, since the interfaces exhibit similar functions such as multiple small shear bands in pre-deformed MGs [6, 23, 26, 27].

In general, NGs are nanostructured MGs consisting of glassy nanometer-sized cores connected by interfaces having enhanced free volume. As shown in Fig. 1-2, the atomic structural feature of nanoglasses (NGs) is a combination of the atomic structural features of nanocrystalline materials and normal glasses. Nanocrystalline material is prepared by consolidating the crystalline nanoparticles into a bulk material. This is different from NG, which is prepared by consolidating the glassy nanoparticles. When compared to the normal glass, NG contains a large amount of interfaces with enhanced free volume. NG can be either non-metallic or metallic glassy materials, however in the current study NG are only referred to as metallic glassy materials.

1.2 Free volume and short-range order in metallic glasses

Understanding the atomic structure of MGs is important for the improvement of MGs, to understand the intrinsic questions of glasses (such as the mystery of the glass transition), as well as to produce NGs with superior properties than the corresponding MGs.

Considering the atomic structure of MGs, two important concepts will be described: the "free volume" and the "short-range order" (SRO), which are frequently used in this thesis.

The concept of free volume was brought forth by Cohen and Turnbull [28-30], and was later improved by Cohen and Grest [31]. These concepts were used to explain the variations of physical properties that are near the glass transition, such as the specific heat, thermal expansion, and viscosity [28-31].

As shown in Fig. 1-3a, an atom (black sphere) is trapped in the cage that is formed by its neighbors, where V_a is the volume of an atom, V_c is the volume of the cage. Free volume is defined as $V_f = V_c - V_a$. Due to the confinement of the cage, the black atom cannot move freely, and most of the time its movement is backscattered by its neighboring atoms. However, free volume can be redistributed between the neighboring cages without consuming local free energy, thus when there is enough empty space (larger than V_c) next to the atom, such as the vacant site shown in Fig. 1-3b, the atom can move freely into the empty space [31].

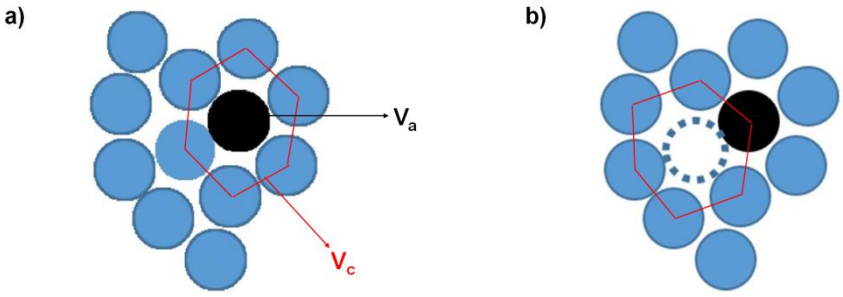

Figure 1-3. Schematic drawing of the free volume model, which was proposed by Cohen et al. V_a is the volume of an atom, V_c is the volume of the cage, free volume is defined as the difference between the V_c and V_a. (a) The motion of the black atom is restricted by the cage. (b) The black atom can freely move into the circle place which was redistributed of the free volume. [31]

The free volume model is intuitive, and it can be used to explain various thermodynamic behaviors of the MGs, however, it does not explain any local atomic structural information of MGs. In order to understand the atomic packing behavior of liquids and MGs, the atomic structures of glass are assigned into three groups first, i.e., the SRO with a range smaller than 0.5 nm, medium range order (MRO) ranging from 0.5 nm to 2 nm, and

the long-range disorder beyond 2 nm [32]. Metallic glasses are categorized as long-range disordered metallic alloys, but they have short- or medium- range ordered structure.

The SRO include chemical SRO (CSRO) and topological SRO (TSRO) [33]. Since MGs are typically prepared by the rapid-quenched method, it is reasonable to assume that a totally homogenous distribution of components is not achievable. Therefore, the chemical compositions of certain local parts of MG are different from the average composition. The variation in chemical composition is referred to as different CSRO. The TSRO can be considered as a different configuration of the atoms. For instance, we can say diamond and graphite have different TSRO though carbon atoms construct them both.

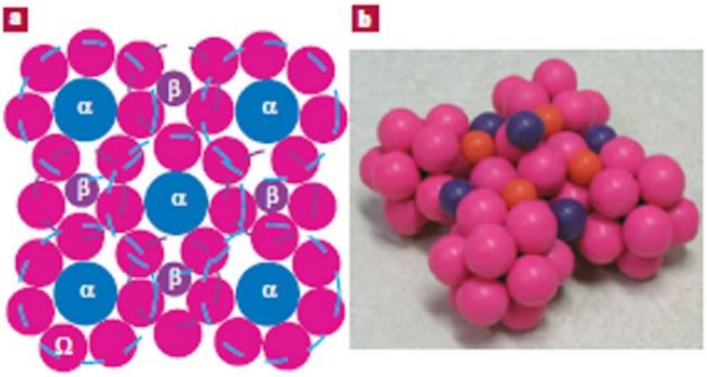

Figure 1-4. Single cluster unit cell for the dense cluster-packing model. (a) A two-dimensional representation of a dense cluster-packing structure; α and β spheres represent the solute atoms, which are surrounding the solvent atoms (red spheres), and the blue dashed circles represent the clusters. (b) A portion of a cluster unit cell of a Zr-(Al,Ti)-(Cu,Ni)-Be alloy that were packed plastic spheres. [34]

Miracle et al. [34] investigated the atomic structure of MGs by densely packing plastic spheres, and proposed a dense cluster-packing model for MGs. As shown in Fig. 1-4, the MG are overlapping in the dense solute-centered clusters [34, 35]. These clusters contain solvent atoms only in the first coordination shell and share their face, edge, or vertex with the adjacent clusters. The candidate cluster configurations in the MG are summarized in Fig. 1-5 [36]. The characteristic and occurrence of these clusters are typically determined by the atomic size ratio between the solute and the solvent atoms.

Building on Miracle's work, Ma et al. [37] studied the atomic structure of MG using experimental and computational techniques, and suggested that the main underlying TSRO in MG is Kasper polyhedra. The Kasper polyhedra are attracted to the adjacent polyhedra with a shared face, edge, or vertex to form the "quasi-equivalent" icosahedral clusters (Fig. 1-6). These icosahedral clusters are the dominant medium-range order (MRO) of MG.

Chen et al. [38, 39] used coherent nanobeam ED to achieve real-space observation of SRO and MRO. In combination with the ab initio molecular dynamics simulation, the structures and assemblies of clusters, which are consistent with Miracle and Ma's cluster models, can be obtained. Note that although some knowledge of the MRO have been gained, the MRO of the MGs are still not completely understood, due to the complex

structure of MGs and the difficulties of structural characterization. Thus, the atomic packing behavior of MG needs to be further investigated.

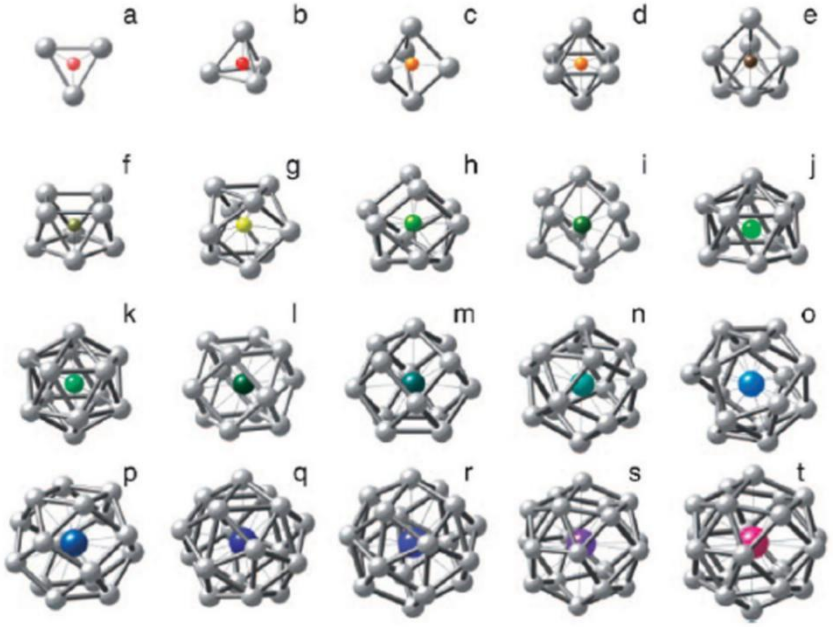

Figure 1-5. Atomic structural models of solute-centered clusters. [36]

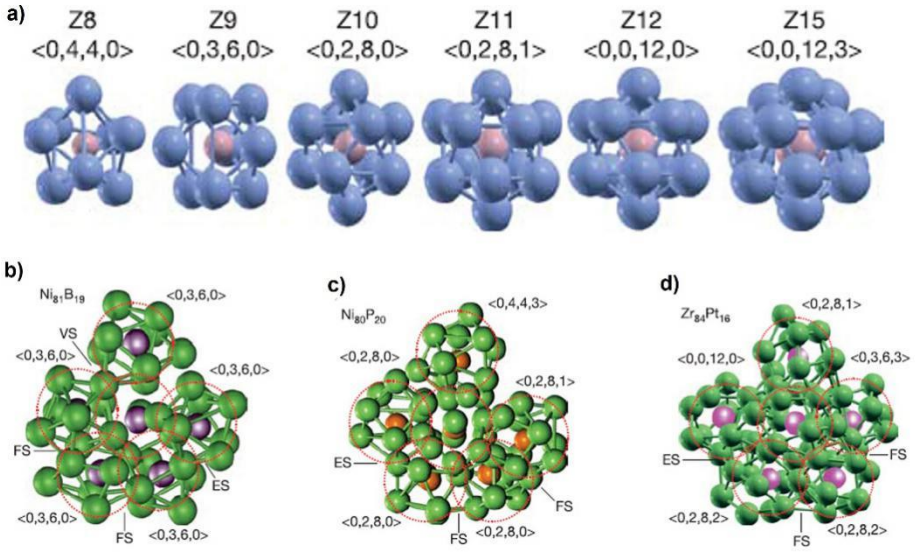

Figure 1-6. TSRO and MRO in MG. (a) Kasper polyhedra (TSRO) with different coordination numbers (CNs), and the Voronoi index are given to indicate their identities. (b), (c) and (d) are the MRO (icosahedral clusters) of the $Ni_{81}B_{19}$, $Ni_{80}P_{20}$, $Zr_{84}Pt_{16}$ MGs, respectively. VS, ES and FS are referred to as vertex-sharing, edge-sharing and face-sharing, respectively. The red dashed circles denote the Kasper polyhedra (TSRO), these Kasper polyhedral are packed into quasi-equivalent icosahedral clusters (MRO). [37]

1.3 State of the art

1.3.1 Synthesis and properties of nanoglasses

Recall that for the purposes of this study, NGs are only referred to as bulk non-crystalline materials that are prepared by consolidating non-crystalline nanoparticles at high pressures. Researchers commonly report producing other non-crystalline solids with density fluctuation, which were also referred to as "NGs". To clarify the differences between these other NGs, and the ones in the current study, this section will give a brief review of the synthesis and properties of different NGs.

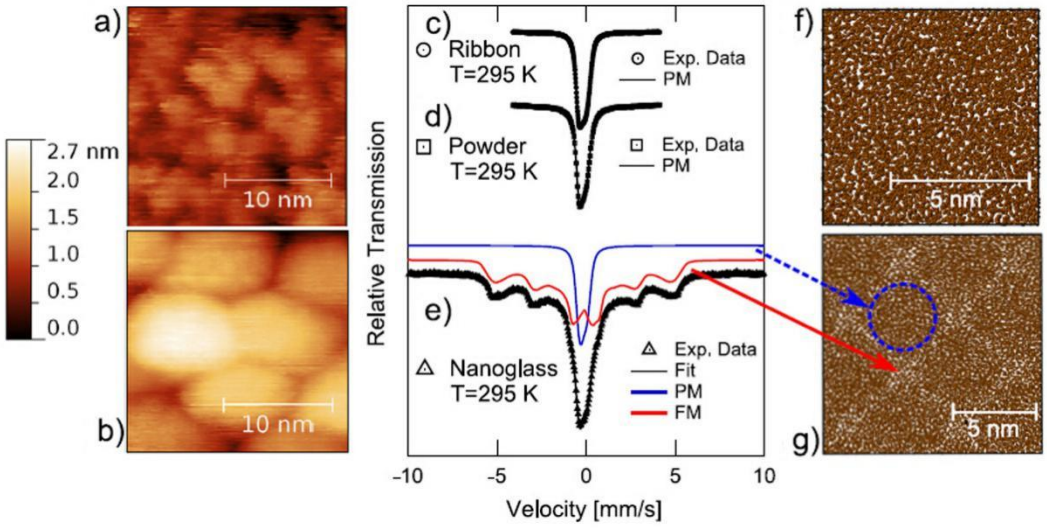

Figure 1-7. Constant current scanning tunnel microscopy images of the polished surfaces of $Fe_{90}Sc_{10}$ MQR (a), and $Fe_{90}Sc_{10}$ NG (b). Room temperature MS spectra of the $Fe_{90}Sc_{10}$ MQR (c), the primary $Fe_{90}Sc_{10}$ GNp (d), and the $Fe_{90}Sc_{10}$ NG (e). The red six-line curve represents the ferromagnetic interfaces while the blue single-peak curve represents the interior-cores of NG. Molecular dynamics simulated structures of melt-quenched Ge glass (f) and Ge NG (g). [7]

The classic and most common approach in NG preparation is consolidation of non-crystalline nanoparticles into bulk materials. For this approach, various non-crystalline nanoparticles can be prepared by physical and chemical methods, such as the inert gas condensation (IGC), ball milling, and solution precipitation [40]. The IGC method [41] was used to synthesize the crystalline nanoparticles, and is considered the best way to prepare ultra-fine, contamination free, and narrow-size distributed metallic GNp. Since these metallic GNp are

consolidated in-situ in the ultra-high vacuum (UHV) chamber of the IGC apparatus, clean interfaces, without oxide or absorbed gas, porosity-free metallic NGs are obtained.

Figures 1-7a and 1-7b display the morphologies of the polished surfaces of the $Fe_{90}Sc_{10}$ melt-quenched ribbon (MQR) and the $Fe_{90}Sc_{10}$ NG [7]. Compared to the MQR sample, $Fe_{90}Sc_{10}$ NG sample prepared by consolidating the GNp clearly exhibit a nano-granular structure with a typically size of the "nano-grains" of about 10 nm. These "nano-grains" are considered to be the core of the $Fe_{90}Sc_{10}$ NG, and the "grain boundaries" may indicate the presence of low density interfaces. Mössbauer spectra (Figs. 1-7c, d, e) shows that the interfaces are ferromagnetic at room temperature, yet the cores are paramagnetic like the primary isolated $Fe_{90}Sc_{10}$ GNp and the MQR of similar composition. Moreover, over the entire compositional range in the Fe-Sc magnetic phase diagram, no room temperature ferromagnetic phase exists for MQR samples [42]. This indicates that a truly novel amorphous structure is present in the interfacial regions. Accordingly, due to the presence of large amounts of the interfaces with novel atomic structure, the consolidated NGs exhibit better mechanical properties than the corresponding MGs with the identical composition [6, 26, 27, 43-52].

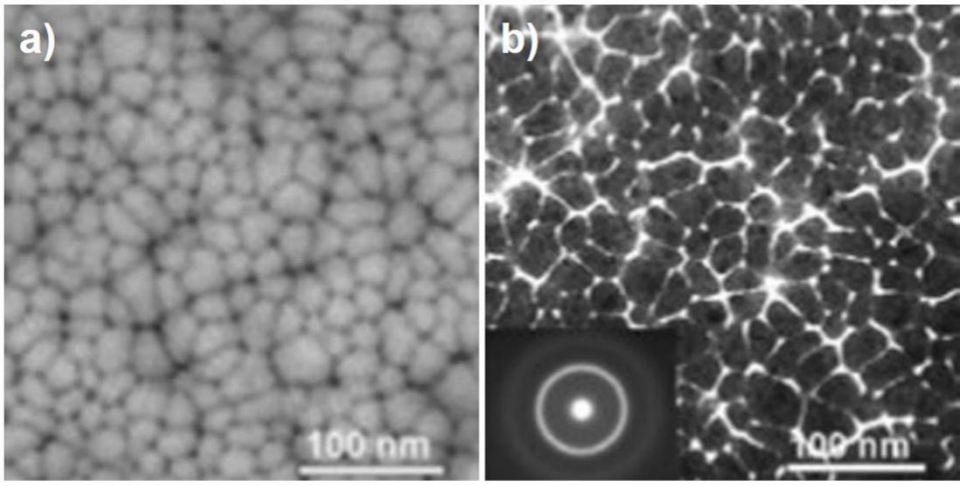

Figure 1-8. Surface morphology of the $Au_{49}Ag_{5.5}Pd_{2.3}Cu_{26.9}Si_{16.3}$ NG thin film produced by magnetron sputtering. a) SEM image, b) TEM image, the insert shows the ED pattern. [53]

Figure 1-8 depicts typical SEM and TEM images of the surface morphology of the NG thin film, which was produced by Chen et al. using magnetron sputtering [53]. It is seen that the $Au_{49}Ag_{5.5}Pd_{2.3}Cu_{26.9}Si_{16.3}$ NG thin film consists of "nano-grains" of about 30 nm, connected by lower density interfaces. Śniadecki et al. produced $Ni_{50}Ti_{45}Cu_5$ NG thick films by using a similar method as Chen, however, $Ni_{50}Ti_{45}Cu_5$ NG thick film shows a different hierarchical nano-columnar structure (Fig. 1-9a) from nano-grain structure [54]. This indicates that the "nano-grain" structure may be present only in very thin films. The average diameter of the columns was about 8 nm, and the elemental maps of Ni and Ti indicate that the Ni-rich columns connect through the Ti-rich interfacial regions (Fig. 1-9b).

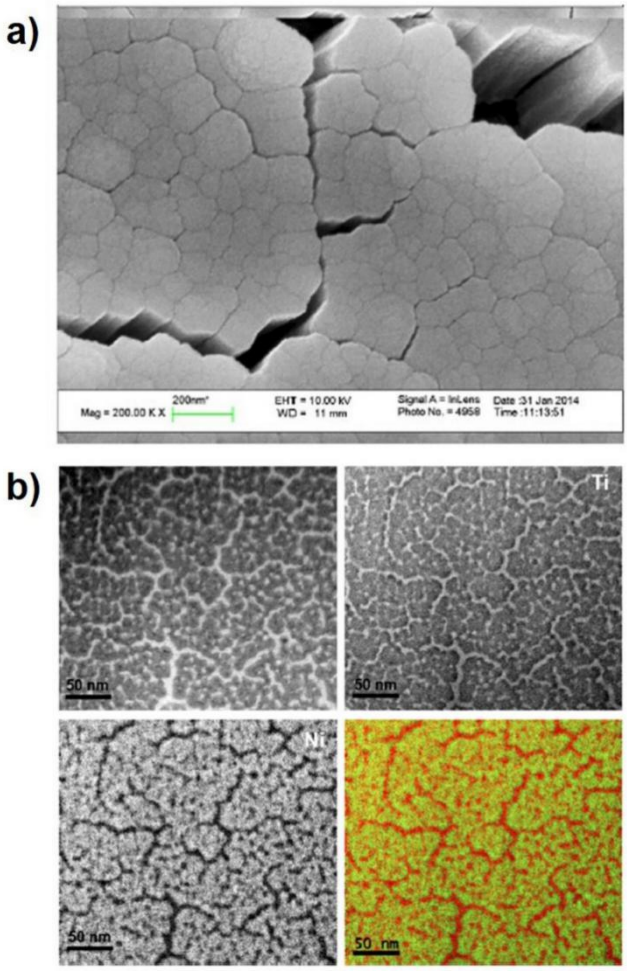

Figure 1-9. Scanning electron microscopy image of the surface morphology of the $Ni_{50}Ti_{45}Cu_5$ NG thick film (a). The non-filtered TEM image and corresponding elemental maps of Ti, Ni and their overlapped map (Ni in green and Ti in red) for the $Ni_{50}Ti_{45}Cu_5$ thin film (b). The concentration ratio between Ni and Ti in the columns is 5:3. [54]

Magnetron sputtering with powder targets has been employed to produce several different metal-based NGs [53-61]. These NGs show unique chemical [53], mechanical [53, 58], biological [59-61] properties. For instance, $Au_{52}Ag_5Pd_2Cu_{23}Si_{10}A_{l6}$ NG is a good catalyst for oxidation of organosilane compounds, also, this particular NG exhibits a high hardness, low elastic modulus, and good thermal stability [53].

Electrodeposition is an effective method to prepare high quality nanocrystalline materials [62], however its use is novel for NGs preparation. The surface morphology of the Ni-P sample that was prepared by Guo et al. using the multi-phase pulsed electrodeposition, is shown in Fig. 1-10 [63]. The granular structure of the surface indicates that the Ni-P amorphous alloy could be similar to consolidated NGs, which are composed of "nano-grains". Guo et al. also used SAXS to characterize the structure of this Ni-P sample, and found that its density is inhomogeneous on the nanometer-scale. The authors claimed that the Ni-P sample could be categorized in the NG family but the properties of this sample have not been studied.

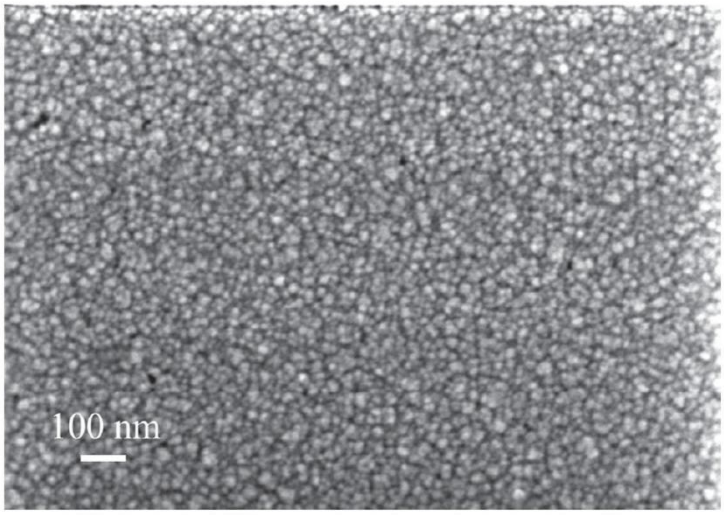

Figure 1-10. Scanning electron microscopy image of the surface morphology of the Ni-P thin film that was prepared by multi-phase pulsed electrodeposition. [63]

A cluster beam technology has recently been used by Kartouzian et al. to produce an amorphous Cu-Zr thin film [64]. The gas phase metallic clusters can be generated from an alloy target that is vaporized by a high frequency pulsed laser, and deposited on a borosilicate glass substrate. They claimed that these results are relevant to the NGs project, since also the NGs can be treated as cluster-built materials [65]. Determining if these thin films could be categorized as a NG would require further research, however, the initial research indicates that the crystallization temperature of the Cu-Zr thin film is much lower than the crystallization temperature of the normal Cu-Zr MG. This is inconsistent with Wang et al.'s result that the crystallization temperature of magnetron-sputtered $Au_{52}Ag_5Pd_2Cu_{25}Si_{10}Al_6$ NG thin film is higher than the corresponding MQR [66].

The above methodologies can be grouped into "bottom-up" methods in that the basic building blocks for the NGs are small non-crystalline nanoparticles or clusters. The "top-down" method is typically categorized as the introduction of multiple small shear bands into bulk MGs by severe plastic deformation (SPD), and the shear bands with enhanced free volume are assumed to be comparable to the interfaces in NGs [23, 67-70].

Typical SEM and TEM images of the cross-section of the severe plastic deformed $Au_{49}Ag_{5.5}Pd_{2.3}Cu_{26.9}Si_{16.3}$ bulk MGs are shown in Figs. 1-11a and 1-11b [23]. The presence of multiple small shear bands are indicated by a modulated microstructure with a spacing smaller than 100 nm between the shear bands. In addition, the DSC measurements indicate that the free volume of the as-prepared bulk MG sample (Fig. 1-11c) was enhanced by SPD (Fig. 1-11d).

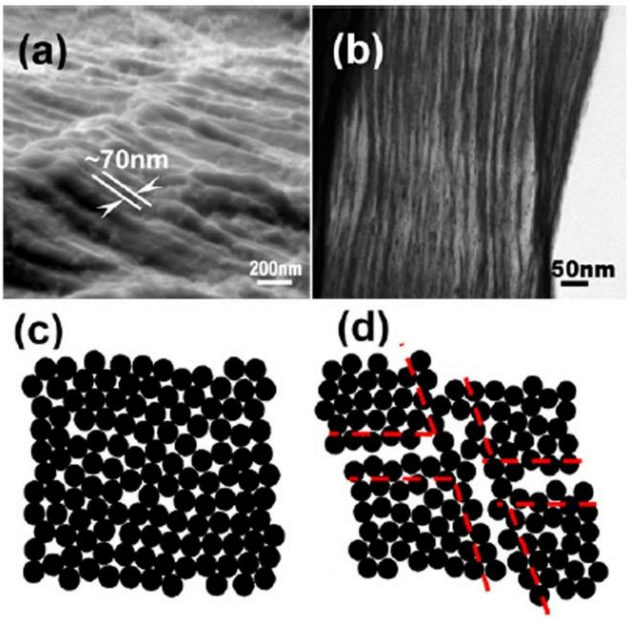

Figure 1-11. Scanning electron microscopy (a) and TEM (b) images of the cross-section of the $Au_{49}Ag_{5.5}Pd_{2.3}Cu_{26.9}Si_{16.3}$ bulk MG after SPD by high pressure torsion. Schematic drawing of the atomic structure of the as-prepared MG (c), and the atomic structure of the MG after SPD (d). The area within the red dashed cross represents the shear bands with enhanced free volume, the glass matrix is divided by shear bands into different nanometer-scale zones. Note, the density fluctuation of MG is referred to as NG. [23]

The formation of shear bands by SPD of MG can be accomplished in many glassy materials, however, achieving numerous small shear bands without crystallization of the MG is not easy, therefore this method can only be used in specific MG. Consequently, the consolidation of IGC making GNp into a bulk material could be the present ideal method for producing high quality bulk NGs. However, one big drawback of the IGC method is that the chemical compositions of the nanoparticles are dependent on the evaporation rate of the alloy components [41]. If the vapor pressures of the alloy components are not close to each other, the chemical compositions of the nanoparticles will vary during evaporation. The glass forming ability of MGs is closely related to the chemical composition, making it difficult to control not only the chemical compositions but also the amorphous state of the nanoparticles. In addition, the high price of the IGC apparatus paired with the small yield of the sample production limits the use of the IGC method.

Due to the limitation of IGC method, there have been few NGs synthesized by this route. Since the first NG was produced (Jing et al. in 1989) [25], only a few of NGs have been produced via IGC, such as Ni-Zr NG [71], Ti-Pd NG [72], Ni-Ti NG [71, 73, 74], Si-Au NG [75], Fe-Sc NG [6, 7], and Cu-Sc NG [76]. To find an adequate route to prepare large scale, high quality NGs, is urgently needed.

1.3.2 Electronic, atomic and microstructures of nanoglasses

In this section, research results of the NGs structures, including electronic, atomic, and microstructures will be briefly reviewed in chronological order.

The initial structural studies of NGs were conducted on the $Pd_{70}Fe_3Si_{27}$ NG using MS in 1989 [25]. As shown in the Fig. 1-12, the quadrupole splitting (QS) distribution of the MQR is displayed as a single peak (Fig. 1-12a), while the QS of the NG is displayed as two peaks (Fig. 1-12b). The QS distribution of the NG indicated that the NG consists of two components. One component is the interior region (cores), which likely has similar structure to the MQR, since the first QS distribution peak of the NG coincides with the QS distribution peak of the MQR. The second component is the interfacial region (interfaces) with larger QS (the red area under the second peak as indicated in the Fig. 1-12b). The larger QS values also indicated that the interfaces of $Pd_{70}Fe_3Si_{27}$ have a larger isomer shift. Since the larger isomer shift corresponds to the lower electron density, it means that the s-electron densities of the interfaces are reduced. The reduced s-electron density was explained as the reduced average atomic density.

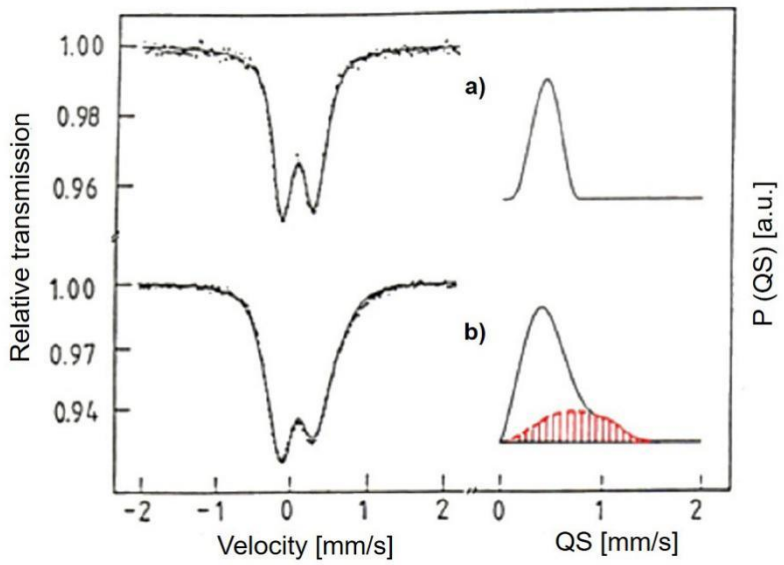

Figure 1-12. Mössbauer spectra and corresponding quadrupole splitting (QS) distribution (P(QS)) of the $Pd_{72}Fe_{10}Si_{18}$ MQR (a), and of $Pd_{70}Fe_3Si_{27}$ NG, which was produced by consolidating GNp into a bulk material (b). [25]

Weissmüller et al. investigated the atomic density distribution of Si rich Si-Au NGs through X-ray diffraction, and claimed that the Si-Au NGs had a lower SRO than the dense random packed and continuous random network structure amorphous alloys [75, 77].

Sturm and Wiedenmann used small angle neutron scattering to characterize the microstructure of $Si_{1-x}Au_x$ NGs [78-82]. They found that the small angle neutron scattering intensity decreases at a low q (scattering vector) according to a power law of $q^{-3.37}$ that was attributed to an internal surface fractal structure with a dimension of Ds= 2.63 (Fig. 1-13). The internal surface across the entire sample is an interconnected channel that formed between the highly dense regions and the agglomerates of the free volumes. Thus, NGs can be categorized as dense nanometer-sized particles embedded in a less dense "matrix" formed by free volume and "grain boundaries". In addition, they also found that the densities of $Si_{1-x}Au_x$ NGs are dependent on the average particle sizes, but are independent of the alloy chemical composition.

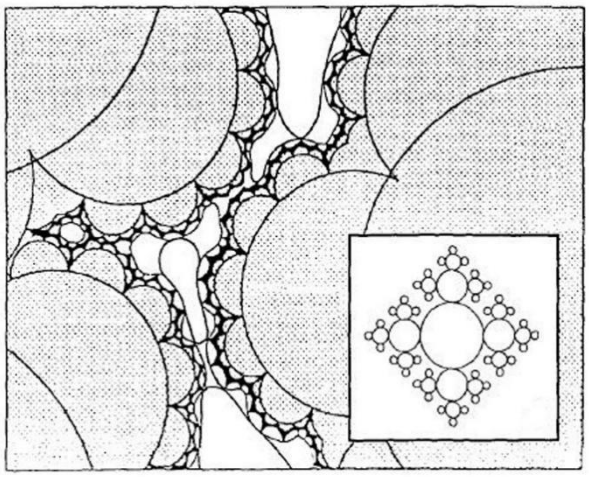

Figure 1-13. Schematic drawing of internal surface fractal structure of $Si_{1-x}Au_x$ NGs. [82]

The fractal structure of $Si_{1-x}Au_x$ NGs seem to be consistent with Campbell et al.'s computer simulation results of SiO_2 NG that was synthesized by consolidation of the SiO_2 GNp [83]. The structure of pores inside the SiO_2 NGs was self-similar with a fractal dimension close to 2 and the surface roughness exponents of pores were 0.5, when the densities ranged from 76% to 93% of the corresponding SiO_2 bulk glass. They also claimed that the SRO in SiO_2 NG was similar to the SRO in SiO_2 bulk glass (Both SiO_2 NG and bulk glass consist of corner-sharing $Si(O_{1/2})_4$ tetrahedra), however the MRO in these two glasses are quite different. The first sharp diffraction peak of the SiO_2 NG, which is the signature of MRO, is much lower and is shifted to the smaller wave vectors relative to the first sharp diffraction peak of the SiO_2 bulk glass.

Würschum et al. first studied the structural free volume of Ni-Zr NGs by using PAS [71]. They proposed that Ni-Zr NGs have more free volume than the corresponding ball-milled and melt-spun Ni-Zr amorphous alloys. Further studies were performed by Würschum in cooperation with Fang et al. to investigate the

distribution of free volume in the $Sc_{75}Fe_{25}$ NGs in detail by using PAS [6]. As shown in Fig. 1-14, the microstructure of $Sc_{75}Fe_{25}$ NG consists of nanometer-sized regions, as indicated by the thickness contrast (bright/dark regions).

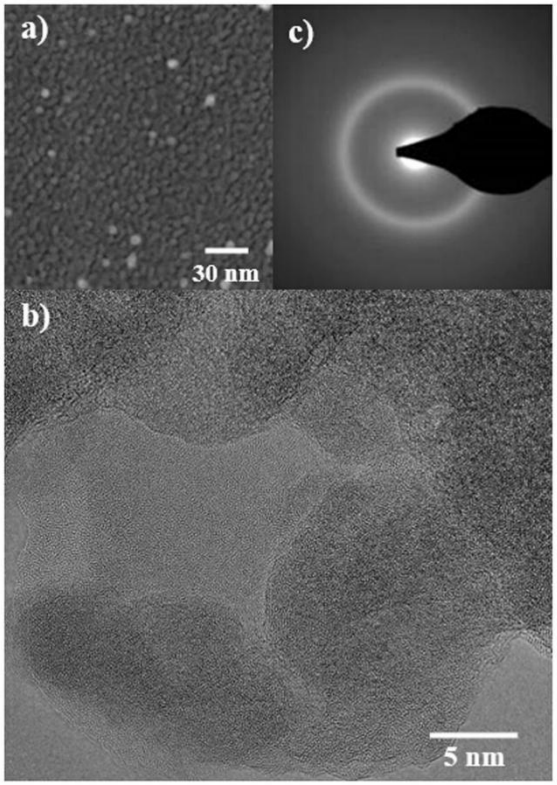

Figure 1-14. (a) TEM image of primary $Sc_{75}Fe_{25}$ GNp that were used to produce the NG by consolidation. (b) High resolution TEM (HRTEM) image of a $Sc_{75}Fe_{25}$ NG that was consolidated at 4.5 GPa. (c) ED pattern required from the selected area in (b). [6]

Two lifetimes components were observed in $Sc_{75}Fe_{25}$ NG after consolidation at 4.5 GPa, i.e., τ_1 =169 ps, and τ_2 =285 ps, with an average lifetime of 209 ps. Long positron lifetimes in the order of 350-500 ps, which are indicating nano-voids, have not been observed. Component τ_1 is considered originate from the cores of the NG and the second component τ_2 from the interfaces with their enhanced free volume. The volume fraction of the interfaces within the $Sc_{75}Fe_{25}$ NG was estimated to approximately 35%.

Small angle X-ray scattering was also applied to obtain additional information on the structure of the $Sc_{75}Fe_{25}$ NGs that were consolidated at different pressures (Fig. 1-15) [6]. In accordance with the PAS results, the SAXS curves were also composed of two components. The first was a power-law component that seemed to originate from the fractal fluctuations of electron density in the interior of the specimen and/or from the surface roughness, and a second superimposed hump indicated that the structure of the NG may be modeled as a two component system, i.e., regions with high and low electron densities. Density changes can originate from different chemical compositions and from enhanced free volume within interfacial regions. The SAXS data

were fitted assuming the NG consisted of spherical regions with the same density and a log normal size distribution, with an average sphere diameter of 5.4 nm for 1.5 GPa NG, and about 3 nm for 3.0 GPa and 4.5 GPa NGs. Since the diameter of the primary $Sc_{75}Fe_{25}$ GNp was about 7 nm (Fig. 1-14a), the humps in the SAXS curves may be correlated to the sizes of the cores and their interconnecting interfaces.

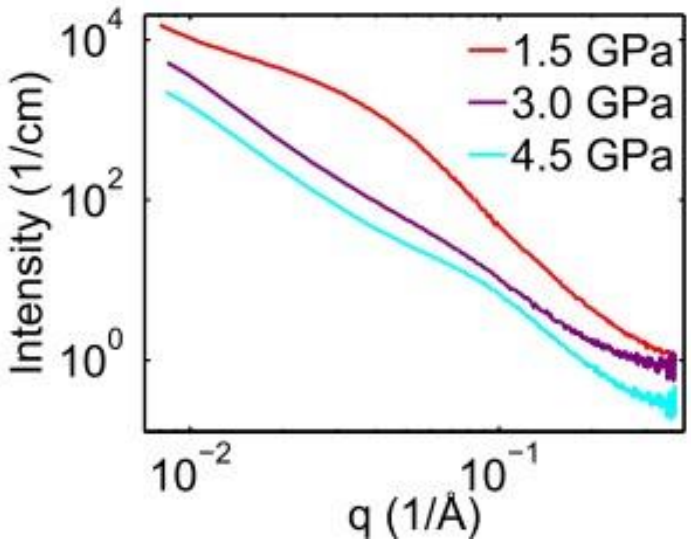

Figure 1-15. SAXS curves of $Sc_{75}Fe_{25}$ NGs consolidated at different pressures. [6]

Fang et al. also obtained the chemical composition profiles of $Sc_{75}Fe_{25}$ NG by using EDX mapping, and found that the interfaces were enriched with Sc. By analyzing the SAXS, the PAS, and the chemical composition profiles, Fang et al. calculated the electron density variations between the cores and the interfaces. They found that the interfaces have lower electron density than the cores. This is caused by the different chemical composition, as well as the lower atomic density. In summary, for $Sc_{75}Fe_{25}$ NG, the electron density and the atomic packing density of the interfaces are lower than the cores.

Witte et al. also used MS to investigate the structure of the $Fe_{90}Sc_{10}$ NGs [7]. The room temperature Mössbauer spectra indicated that the $Fe_{90}Sc_{10}$ NGs are ferromagnetic, while the corresponding MQRs are paramagnetic (Fig. 1-7). Low temperature Mössbauer spectra of the $Fe_{90}Sc_{10}$ NGs and the corresponding MQRs are presented in Fig. 1-16. The Mössbauer spectrum of $Fe_{90}Sc_{10}$ NGs consists of three sextets that were attributed to the cores, the interfaces, and bcc-Fe. Based on the fraction of each component in the spectrum of $Fe_{90}Sc_{10}$ NG, the volume fraction of the interfaces and cores were calculated to be 35% and 56%, respectively. The remaining fraction (9%) is assigned to bcc-Fe.

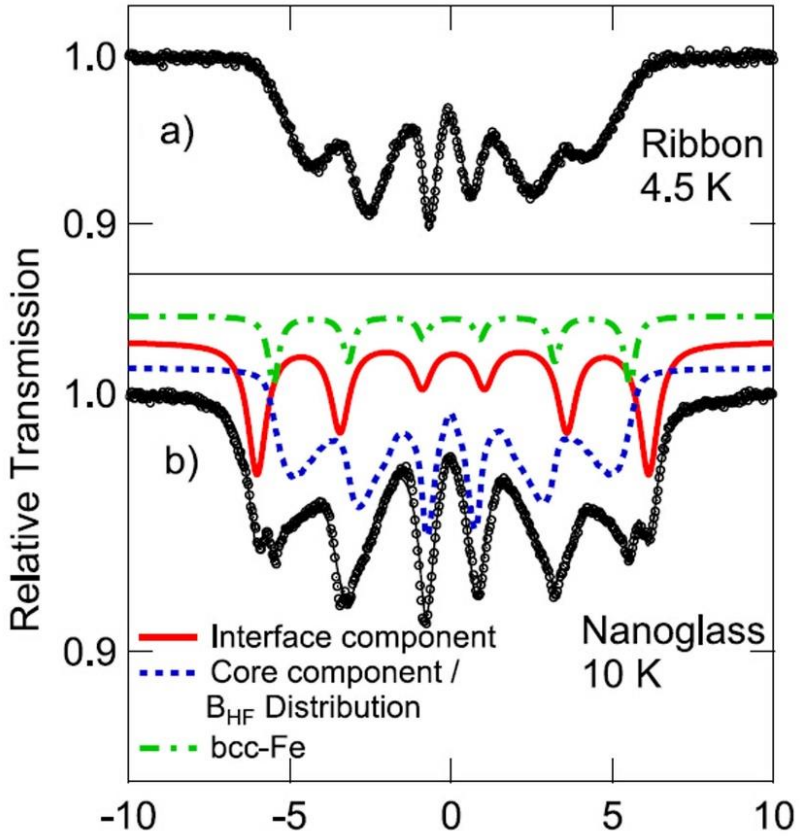

Figure 1-16. Low temperature Mössbauer spectra of $Fe_{90}Sc_{10}$ MQR (a) and NG (b). The Mössbauer spectrum of NG was fitted with three sextets. The dashed blue curve has the identical Mössbauer parameters as the ribbon spectrum (a), and is attributed to the cores. The solid red curve is attributed to the interfaces, and the dashed-dotted green curve is attributed to bcc-Fe. The spectral fractions of cores, interfaces, and bcc-Fe are approximately 35%, 56%, and 9%. [7]

Ghafari et al. further investigated the magnetic properties of $Fe_{90}Sc_{10}$ NGs and the corresponding MQRs using magnetic Compton scattering [84]. They found that the interfaces within $Fe_{90}Sc_{10}$ NGs exhibited more sp-electrons than crystalline Fe. The interfaces have higher magnetic moments than the cores and the corresponding MQRs, thus $Fe_{90}Sc_{10}$ NGs are ferromagnetic at room temperature.

Ghafari also studied the structure of $Fe_{90}Sc_{10}$ NGs by using high energy X-ray diffraction, and compared the radial distribution functions (RDFs) of the $Fe_{90}Sc_{10}$ NGs and the corresponding MQRs [8]. The coordination number (CN) was calculated in the range from 2.1 Å to 3.1 Å was 10.5 for NGs and was 11.3 for the MQRs (Fig. 1-17). It seems that the CN of the cores was the same as the CN of the MQRs. Combining that the interface fraction was calculated to be about 35% (Fig. 1-16b), the CN of the interfaces can be determined to be 9.1.

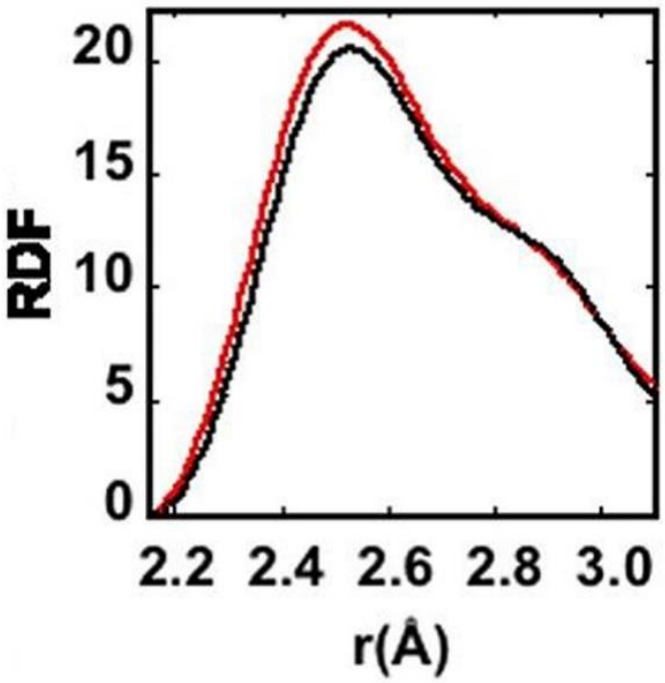

Figure 1-17. The RDF of $Fe_{90}Sc_{10}$ NG (red curve) and the RDF of the $Fe_{90}Sc_{10}$ MQR (black curve) with radial ranges of 2.1 Å–3.1 Å. [8]

X-ray absorption spectroscopy is a powerful technique that was applied by Léon et al. to study the structure of the $Fe_{90}Sc_{10}$ NGs [85].

The X-ray absorption near edge structure (XANES) spectra at the Sc K-edge of the different $Fe_{90}Sc_{10}$ NGs are shown in Fig. 1-18a. The different shapes of the XANES spectra imply that the local structures around the Sc atoms differ between the NGs and the MQRs. As a typical feature of 3d transition metals, the shoulders at the rising edge indicate that the SRO in the NGs is lower than the MQRs, and at lower consolidation pressures results in lower SRO. The comparison of the extended X-ray absorption fine structure (EXAFS) signal of the NGs and the MQRs is shown in Fig. 1-18b. The amplitude of the oscillation is lower than compared to the MQRs, and no obvious EXAFS oscillations of the NG samples were found beyond k = 7 Å, however, the oscillation of MQR was found up to k = 9 Å. This confirms the less ordered structure of NGs compared to the MQRs. The Fourier transformation of the k^2-weighted EXAFS function was calculated to separate the contributions of the different coordination shells (Fig. 1-18c). The amplitude of the first shell and the number of the high order shells (i.e., the second shell, and the third shell) were reduced in NGs when compared to the MQRs. The shells in the NGs were different from the shells in the MQRs, confirming the differences of the local structure between these two alloys.

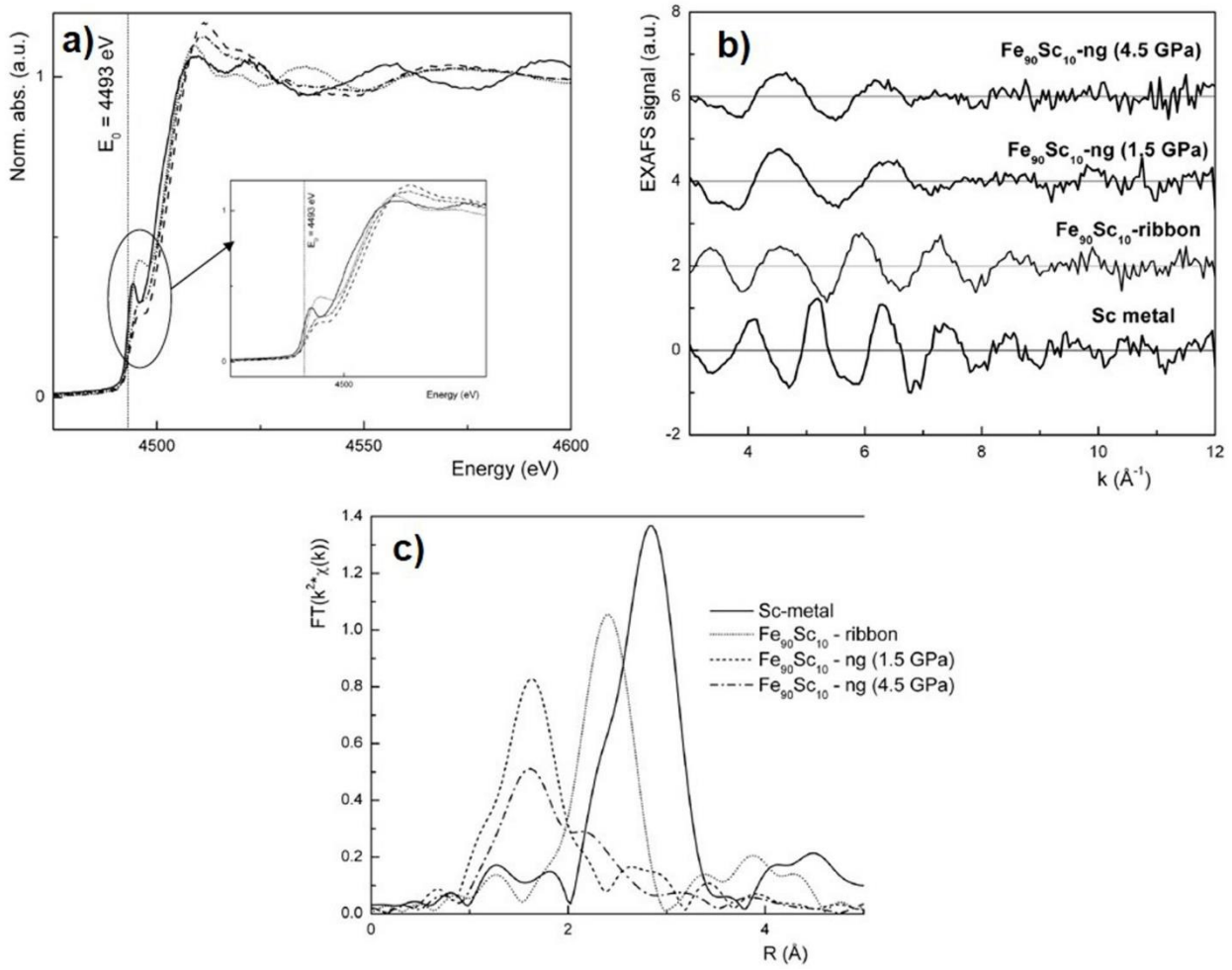

Figure 1-18. (a) XANES spectra at the Sc K-edge of the $Fe_{90}Sc_{10}$ NG consolidated at 1.4 GPa (dashed line); $Fe_{90}Sc_{10}$ NG consolidated at 4.5 GPa (dashed-dotted line), $Fe_{90}Sc_{10}$ MQR (dotted line) and pure Sc (solid line). (b) EXAFS signal at the Sc *K*-edge of the samples described in (a). (c) Amplitude of the Fourier transform of the EXAFS signal of (b). [85]

Molecular dynamics simulation of NG was initially performed by Albe et al. to investigate the microstructural evolution of the formation of a NG through sintering the Ge GNp [9]. Figures 1-19a – 1-19c display the arrangement of the atoms in a thin slice (1.5 nm thick) of materials cut out of the block of Ge NG. The primary uniform Ge GNp (5 nm in diameter) were arranged in a face centered cubic (fcc) pattern with voids between them (Fig. 1-19a). These Ge GNp were subsequently sintered at 300 K under a hydrostatic pressure of 5 GPa. With increasing time, the volume of the voids decreases, and interfacial areas (interfaces) between the adjacent GNp are formed (Figs. 1-19b and 1-19c). The corresponding evolution of the density distribution in NG is depicted in Figs. 1-19d – 1-19f, where the different colors show the variation of density. The density distribution (Fig. 1-19f) and the structural model (Fig. 1-19c) indicate that low-density interfaces containing enhanced free volume are formed. Figures 1-19c and 1-19f are the structural models of the Ge NG.

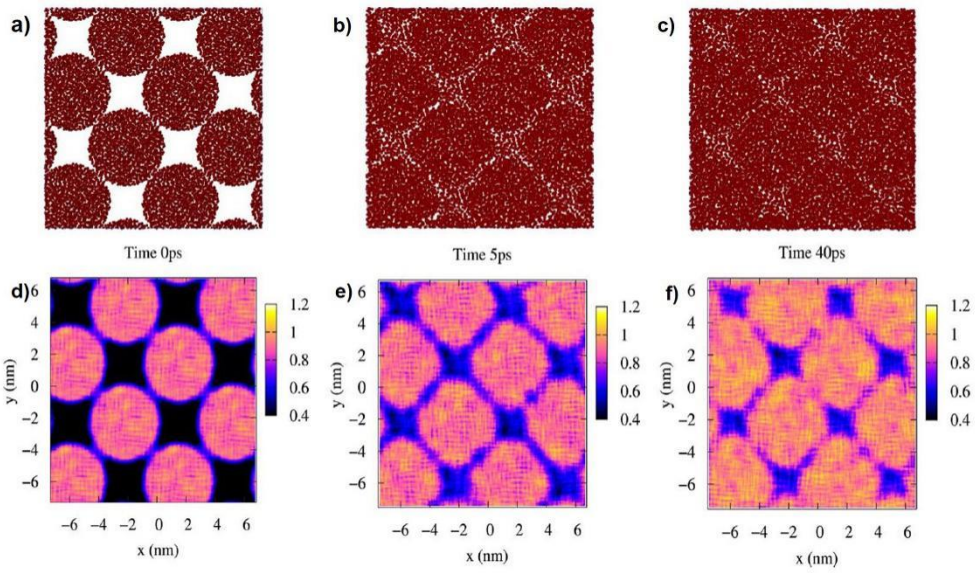

Figure 1-19. Computer simulation of the consolidation of a Ge NG that is obtained by sintering nanometer-sized (5 nm in diameter) Ge GNp at 300 K and 5 GPa. (a) - (c) are thin slices of materials cut from the bulk NG that display the atomic structure of the sintered NG by showing the position of the Ge atoms. (d) - (f) show the density distribution of the sintered NG corresponding to the structures as shown in (a)-(c). The contour plots indicate the atomic density relative to the bulk value. It can be seen that the NG consists of the dense cores connected by the loose interfacial regions. As the sintering process proceeds, the density of the interfacial regions increases. In the meantime, the low-density interfacial area increases, meaning the free volume between the corners of the GNp delocalize to form the wider interfaces. [9]

Albe et al. also simulated the internal interfaces of a $Cu_{64}Zr_{36}$ MG that were generated by joining two planar surfaces [10]. The fraction of Cu-centered full icosahedra found in the interfaces (the center of the interface is at x=0) of $Cu_{64}Zr_{36}$ glass was lower than the cores (Fig. 1-20a). The Voronoi volumes in an interfacial region of about 1 nm width were increased when compared to the average bulk Voronoi volume. This indicated that the free volume in the interfaces also increased.

To determine how the localized free volume in the interfaces correlates to the atomic structure, the frequency and spatial distribution of the Voronoi polyhedra were evaluated. Assuming the width of the interface being 1 nm, the differences in the atomic structures of the cores ("bulk"), the interfaces, and the shear bands can be found in Fig. 1-21. A Cu-centered full icosahedron [0, 0, 12, 0] is characterized as the densely atomic packed and the majority SRO in Cu-Zr glasses, its population in the cores was higher than in the interfaces. Additionally, the population of the Zr-centered polyhedra in the cores was also higher than in the interfaces and was characterized as dense atomic packed SRO. Thus, the interfaces within $Cu_{64}Zr_{36}$ glass were characterized by lower population of short-range order with excess free volume.

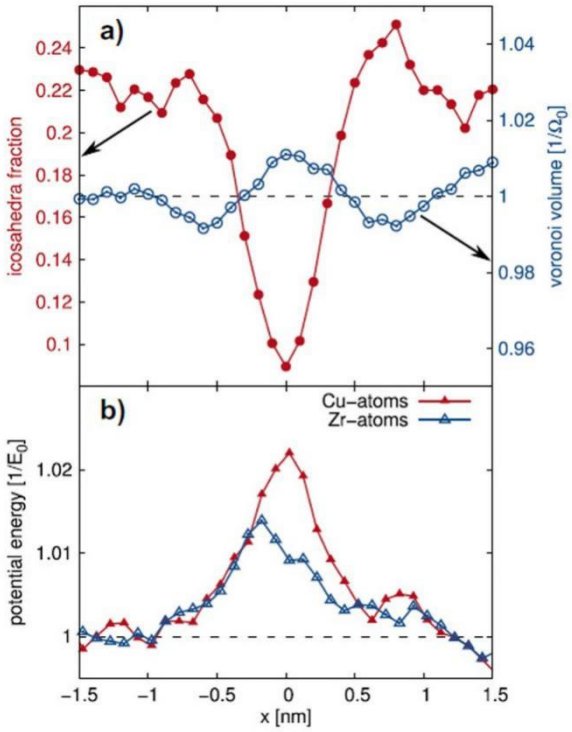

Figure 1-20. (a) Fraction of Cu-centered full icosahedra and Voronoi volumes and (b) potential energy as a function of the distance from the center of the interfaces within $Cu_{64}Zr_{36}$ MG where x = 0 nm. [10]

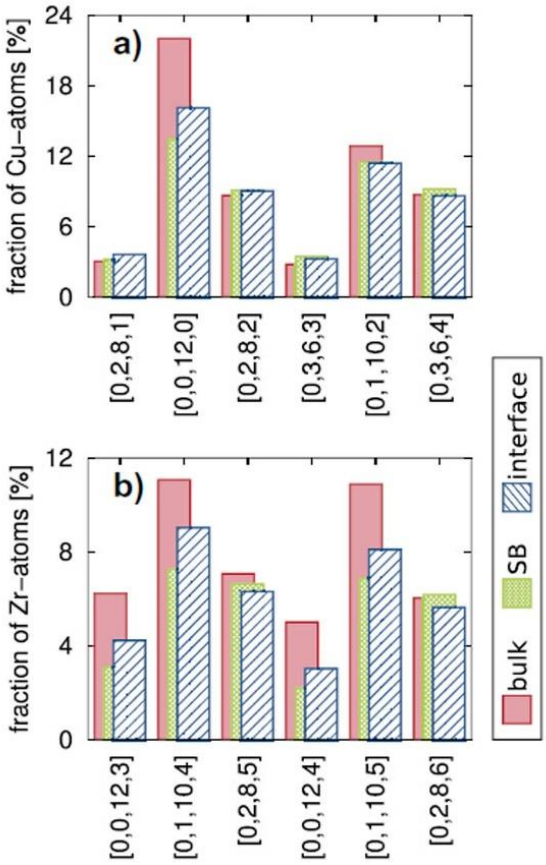

Figure 1-21. Fraction of (a) Cu-centered and (b) Zr-centered Voronoi polyhedra with a population >3% in the $Cu_{64}Zr_{36}$ glasses. The Cu-centered full icosahedron is the dominant Voronoi polyhedon in the cores (bulk), and its population in the cores is higher than the interfaces. For the Zr-centered Voronoi polyhedra, the population in the cores is also higher than the interfaces, which indicates that the interfaces are deficient of SRO. The SRO of the interface shows similar features to a shear band ("SB") in the same alloy. [10]

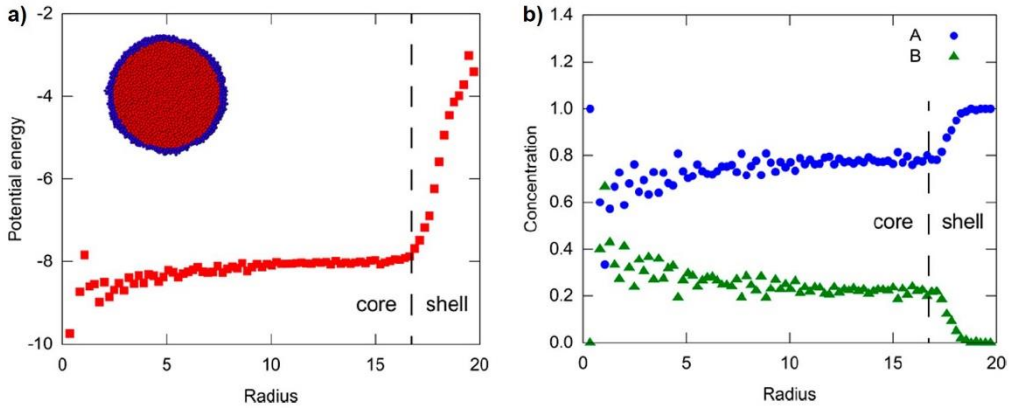

Figure 1-22. Potential energy (a) and chemical composition (b) as a function of radius in a glassy nanoparticle that is prepared by vapor deposition. Inset in (a) shows a cross-section of the nanoparticle, where red spheres represent cores and blue spheres represent the shell. (b) Indicates that the shell of the glassy nanoparticle is enriched with the majority component (A atoms). [11]

Danilov et al. modeled the physical vapor deposition process of the binary GNp and their consolidation into a NG [11]. They found that the potential energy of the GNp is higher in the surface shells than in the cores (Fig. 1-22a), and the majority component (A atoms) segregation occurs within the primary GNp (Fig. 1-22b). This is consistent with the surface segregation behavior of $Sc_{75}Fe_{25}$ GNp.

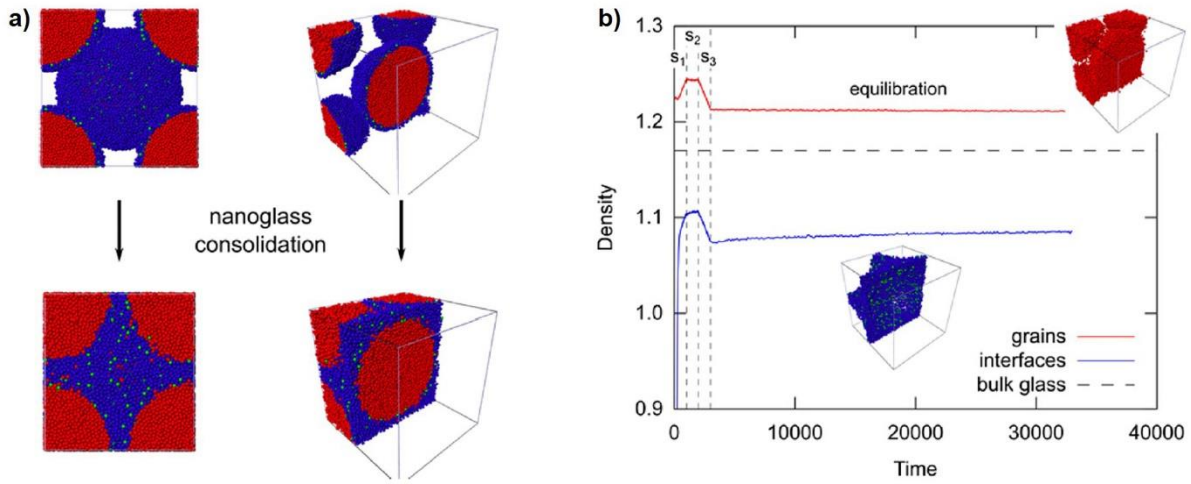

Figure 1-23. Consolidation of segregated GNp into a NG (a) and densities evolution of the cores (grains) and shells (interfaces) during consolidation and the subsequent equilibration process (b). The red spheres represent both A and B atoms in the cores, while the blue spheres solely represent the A atoms within the shells, and green spheres solely represent the B atoms within the shells. (a) Indicates the interfaces of NG are enriched with the majority component that is transferred from the primary GNp. (b) Indicates the density of interfaces of NG is lower than the corresponding bulk glass and the cores. [11]

The consolidated NG consists of two components, i.e., the nanometer-sized cores and the interfaces between them (Fig. 1-23a). Compared to the cores, the interfaces are enriched with majority component (Fig. 1-23a). This effect can be understood by assuming that the composition gradient in the GNp (Fig. 1-22) are transferred to the consolidated materials (Fig. 1-23a). However, the atomic packing density of the interfaces is lower (Fig. 1-23b) because the delocalization of the free volume between the corners of the GNp. Interestingly, the density of the cores was higher than the corresponding bulk glass (Fig. 1-23b). Until now, the experimental data for the density of the cores was not sufficient.

Adjaoud and Albe obtained similar structural information of the GNp and the corresponding NG via molecular simulation [12]. They found that the segregation of the majority component occurs in the $Pd_{80}Si_{20}$ and $Cu_{64}Zr_{36}$ MGs as well. They highlighted that Pd segregates to the shells of the $Pd_{80}Si_{20}$ GNp, and Cu segregates to the shells of the $Cu_{64}Zr_{36}$ GNp. They claimed that the surface segregation effect in GNp depends on the potential energy of the components. However, other research stated that the surface segregation of the alloys is dependent on the balance between the surface energy and the total potential energy of the alloys [86-89]. Without studying the surface segregation behavior of the Si-rich Pd-Si GNp and the Zr-rich Cu-Zr GNp, one

cannot conclude that the surface segregation behavior of GNp is controlled solely by potential energy of the components. To clarify the surface segregation behavior of GNp, further experimental studies are necessary.

The simulations indicate that the surface segregation effect plays an important role in determining the chemical composition of the surfaces of GNp. The chemical composition of the interfaces is different from the interior cores since the chemical composition of the surfaces can also be transferred into the interfaces within NGs.

Adjaoud [12] suggested that the atomic size of the segregated component in the surfaces of the primary GNp would affect the number density and the electron density of the consolidated interfaces within NGs. The number and the electron densities of the segregated interfaces within $Pd_{80}Si_{20}$ NGs are lower than the cores, while the number and electron densities of the interfaces within $Cu_{64}Zr_{36}$ NGs are higher than the cores (see Fig. 1-24). This is due to the smaller size Cu atoms enriching the interfaces. The interfaces of $Fe_{90}Sc_{10}$ NGs should be enriched with smaller size Fe atoms, assuming the majority component (Fe atoms) segregation behavior also occurs in the case of $Fe_{90}Sc_{10}$ GNp. According to Adjaoud's results, the number and the electron densities of the segregated interfaces within $Fe_{90}Sc_{10}$ NGs should be higher than the cores. This finding conflicts with the experimental results described above, where the number and the electron densities of the interfaces within $Fe_{90}Sc_{10}$ NG are lower than the cores. Therefore, the surface segregation behavior and the atomic packing behavior of $Fe_{90}Sc_{10}$ GNp requires further clarification into the discrepancy between the experimental and the simulation results.

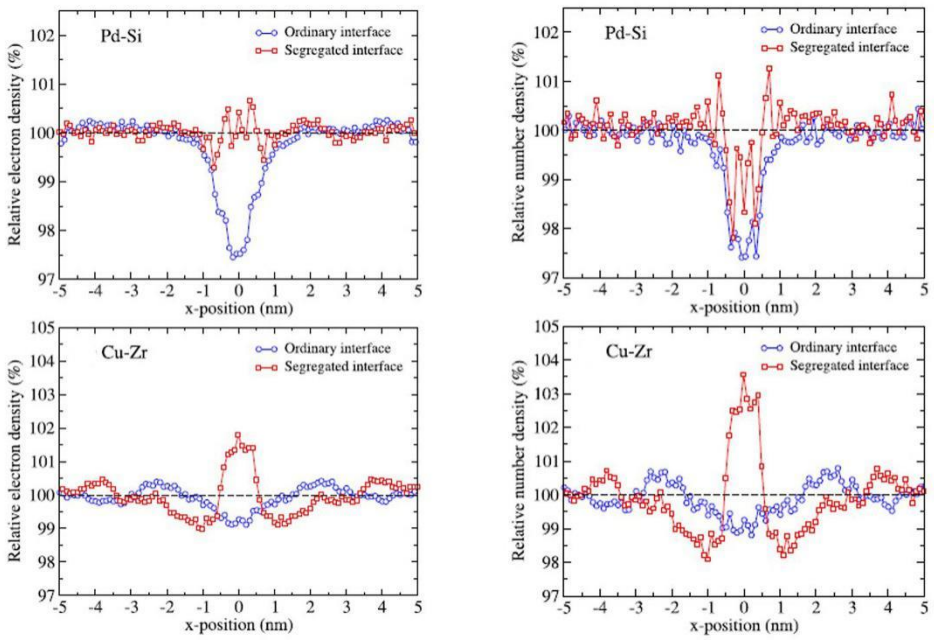

Figure 1-24. Variations of relative electron and number densities of Pd-Si and Cu-Zr glasses with ordinary (composition homogeneous) and segregated (composition inhomogeneous) interfaces. The center of the interface is x=0. The relative densities are given relative to the total bulk value, which is taken as 100%. [12]

Both the experimental and the simulation results confirmed that NGs have novel electronic, atomic, and microstructures, that differ from the corresponding traditional MGs with similar average chemical composition. Interfaces within NGs have lower electron density, different chemical composition, lower CN, different SRO, and enhanced free volume when compared to the cores and the corresponding MQRs. However, since achieving the real-space structural characterization of the SRO of MGs is difficult, details pertaining to the atomic packing behavior of NGs, such as the types of SRO within NGs, remain unclear. Additional experimental studies are necessary to gain further understanding of the structure of NGs.

1.3.3 Structural stability of nanoglasses

Although the structural stability of NGs is important, there is a lack of research due to the general difficulties in performing structural characterization. The study performed by Fang et al. is the only known comprehensive experimental study of the structural stability of NGs (here the NGs are only referred to as the consolidated NGs, it is important to note that there is another report regarding the structural stability of the Au-based NG thin films [90]) [6]. In fact, studies that address the structural stability of NGs typically were normally conducted by computer simulations. In this section, the experimental results of the current study and the latest simulation results will be briefly reviewed.

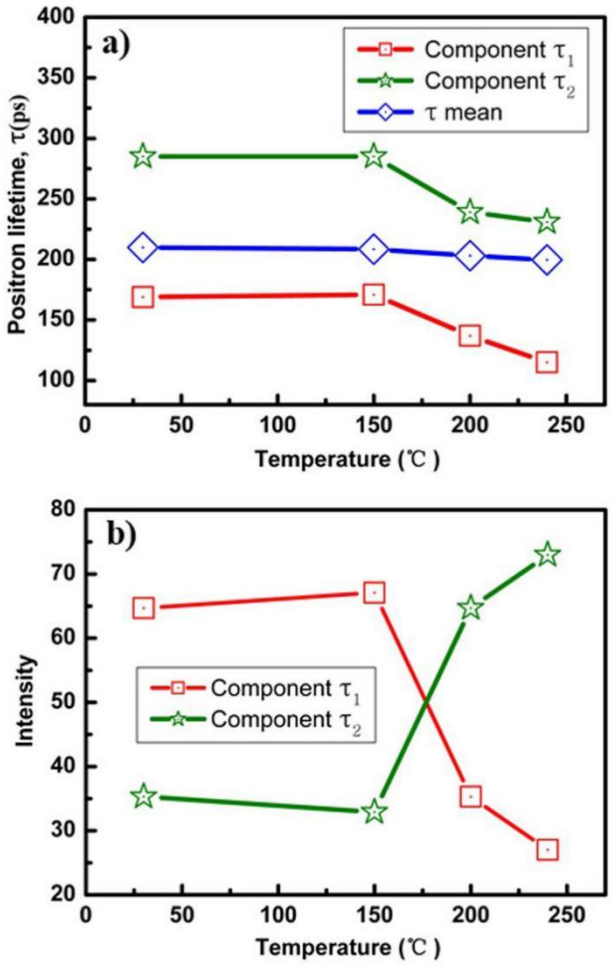

Figure 1-25. Positron lifetimes and relative intensities of the as-prepared $Sc_{75}Fe_{25}$ NG and of the same NG during annealing. (a) Positron lifetime of components τ_1 (red line), τ_2 (green line), and mean positron lifetime τ_m (blue line). (b) Relative intensities I_1 (τ_1 component), I_2 (τ_2 component), $I_1 = 100 - I_2$. [6]

Fang et al. studied the structural evolution of $Sc_{75}Fe_{25}$ NG during annealing [6]. In this study, PAS was employed to examine the evolution of the free volume in $Sc_{75}Fe_{25}$ NG (consolidated at 4.5 GPa) as a function of temperature, see in Fig. 1-25 for results. The as-prepared $Sc_{75}Fe_{25}$ NG, τ_1 component (τ_1 = 169 ps) is considered to originate from the cores of the NG. It was suggested that the τ_2 component (τ_2 = 285 ps) originates from the interfaces (Fig. 1-25a). The volume fraction of the interfaces within the as-prepared $Sc_{75}Fe_{25}$ NG was about 35% (Fig. 1-25b). After annealing at 150 °C, the intensity of the τ_2 component increased from 35% to 75%, implying that the volume fraction of the interfaces also increased from 35% to 75%. After annealing at temperatures above 150 °C (Fig. 1-25a), the lifetimes of τ_1 and τ_2 decreased to lifetimes similar to pure α-Fe and pure Sc. This is consistent with the elemental mapping in the NG, where the interfaces were enriched with nearly pure Sc. The average free volume within the NG decreased, as indicated by the decrease of the mean positron lifetime τ_m (Fig. 1-25a). The decrease of τ_m further indicated the annihilation of free volume within NG, due to structural relaxation.

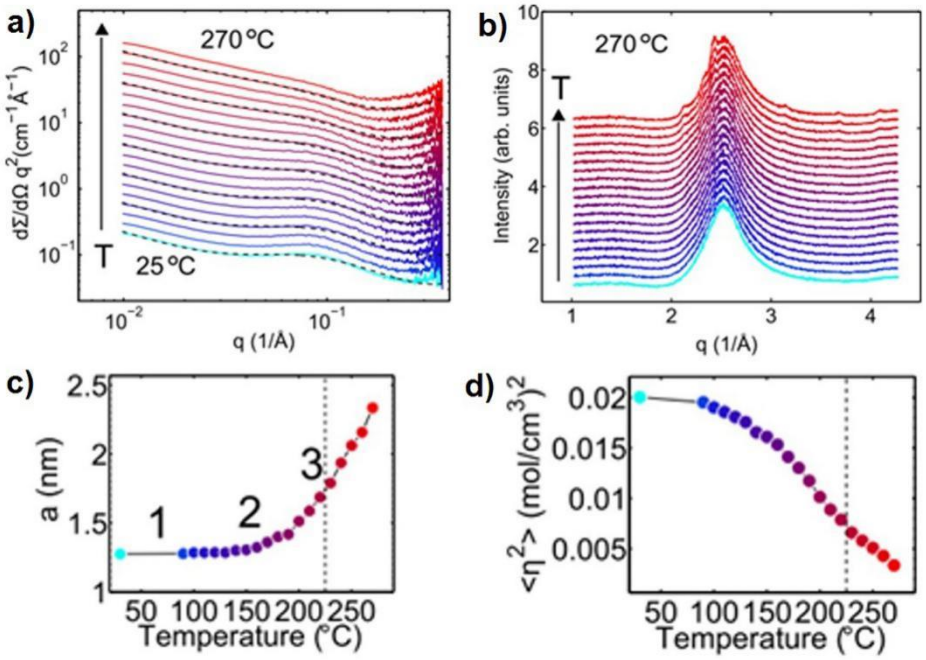

Figure 1-26. q^2-weighted SAXS curves (a) and WAXS (b) of a $Sc_{75}Fe_{25}$ NG (consolidated at 4.5 GPa) as a function of the annealing temperature. The positions of the curves have been shifted vertically for clarity, with the exception of the lowest curve. (c) and (d) are the results of the Debye-Bueche model fitting of the SAXS curves in (a). q is the length of the scattering vector and $q=4\pi\sin\theta/\lambda$, where λ is the wavelength of the X-ray and θ is half of the scattering angle. [6]

To substantiate the PAS results, in-situ SAXS was applied to examine the structural evolution of the $Sc_{75}Fe_{25}$ NG (consolidated at 4.5 GPa) as a function of the temperature. The original SXAS data curves consisted of two components similar to the curves in Fig. 1-15, i.e., a power-law component and a superimposed hump (see Fig. 1-26a). The Debye−Bueche model was used to fit the curves, where the two parameters, **a** and $\langle\eta^2\rangle$, can be obtained. **a** is the correlation length that represents the thickness of the interfaces. $\langle\eta^2\rangle$ is the mean

square fluctuation of the electron density, and it is dependent on the electron density difference between the high- and the low-density regions. In other words, $\langle \eta^2 \rangle$ characterizes the electron density difference between the cores and the interfaces. Therefore, the thickness of the interfaces increases as the temperature increases as indicated in Fig. 1-26c. This is consistent with the PAS data that showed the volume fraction of the interfaces increased with the temperature increase (Fig. 1-25b). The $\langle \eta^2 \rangle$ decreases as the temperature increases, indicating that the electron density difference between the cores and the interfaces decreases. The electron density difference between the cores and interfaces is primarily attributed to the free volume content difference between them but not the composition difference. This suggests that the decrease of the electron density difference results from the decrease of the free volume content difference (between the cores and the interfaces), i.e., the atomic density difference decreases.

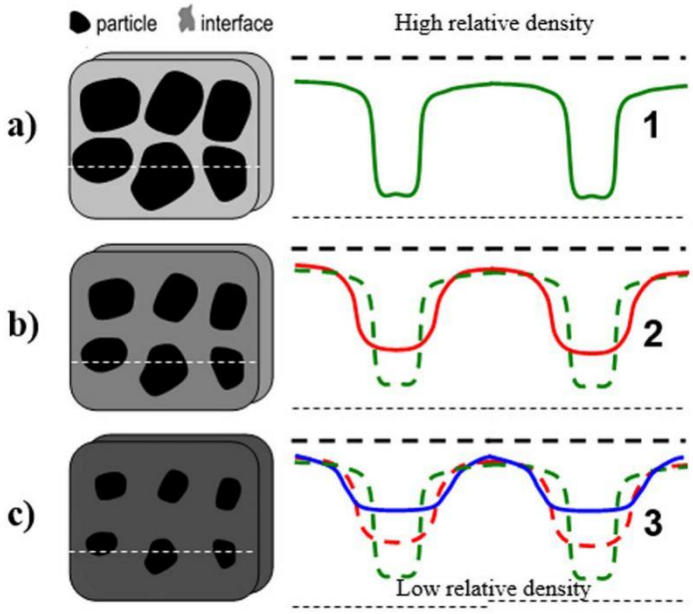

Figure 1-27. Schematic drawing of the structural evolution of the $Sc_{75}Fe_{25}$ NG during annealing that was summarized according to the results of the SAXS/WAXS and the PAS. The different dark/light grey colors represent the different density regions in the NG. For every NG structural model, the darker region represents the cores with high density, and the lighter region represents the interfacial region. The white dashed lines in (a), (b), and (c) represents the cross section of the NGs. 1−3 are the relative densities corresponding to steps 1−3 in Fig. 1-26c. [6]

Consequently, Fang et al. summarized the structural evolution of the NG according to the variation of **a** and $\langle \eta^2 \rangle$. This, in combination of the PAS results, let them to propose a schematic drawing of the structural evolution, as shown in Fig. 1-27. The different dark/light grey colors represent the regions with different densities. Within this NG structural model, the darker region represents the cores with high density, while the relative lighter region represents the interfacial region between the two cores. The curves in the right side of the Fig. 1-27 represent the relative electron density fluctuation of the NG and its evolution during annealing. The interfaces are small for the as-prepared NG (Fig. 1-27a). After annealing, the volume fraction of the interfaces

increases, while the volume fraction of the high-density cores decreases (left side of Figs. 1-27b and 1-27c). Accordingly, the electron density difference between the cores and the interfaces decreases (right side of the Figs. 1-27b and 1-27c). This suggests that the free volume within the interfaces delocalizes as time and temperature increases. However, the WAXS curves indicate that the onset of the crystallization prior to the free volume spreads out over the entire specimen.

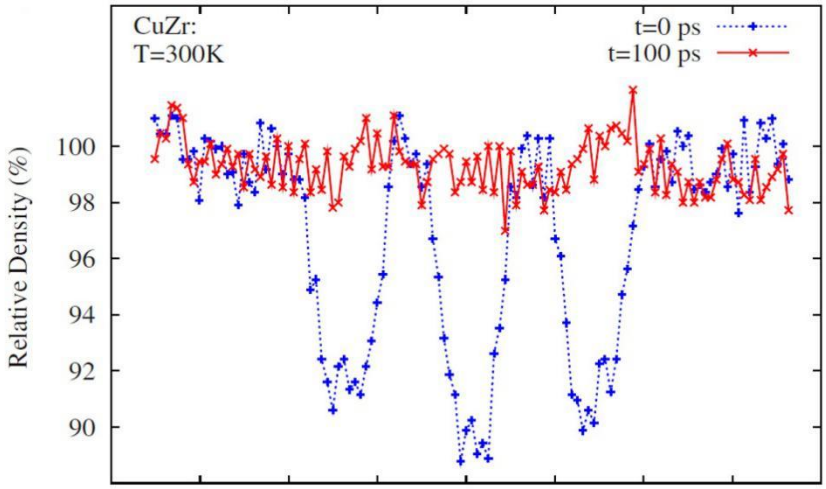

Figure 1-28. Computer simulation of the density variation of the interfaces within Cu-Zr NG under annealing at 300 K for 100 ps. The dotted red line represents the initial density distribution, the solid blue line represents the density distribution after annealing. [9]

Based on Albe et al.'s previous simulation results, it was concluded that the free volume within the interfaces spreads out over the entire sample during annealing [9]. As shown in Fig. 1-28, the initial density in the center of the interfaces within Cu-Zr NG was about 90%, with a bulk glass density of 100%. When Cu-Zr NG was annealed at 300 K for 100 ps, the enhanced free volume in the interfaces spreads out, resulting in a nearly homogenous density structure. These results were different than the experimental results that found the interfaces within the $Sc_{75}Fe_{25}$ NG were stable during annealing [6]. The different chemical compositions between the interfaces and the cores has never been considered in the simulation of the structural evolution for the Cu-Zr NG during annealing. This is a possible explanation for the discrepancy between the experimental results and the simulation results. The chemical composition of the interfaces in $Sc_{75}Fe_{25}$ NG is different from the cores, meaning that the interfaces have a different electronic structure from the cores. In fact, the different electronic structure between the interfaces and the cores have been reported in $Fe_{90}Sc_{10}$ NGs [84]. In addition, the segregated interfaces exhibiting different chemical compositions may contain different types of SRO than the cores and the ordinary interfaces (Figs. 1-20 and 1-21) [10, 37]. Accordingly, the different electronic and atomic structures of the segregated interfaces may result in the enhanced structural stability. Moreover, the cores of $Sc_{75}Fe_{25}$ NG contain more Fe, due to the solute drag effect [91,92], the Fe within the cores possibly slowing the diffusion of the atoms.

Danilov et al. took the surface segregation of the primary GNp into account for their simulation work, discovering that the corresponding NGs are stable [11]. As described in last section, Danilov modeled the physical vapor deposition process of the binary GNp and their consolidation into a NG. The average chemical composition of the physical vapor deposited (PVD) GNp is $A_{80}B_{20,}$ however, the chemical composition within the cores of the GNp is $A_{77}B_{23}$ due to the surface segregation of the A atoms. The potential energy of the $A_{77}B_{23}$ bulk glass is lower than the $A_{80}B_{20}$ bulk glass (Fig. 1-29a), suggesting that the potential energy of the cores was reduced due to the surface segregation. In fact, the potential energy per atom of the segregated GNp is lower than the corresponding bulk glass with identical average chemical composition (Fig. 1-29a), although the potential energy of the shells of the GNp is high (Fig. 1-22a). Accordingly, the enthalpy of the NG that was prepared by consolidation of the segregated GNp, remains lower than the enthalpy of the bulk glass, despite the interfaces within NG being enriched with extra free volume (Fig. 1-23).

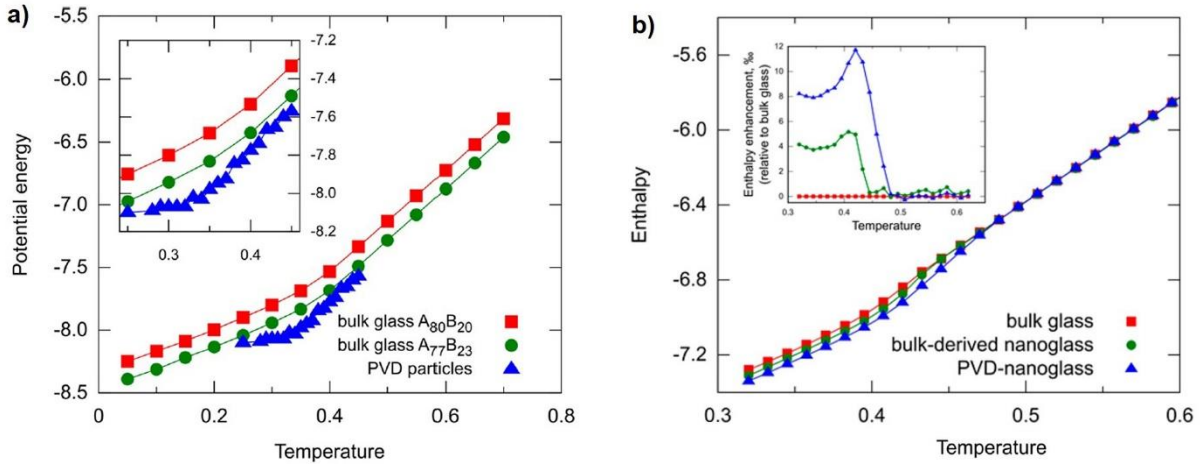

Figure 1-29. (a) The potential energy per atom of the PVD GNp (blue) as a function of the deposition temperature，and the potential energy per atom of the $A_{80}B_{20}$ bulk glass (red) and the $A_{77}B_{23}$ bulk glass (green) as a function of the cooling temperature. (b) Enthalpy of the bulk glass that were cooled form the melt (red), bulk derived NG (green), and the PVD NG (blue).The inset in (b) shows the enthalpy enhancement of the bulk-derived NG and the PVD NG relative to the bulk glass. [11]

According to Adjaoud and Albe [12], the interfacial energy of the segregated interfaces that were formed by consolidation of the segregated GNp is lower than the interfacial energy of ordinary interfaces. The calculated interfacial energies of the segregated interfaces in Cu-Zr and Pd-Si glasses were 0.135 J/m^2 and 0.436 J/m^2, while the interfacial energies of the ordinary interfaces in Cu-Zr and Pd-Si glasses were calculated to be 0.414 J/m^2 and 0.938 J/m^2.

From the results obtained by Danilov [11] and Adjaoud [12], it can be concluded that the interfacial energy of the segregated interfaces within NGs and the potential energy of the entire NG are both reduced due to the surface segregation of the primary GNp, resulting in the enhancement of structural stability of the NGs.

Studies have shown that there are additional nanostructured amorphous materials with high stability. The mechanism of stability within these amorphous materials may provide an explanation of the structural stability

of the NGs. Guo et al. [93] prepared nanostructured glassy polymer thin films, where they discovered that this polymer thin film enhanced the thermal stability at higher glass transition temperature (40 K higher) than the ordinary polymer thin film, but the density of this thin film was 40% lower than the ordinary polymer thin film. They suggested that the ultra-stable nature of the nanostructured polymer thin film stemmed from the nanostructure and the interfaces between the thin film and the deposited glass. Wang et al. [66] studied the thermal stability of the magnetron sputtered Au-based NG, which had an enhanced thermal stability with a higher glass transition temperature (20 K higher) and higher crystallization peak temperature (32 K higher) than the corresponding MQR. They attributed the ultra-stable behavior of this NG thin film to the nanostructure and the relaxation during deposition. However, it is unclear why nanostructures can enhance the stability of these amorphous materials.

The structural stability of NGs is not well understood, particularly by experimental studies. The mechanisms contributing to the structural stability of NGs are not understood. Therefore, experimental studies have been performed in this thesis project to improve our understanding of the structural stability of NGs.

2 Techniques and Experiments

2.1 Background of techniques

2.1.1 Inert gas condensation

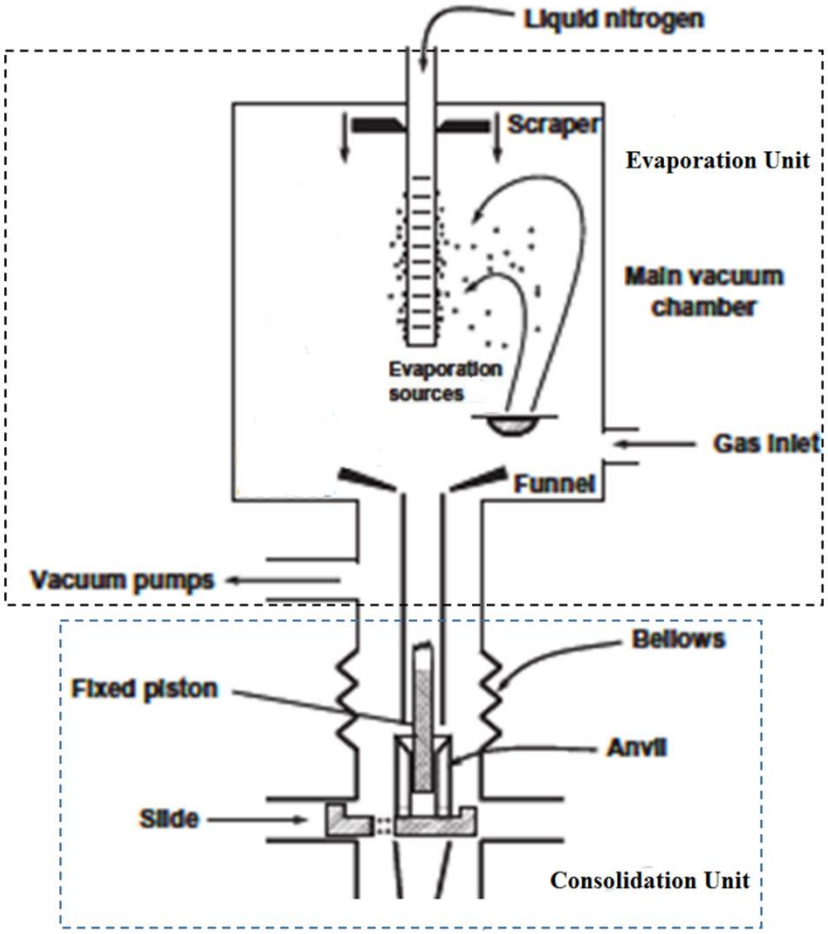

Figure 2-1. Schematic of the IGC chamber for the synthesis of nanostructured crystalline or non-crystalline materials. [41]

The IGC [41] system is mainly comprised of two units, namely the evaporation unit and the consolidation unit (Fig. 2-1). The evaporation unit consists of an UHV chamber, which can reach a pressure of 4×10^{-8} mbar using a turbo-pump.

At the onset of the sample preparation, pumping is stopped and the inert gas (He or Ar) is backfilled into the chamber at a low pressure ranging from 1 to 20 mbar. Then the crucible (W, Ta, or Mo) containing the metal or alloy is heated up to the evaporating temperature of the alloy. In the meantime, the cold finger is cooled down with liquid nitrogen.

At the beginning of the condensation process, the metal vapors evaporate from the thermally heated boat and collide with the inert gas to lose their kinetic energy. These metal atoms are termed as "monomer". The monomers nucleate into small clusters, and subsequently grow by colliding with monomers or by coalescing with other clusters, which is termed as "monomeric growth". Thus, three separate events, namely nucleation, monomeric growth and coagulation occur simultaneously [94]. The average clusters size could be altered by the type and pressure of the inert-gas, temperature of the metals, etc. [41, 95, 96] Convection currents, generated from the heating of the inert gas by the evaporation source and cooling by the liquid nitrogen-filled collection device (cold finger), can carry the condensed fine nanoparticles from the crucible region to the collection device.

The deposited particles are scraped from the cold finger and fall into the anvil. After sufficient amount of particles has been collected, the heating of the boat is stopped and the vacuum pump is applied to achieve UHV conditions in the chamber again in order to minimize the amount of trapped gases. Subsequently, the nanoparticles are consolidated into a disk-shaped pellet with 8 mm in diameter and a thickness of 0.1-0.5 mm.

2.1.2 X-ray diffraction

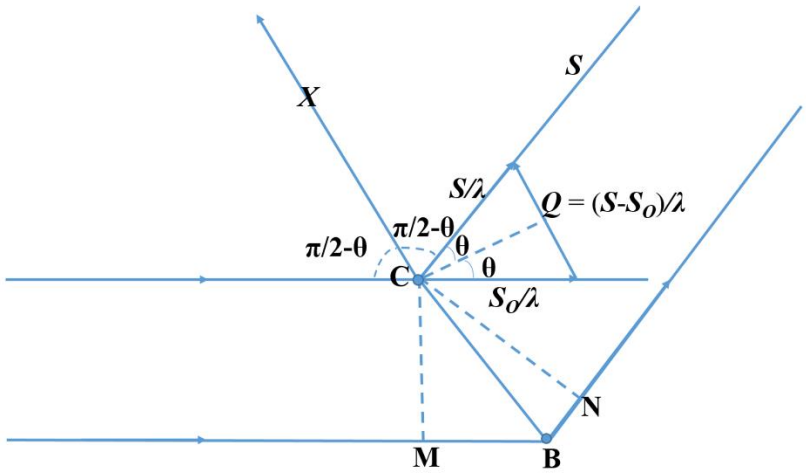

Figure 2-2. Interference between the waves scattered by two individual atoms. [97]

X-rays are a form of electromagnetic radiation with a wavelength normally ranging from 0.1 Å to 100 Å. X-ray diffraction [97, 98] by matter combines of two basic kinds of phenomena, one is the waves scattered by the individual atoms and the other is the interference between these waves.

As shown in Fig. 2-2, the direction of the incident waves is $\boldsymbol{S_O}$, and the direction of the waves scattered by the two atoms C and B is $\boldsymbol{S}$. The path length for the rays going through B is larger than A by L= MB+BN, where M and N are the projections of A. Since MB= $\boldsymbol{S_O}\times\boldsymbol{CM}$, BN=$-\boldsymbol{S}\times\boldsymbol{CM}$, then L=$-\boldsymbol{CM}\times(\boldsymbol{S}-\boldsymbol{S_O})$. Therefore, the scattering phase shift between atoms C and B is $\Psi=2\pi L/\lambda=-2\pi\boldsymbol{CM}\times(\boldsymbol{S}-\boldsymbol{S_0})/\lambda$, where λ is the wavelength of the rays. And Ψ depends on the respective positions of the scattering centers, i.e., the positions of atoms C and B.

Define the vector $\boldsymbol{Q}=(\boldsymbol{S}-\boldsymbol{S_O})/\lambda$, then the direction of $\boldsymbol{Q}$ is $\boldsymbol{CX}$ which bisects the angle formed between vectors $\boldsymbol{S}$ and $-\boldsymbol{S_O}$. If 2θ is the angle between $\boldsymbol{S}$ and $\boldsymbol{S_O}$, then the length of $\boldsymbol{Q}$ is:

$$|Q| = \frac{2\sin\theta}{\lambda} . \quad (2\text{-}1)$$

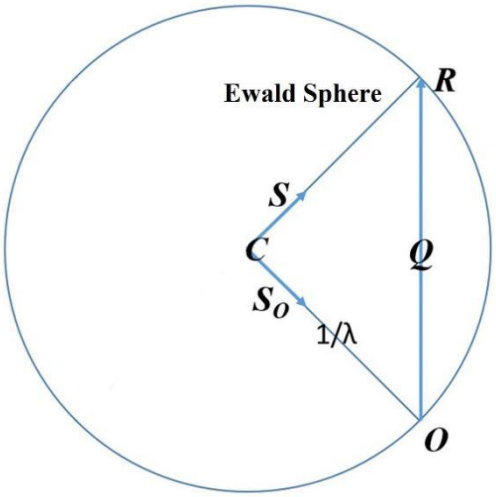

Figure 2-3. The reciprocal space explored by the Ewald sphere.

Taking $\boldsymbol{O}$ as the origin of the reciprocal space, then draw the vector $\boldsymbol{CO}=-\boldsymbol{So}/\lambda$. Using $\boldsymbol{C}$ as the center to draw a sphere of radius $1/\lambda$, then define the reciprocal point $\boldsymbol{R}$ by the vector $\boldsymbol{CR}=\boldsymbol{S}/\lambda$, thus $\boldsymbol{OR}=(\boldsymbol{S}-\boldsymbol{S_O})/\lambda=\boldsymbol{Q}$. This sphere is called the Ewald sphere as shown in Fig. 2-3. $\boldsymbol{CR}$ is the direction of the diffraction planes whose corresponding reciprocal point is $\boldsymbol{R}$.

Since the length of $\boldsymbol{OR}$ is equal to the $1/d_{hkl}$, where d_{hkl} is the distance between the planes with Miller indices as *hkl*, thus

$$2\sin\theta = \frac{\lambda}{d_{hkl}} . \quad (2\text{-}2)$$

Equation 2-2 is the well-known Bragg diffraction equation.

Sharp peaks at different 2θ values representing planes can be found in the XRD patterns of crystalline materials. However, for amorphous or glassy materials, only broad peaks can be observed in their XRD patterns. Accordingly, usually the number and breadth of the peaks in the XRD patterns can be used as the basic index to judge the structures of the materials. Furthermore, the total structure factor can be calculated from the

measured scattering intensity. By using Fourier transformation to convert the structure factor into real space atomic density distribution, the total-scattering pair distribution function (PDF) can be obtained [99].

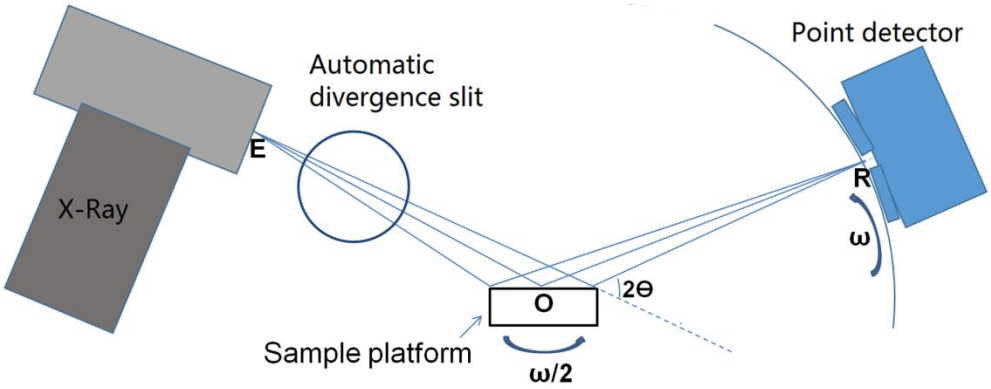

Figure 2-4. Schematic of an X-ray diffractometer.

Figure 2-4 shows the schematic of a typical X-ray diffractometer. The point detector and X-ray source can move around the sample platform to adjust the converging incident X-ray beam so as to focus on the sample surfaces. The distance OE is equal to the distance OR. During the measurement, the detector turns at an angular velocity ω, while the angular velocity of the sample platform is ω/2. In addition, the detected sample volume can be kept constant during the illumination process independent of the diffraction angle, by adjusting the incident beam with the automatic divergence slit.

2.1.3 Transmission electron microscopy

Transmission electron microscopy (TEM) [98] is a technique widely used to characterize specimens at very high magnification. The basic principle of TEM is the interaction between the transmitted electrons with the ultra-thin specimen through which they are transmitted. By interaction of the electrons with the specimen, images are formed, which can be magnified and focused by imaging devices or be detected by a sensor like a charge-coupled device. Typically, the transmitted electron image of a thin specimen has a resolution of 2 Å, which is due to the small De Broglie wavelength of the electron.

When a beam of high energy electrons interacts with a material, elastic or inelastic scattering takes place. In inelastic scattering, the energy and momentum of the electron waves are reduced, which represents a characteristic of the elements with respect to their inner shell ionization. The flight path of the electrons beam emerging from the sample can be varied by using a magnetic prism due to their different energies, this technique can be used to obtain the electron energy loss spectroscopy (EELS) spectra. However, if an adjustable slit is used to allow electrons with a certain range of energies to pass through the samples, then an image can be

reformed based on the detected electrons. This technique used in TEM is called energy-filtered transmission electron microscopy (EFTEM) and can be used to perform chemical analysis of the sample.

In contrast to the conventional transmission electron microscopy, which forms images by electrons that are transmitted through a thin sample, a scanning transmission electron microscope focuses the electron beam to a spot, which is then scanned over the sample. Scanning transmission electron microscopy is suitable for analytical techniques such as energy dispersive X-ray spectroscopy (EDX) mapping and EELS mapping. Conventional transmission electron microscope can be switched into scanning transmission electron microscope by equipping it with additional scanning coils, detectors and circuitry.

Transmission electron microscopy can also be applied to observe the structure of crystals at the atomic level directly, and their 3-D structure can be derived by the projected 2-D images [98]. However, since the packing of atoms in glasses are disordered and isotropic, thus the direct observation of atomic structure of glasses is unavailable [100]. Also, there are many artifacts that may be introduced during the processing of TEM samples, such as oxidation, crystallization, deformation, etc. Since these drawbacks are hard to avoid, MG structures cannot be quantitatively studied by TEM imaging analysis. Nevertheless, the structural information of glasses can be studied in another way by ED.

The principle of ED is similar to that of XRD, and the ED can also provide similar information as the XRD. By converting the ED spectrum into structure factor and PDF (or RDF), the atomic level structure of glasses can be learned. In addition, since TEM can probe the structure of materials in a very small region, the localized structural fluctuations in MGs can be identified. For example, recently, Hirata et al. successfully obtained the SRO in MGs by using the spherical aberration-corrected TEM [38,39].

2.1.4 Small-angle X-ray scattering

Small-angle X-ray scattering has been shown to be a powerful technique for detection of the electron density profiles of particles [101, 102]. Small-angle X-ray scattering technique is based on the elastic scattering of X-rays by materials with inhomogeneous electron densities in the nanometers range. These scattered X-rays are recorded at very low angles (normally 0.1 to 5°) to form the SAXS spectra. Different electron densities result in the different X-ray scattering behavior, thus based on the intensity and/or angular range of X-ray scattering, the information such as the averaged particle size, shapes, aggregation of the particles and so on can be obtained. The X-ray source can be a laboratory X-ray source, such as the Cu or Mo radiation sources are widely used. However, in order to get high resolution measurements, synchrotron light should be considered due to its higher X-ray flux.

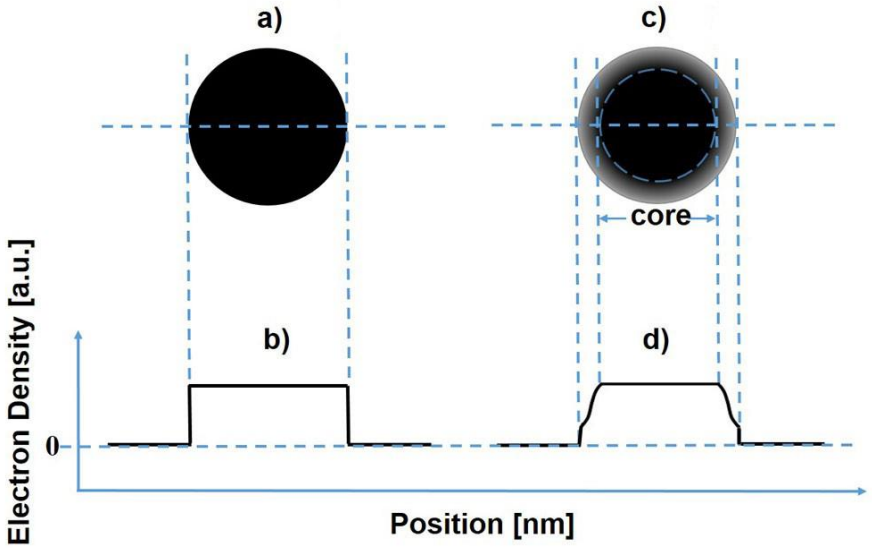

Figure 2-5. Schematic representation of the electron density profiles of nanoparticles. (a) Nanoparticle with a homogeneous chemical composition and atomic packing density profile. (b) Electron density profile of the nanoparticle shown in (a). (c) Nanoparticle with a homogeneous chemical composition but gradually reduced atomic packing density shell. (d) Electron density profile of the nanoparticle displayed in (c). [102]

The scattering intensity at large values of the scattering vector q can be described according to a power law [103]:

$$I(q) \propto q^{-a}, \qquad (2\text{-}3)$$

where $q = (4\pi/\lambda) \cdot \sin\theta$, λ is the wavelength of the incident X-ray beam, and θ is half of the scattering angle. For nanoparticles with a homogeneous chemical composition and atomic packing density (APD) profile (Fig. 2-5a), corresponding to a stepwise like electron density profile (Fig. 2-5b), the scattering intensity is given by Porod's law with a=4. However, the existence of diffuse atomic shells (Fig. 2-5c) with a gradient of the APD on the particle surface causes a deviation from Porod's law resulting in a>4. Accordingly, the electron density profile on the particle surface does not show a stepwise behavior, but instead changes gradually from the perimeter of the core to the surface of the particle (Fig. 2-5d) [101, 102]. Based on the sigmoidal electron density gradient model, the thickness of the shell with a lower electron density can be calculated [102, 104].

Guo et al. [102] used the sigmoidal electron density gradient model to reveal the diffuse shell structure of metallic crystalline nanoparticles, which were synthesized by electric discharge in an inert gas atmosphere. The thicknesses of the diffuse shells were deduced from the SAXS measurements and confirmed by transmission electron microscopy.

2.1.5 Mössbauer spectroscopy

Mössbauer spectroscopy (MS) [98] is a kind of spectroscopic technique based on the Mössbauer effect. The Mössbauer effect was named after its discoverer Rudolf Mössbauer and is the resonant absorption of gamma rays by some solids due to the recoil-free emission of gamma rays.

Mössbauer spectroscopy is a very sensitive technique, which can be used to detect very small changes in the environments around the nucleus. Three important interactions between the nucleus with their environment have been observed, namely, the isomer shift (δ), quadruple splitting and hyperfine splitting. The interaction between the nucleus with the *s*-electrons results in the isomer shift. The whole spectrum shifts in a positive or negative direction depending on the density of *s*-electrons. The interaction between the nucleus and their surrounding electric field gradient results in the quadruple splitting. Hyperfine splitting, which is also called magnetic splitting, represents the interaction between the nucleus and their surrounding magnetic field.

Since MS can detect tiny changes of electron density variation around the probe atoms, it is widely used to investigate the atomic or electronic structure of interfaces within bulk nanostructured materials. For instance, the lower electron density of the interfaces (grain boundaries) for bulk nanostructured Fe was detected by MS [105]. In addition, the width of the grain boundaries can also be measured [106]. Recently, MS was applied to $Fe_{90}Sc_{10}$ nanoglasses, and it was found that the spectrum of the interfaces is totally different from the spectrum of the cores [7, 84].

2.2 Experimental procedures

XRD characterization

The XRD samples were prepared in the glove-box filled with high purity Argon. The GNp or the nanoglass pellets were sealed in the sample cover filled with Argon gas. The sample cover consists of a silicon substrate, which was covered by a plastic dome. The dome and the substrate both exhibit no diffraction peaks in the 2θ range from 10-50^{o} of Mo-XRD, i.e., the peaks, which were observed from the XRD all belong to the analyzed samples. In contrast, the melt spun ribbon samples were prepared in the air. They were cut into pieces of approximately 2 cm in length and attached onto the substrate directly to perform the XRD measurements.

The XRD patterns were recorded on a Philips X'Pert Panalytical diffractometer using Mo-Kα radiation (step size=0.02^{o}, integration time 15 s/step.). Prior to the start of the X-ray scanning, the height of the sample substrate was carefully calibrated to determine the exact position and intensity of the diffraction peaks.

TEM characterization

The primary GNp for TEM measurements were collected directly by attaching a carbon coated TEM grid onto the cold finger of the IGC apparatus. The thin lamella of the $Fe_{90}Sc_{10}$ nanoglasses for TEM analysis was prepared by focused ion beam (FIB, FEI Strata 400 S) cutting from the NG pellets and finally thinned using a Nanomill (Fischione) at a low voltage of 600 V.

The FEI Titan 80 - 300 electron microscope (FEI Co., Hillsboro, OR, USA) used was equipped with a CEOS image spherical aberration corrector, Fischione model 3000 high angle annular dark field (HAADF) STEM detector, an EDAX-SUTW EDX detector and a Gatan Tridiem image filter.

The electron microscope was operated at an accelerating voltage of 300 kV in the TEM mode for HRTEM, and in the nanoprobe mode for STEM imaging and EELS spectra acquisition. In addition, the Fe and Sc maps were acquired with the Gatan image filter in the EFTEM mode.

SAXS characterization

Specimens for SAXS measurement were prepared in the glove-box filled with high purity Argon. The GNp for SAXS measurements were synthesized at the same time. A fraction of the GNp was sealed between two Kapton foils. The rest of the GNp was compacted at a uniaxial pressure of 500 MPa into a thin pellet with residual porosity, called "compacted GNp" in the following. Subsequently, the compacted GNp were sealed in between two Kapton foils as well. The X-ray scattering intensity originating from the Kapton foils was recorded by measuring blank Kapton foils without a specimen. This scattering contribution originating from the Kapton foils was subtracted in the subsequent data evaluation.

Measurements were carried out at a laboratory temperature around 20 °C. During the measurement, the specimens were kept in a vacuum condition with a pressure lower than 1 mbar, since the air molecules may affect the scattering.

The details of the SAXS/WAXS equipment used, the method applied for the data collection as well as the data processing were reported elsewhere [102].

Ex situ annealing of the $Fe_{90}Sc_{10}$ NG pellet in UHV tube-furnace

The $Fe_{90}Sc_{10}$ nanoglass pellet for the annealing experiments were mechanically polished to remove the oxide layers and placed in a ceramic boat in the UHV tube-furnace. When the vacuum pressure at room temperature was pumped to 1×10^{-8} mbar, the tube-furnace was quickly heated to the target temperature and temperature and maintained at that temperature for the desired time.

During one annealing experiment, the same pellet was heated from room temperature to the desired temperatures (150, 200 and 250 °C) and annealed for 2 hours at each temperature. In between, XRD were recorded at room temperature, and the Mössbauer spectroscopy was performed at 20 K.

Mössbauer spectroscopy characterization of $Fe_{90}Sc_{10}$ NGs

The $Fe_{90}Sc_{10}$ NG pellets for MS characterization was mechanically thinned to about 60 μm in thickness. Mössbauer spectroscopy was performed using a standard transmission setup with a ^{57}Co Rh source in a linear acceleration mode. The spectra were measured with the external field perpendicular to the γ-ray. The isomer shift (IS) is given relative to bcc-Fe at room temperature. In addition, every time the sample was irradiated in the MS for a long time until the resolution spectra are obtained.

In situ annealing of the $Fe_{90}Sc_{10}$ NG lamella in transmission electron microscope

The same lamella specimen, used to perform the EELS mapping, was examined in this experiment. After obtaining some basic information at room temperature, such as the ED, STEM and HRTEM images, the lamella specimen was heated to the desired temperatures at a constant heating rate (5 °C/s). After annealing at 150, 200 and 250 °C for half an hour at each temperature, the STEM and ED patterns of the lamella specimen were recorded.

3 Results and Discussion

3.1 Atomic structure of $Fe_{90}Sc_{10}$ glassy nanoparticles and nanoglasses

3.1.1 Surface segregation of the primary glassy nanoparticles

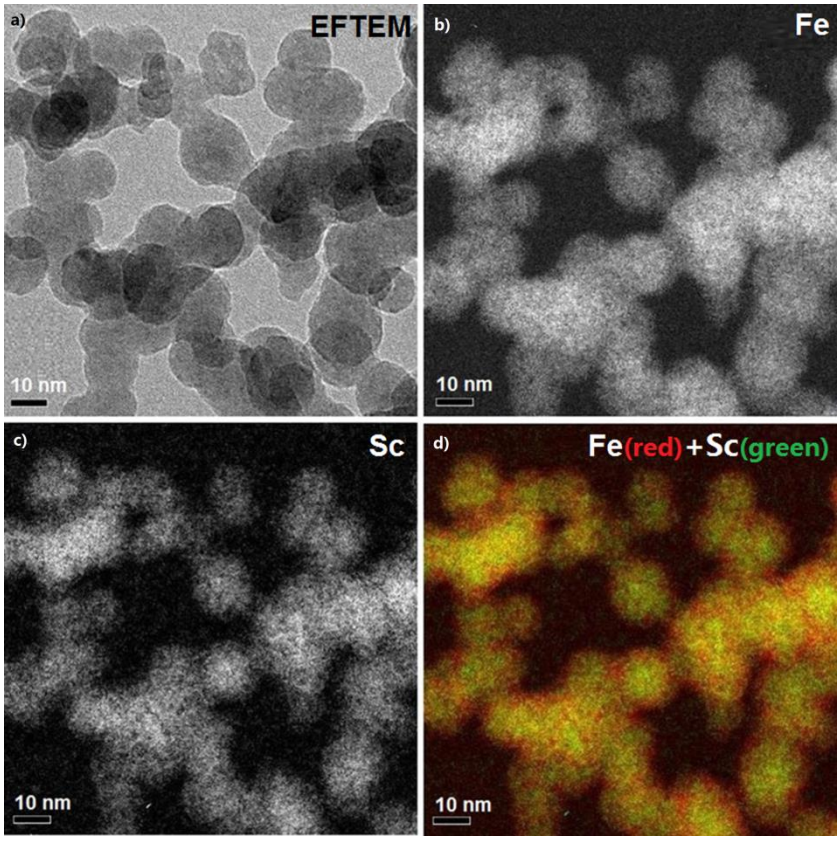

Figure 3-1. EELS mapping of Fe and Sc in the primary $Fe_{90}Sc_{10}$ GNp. (a) EFTEM image, (b) Fe map, (c) Sc map. (d) was obtained by overlapping (b) and (c), and red color represents Fe, while green color represents Sc.

The EFTEM image of the primary GNp that was used to perform the elemental mapping is shown in Fig. 3-1a. The Fe and Sc maps for the primary GNp are shown in Fig. 3-1b and 3-1c, respectively. Comparison of the results in Fig. 3-1a with those in Fig. 3-1c reveal that on average the diameter of the Sc particles is smaller than that of the primary particles, whereas the diameter of the Fe particles is as large as that of the primary particles (Fig. 3-1b). These observations indicate that the Sc concentration at the surfaces of the $Fe_{90}Sc_{10}$ primary GNp is too low to be detected. The image presented in Fig. 3-1d, obtained by overlapping the images in Fig. 3-1b and

3-1c, confirms that Fe is concentrated on the surface of the GNp. Such segregation of the majority component to the free surface has also been found in $Sc_{75}Fe_{25}$ GNp, as shown in Fig. 3-2, the Sc tends to segregate to the surface, thus the Fe concentration in the shell of the $Sc_{75}Fe_{25}$ GNp is lower than in the core [6, 107].

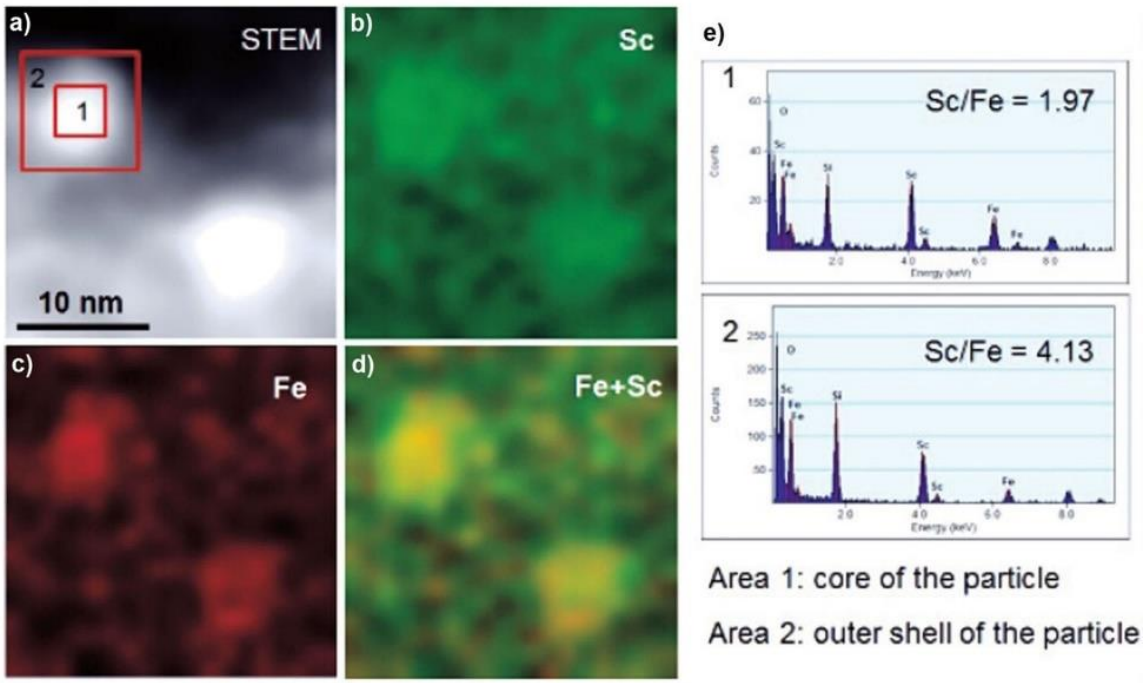

Figure 3-2. EDX mapping of Fe and Sc in the primary $Sc_{75}Fe_{25}$ GNp. (a) STEM image, (b) Sc map, (c) Fe map. (d) was obtained by overlapping (b) and (c), red color represents Fe, while green color represents Sc. (e) are the integrated EDX spectra of the core (spectrogram 1) and of the shell (spectrogram 2). [107]

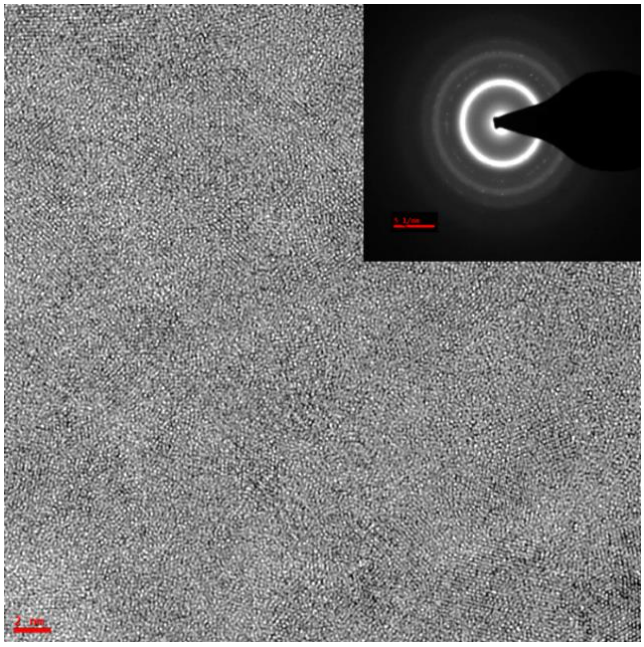

Figure 3-3. HRTEM of the $Fe_{90}Sc_{10}$ NG, the insert is the selected area ED (SAED) image.

Electron energy loss spectra mapping of the $Fe_{90}Sc_{10}$ NG was performed to confirm the segregation behavior reported above and to investigate the structure of $Fe_{90}Sc_{10}$ NG. Prior to the EELS mapping, the HRTEM image of a $Fe_{90}Sc_{10}$ NG was required and is shown in Fig. 3-3. This image reveals the presence of some atomic lattices in the amorphous matrix, which indicates that the $Fe_{90}Sc_{10}$ NG lamella is not totally amorphous, but has a small amount of nanocrystallites. These nanocrystallites are α-Fe, which have been confirmed by MS.

The granular structure of the NG is visible in the EFTEM micrograph displayed in Fig. 3-4a. The EELS mapping of each components was performed in the same manner as for the $Fe_{90}Sc_{10}$ GNp. Comparing the Fe and Sc maps, one can detect that the Fe distribution is nearly homogeneous throughout the NG. Accordingly, the boundaries between the "nanograins" are almost invisible (Fig. 3-4b). In contrast, the distribution of Sc (Fig. 3-4c) is heterogeneous and shows up in the form of the nanometer-sized "brighter dots" (indicated by the red arrows) connected by the darker areas. The "brighter dots" may represent the cores within NG containing more Sc, whereas the darker areas may represent the interfacial regions between the cores with less Sc. Thus, the heterogeneous structure of the $Fe_{90}Sc_{10}$ NG can be observed in Fig. 3-4d, which is created by superimposing Fig. 3-4b and Fig. 3-4c.

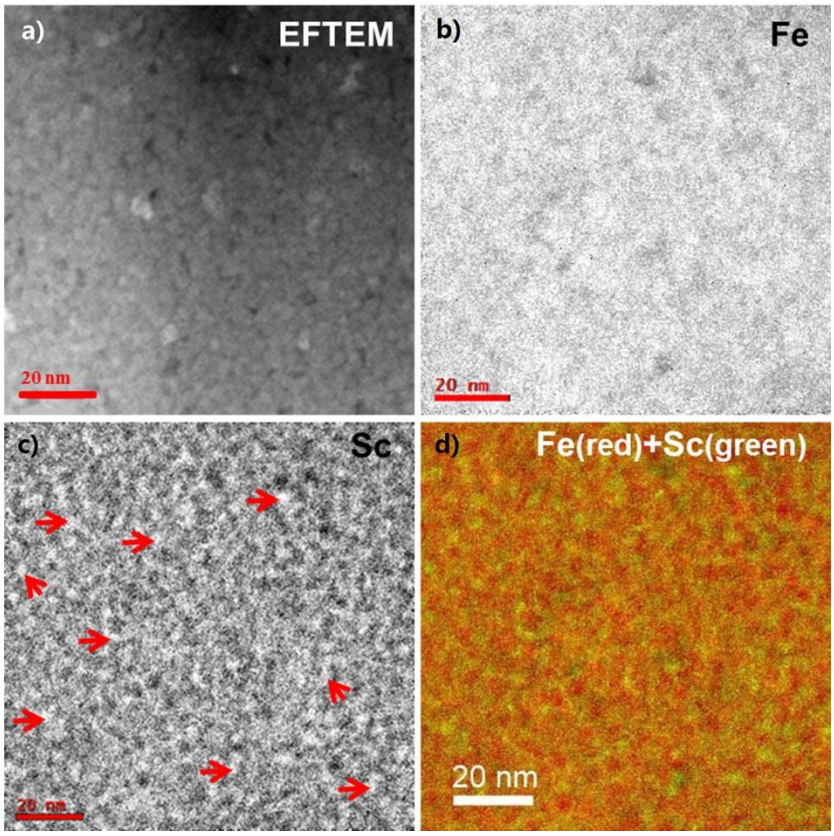

Figure 3-4. EELS mapping of Fe and Sc from the $Fe_{90}Sc_{10}$ NG. (a) EFTEM image; (b) Fe map; (c) Sc map, the "bright dots" indicated by the red arrows are the cores richer in Sc; (d) this image was obtained by overlapping (b) and (c), red color represents Fe, while green color represents Sc.

In order to understand the origin of the surface segregation of Fe-Sc GNp, a theoretical estimate of the chemical distribution based on a monolayer model has been carried out and was compared with the experimental results.

Monolayer models are known to be applicable to estimate the surface composition of the liquid binary alloys as well as of solid solutions of binary alloys [86, 87, 89, 108, 109]. In monolayer models, solid solutions of binary alloys are regarded as regular solutions. The surfaces of binary alloys are modeled as a monolayer and the compositional variations are assumed to be limited to the topmost monolayer. The driving force for surface segregation depends on two distinct contributions [86-88]. One contribution results from the different surface energies of the two pure components. The second component depends on the heat of mixing, ΔH, of both components, or the degree of negativity of ΔH_{mix}. Since binary MGs are metastable frozen liquid alloys [110], their atomic structures may be approximated by the structures of the corresponding molten state [111]. In other words, they could be treated as solid solution of binary alloys fitted to the monolayer model.

The equation derived from the monolayer model may be written in the following form [109]:

$$\frac{X_1^{\,i}}{X_1^{\,s}} = \frac{X_2^{\,i}}{X_2^{\,s}} \exp\left(\frac{S_1 - S_2}{RT}\right) f(W) \quad . \tag{3-1}$$

$X_1^{\,s}$and $X_1^{\,i}$ are the molar fraction of component "1" on the surface and the interior of the binary liquid alloy, respectively. $X_1^{\,S}+X_2^{\,S}=1$, $X_1^{\,i}+X_2^{\,i}=1$. S_1 and S_2 are the molar pure-component surface energies of 1 and 2, respectively. R is the gas constant, T is the absolute temperature. $f(W)$ is the regular solution function for the heat of mixing components and can be derived by equation as:

$$f(W) = \exp\left\{\frac{W(l+m)}{RT}\left[\left(X_1^{\,i}\right)^2 - \left(X_2^{\,i}\right)^2\right] + \frac{Wl}{RT}\left[\left(X_2^{\,s}\right)^2 - \left(X_1^{\,s}\right)^2\right]\right\} \tag{3-2}$$

Here, W is defined as $W = z(E_{12} - (E_{11}+E_{22})/2)$, and z is the total number of next-neighbor contacts. E_{11}, E_{22} and E_{12} are the bond energies, where, E_{11} can be defined as the bond energy between per mole atoms of component 1 and similarly E_{22} and E_{12}. For ideal solution, W=0 and $f(w)$=1. l and m denote the fractions of the total next-neighbor contacts made by an atom with its own layer and neighboring next layer. Accordingly, the total number of next-neighbor contacts of the interior atom is $(l+2m)z$, while that of the surface layer is $(l+m)z$, and $(l+2m)=1$ [108].

The molar surface energies of pure Fe and pure Sc can be calculated based on the relationship between the surface energy and the heat of sublimation as $S = 0.16\ \Delta H^{sub}$ [89]. The heat of sublimation for Fe and Sc are taken from the literature as ΔH^{sub}_{Fe} = 415.50 kJ mol^{-1} [112] and ΔH^{sub}_{Sc} = 381.70 kJ mol^{-1} [113]. The obtained value after calculating the surface energy of Fe and Sc is S_{Fe} = 66.48 kJ mol^{-1} and S_{Sc} = 61.07 kJ mol^{-1}, respectively.

The term W can be derived from the heat of mixing of Fe with Sc above as $W = \Delta H^{mix}/X_{Fe}^{\,i}X_{Sc}^{\,i}$ [114], where ΔH^{mix} = -11.28 kJ mol^{-1} [115]. The choice of l and m values depends on the atomic packing manners [116]. In the glassy state, the atoms are treated as randomly distributed in a nearly closed packed structure [117]. Accordingly l = 0.5, and m = 0.25 are always chosen for the binary MG and liquid alloys [108, 116]. However,

due to the relaxation effect, it was proposed to use l = 0.75 instead of l = 0.5 [118]. Furthermore, according to RDF of $Fe_{90}Sc_{10}$ NG, the number of next-neighbor contacts of Fe at the interfaces and cores are 9.1 and 10.5, respectively [8]. Thus, the values of l = 0.75 and m = 0.125 could be calculated from:

$$\left.\begin{aligned}(l+m)z &= 9.1\\ (l+2m)z = z &= 10.5\end{aligned}\right\} \qquad (3\text{-}3)$$

After substituting the values in equation 3-1 and taking $X_1^i = X_{Fe}^i$ as independent variable and $X_1^s = X_{Fe}^s$ dependent variable, the plotted results are shown in Fig. 3-5.

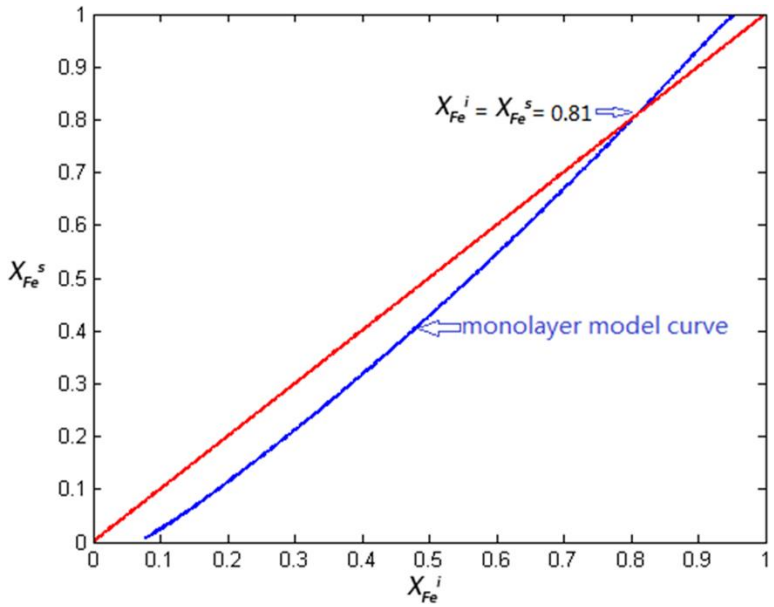

Figure 3-5. Plot obtained by calculating the Fe composition on the surface versus Fe composition on the interior of Fe-Sc MG based on the monolayer model.

As can be seen from Fig. 3-5, the red line represents no surface segregation, i.e., $X_{Fe}^s = X_{Fe}^i$. The theoretical values (blue curve) characterized by the Fe concentration below the intersection ($X_{Fe}^s = X_{Fe}^i$=0.81) imply that the Fe atoms accumulate in the interior of the Fe-Sc MG. The opposite applies to Fe-Sc MG with Fe concentration above the intersection. In these MG, the Fe concentration is enhanced in the surface regions. Obviously, in Sc rich MG, segregation of the majority component happens for all compositions. However, in Fe rich MG, the majority component Fe starts to segregate only when the Fe concentration is above the intersection. Clearly, this result is consistent with the experimental observations for $Sc_{75}Fe_{25}$ and $Fe_{90}Sc_{10}$ GNp, i.e. Sc atoms segregate to the surfaces of $Sc_{75}Fe_{25}$ GNp while Fe atoms prefer to segregate to the surfaces of $Fe_{90}Sc_{10}$ GNp.

In conclusion, the tendency of the blue curve could be simply explained as the combined effects of the two kinds of driving forces for surface segregation. Since Sc has a lower surface energy, the reduction of the surface energy provides the driving force for the segregation of the Sc to the surfaces. However, the driving force resulting from the reduced energy of the Fe-Sc bond will provide a driving force for moving the minority components into the interior of the GNp. Therefore, by changing the composition of Fe-Sc MG, these two

driving forces are balanced against each other and result in the experimentally observed different surface segregation for different chemical compositions.

Since the Fe-Sc NG were produced by consolidation of primary GNp, the surface segregation effect in the primary GNp controls the chemical composition of the interfaces of the as-consolidated NG. A similar phenomenon has been observed in $Fe_{50}B_{50}$ GNp, whose B enriched surfaces are transferred into the $Fe_{50}B_{50}$ NG to form the B enriched interfaces.

Recently, Danilov [11] and Adjaoud [12] simulated the atomic structure of binary GNp and the corresponding NG, and both produced results that are consistent with those obtained in the present work. They found that the surfaces of the GNp are enriched with the majority components, and these surfaces are transferred into the interfaces to form interfaces enriched with majority component.

Moreover, it can be expected that the surface segregation behavior of other binary GNp can be estimated using thermodynamics. As the composition of the surface of the primary GNp can be transferred into the NG, the composition of the interfaces can also be estimated. However, the molar surface energy of the nanoparticles decreases with the decrease of the nanoparticle diameter over a wide-size range, and the sharp drop of the molar surface energy normally occur in the nanoparticles with a diameter smaller than 6 nm [119-122]. Thus, for the ultra-small GNp, the size effect on the molar surface energy should be considered in the thermodynamic calculations to obtain more accurate results. Since the average diameter of the $Fe_{90}Sc_{10}$ GNp is about 12 nm (Fig. 3-1a and Fig. 3-6b) in the present work, for the sake of the simplicity, the minor size effect on the molar surface energy was ignored.

3.1.2 Low packing density shells of the glassy nanoparticles

Figure 3-6a shows the WAXS curves of the primary $Fe_{90}Sc_{10}$ GNp, of the compacted $Fe_{90}Sc_{10}$ GNp and of the blank Kapton foils. Obviously, the peaks at 33^o and 65^o result from the scattering of the Kapton foils. The broad peak visible at 44.5^o was attributed to the $Fe_{90}Sc_{10}$ glassy state because it coincides with the scattering angle of a $Fe_{90}Sc_{10}$ glass, which was prepared by melt spinning. The amorphous state of all samples can be concluded from the broad peaks visible at 44.5^o.

After subtraction of the background scattering, the SAXS curve of the $Fe_{90}Sc_{10}$ GNp is shown in Fig. 3-6b together with fits according to two power-law regions and one Guinier region in between. The scattering intensity in the Guinier region of scattering vector q is expressed as follows [123]:

$$I(q) = G \cdot \exp\left(-R_g^2 \cdot q^2/3\right), \qquad (3\text{-}4)$$

where G is the Guinier pre-factor, and R_g is the radius of gyration of the particles. Based on the value of R_g, the geometric diameter d_p can be calculated from equation (3-5) [123]:

$$d_p = 2\sqrt{5/3}R_g\,. \qquad (3\text{-}5)$$

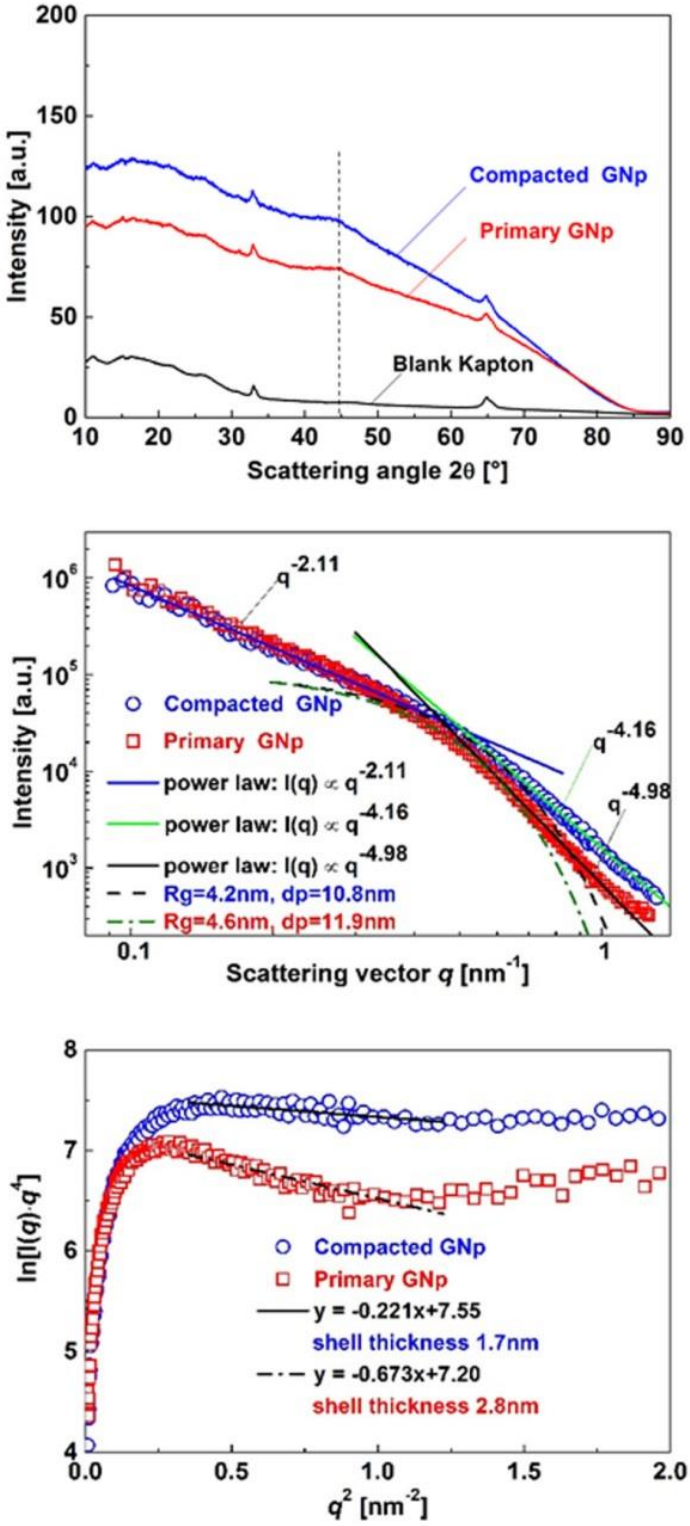

Figure 3-6. Small- and wide- angle X-ray scattering results of the primary and of the compacted $Fe_{90}Sc_{10}$ GNp. (a) Scattering intensity measured with WAXS, the black line stands for the intensity scattered by the Kapton foil only, the red and blue lines display the intensities scattered of the primary and the compacted $Fe_{90}Sc_{10}$ GNp, respectively. (b) Small-angle X-ray scattering (SAXS) curves; (c) Plots of $\ln\left[I(q)\cdot q^4\right]$ versus q^2 for determining the thicknesses of the primary and the compacted GNp.

By using this approach, the diameter of the primary GNp was deduced to be 11.9 nm. This value is close to the values obtained from electron transmission microscopy (Fig. 3-1a). After compaction, the diameter of the scattering units decreases slightly to 10.8 nm.

The scattering intensity decays at larger q values, following a power law with an exponent greater than four ($\alpha>4$), in agreement with the electron density profile as shown in Fig. 2-5d. This indicates that the surface shells of $Fe_{90}Sc_{10}$ GNp are characterized by a reduced electron density.

According to the sigmoidal electron-density gradient model [102, 124], the following relationship applies:

$$\ln\left[I(q)\cdot q^4\right]=\ln K_P-\sigma^2\cdot q^2, \qquad (3\text{-}6)$$

where K_p is the Porod-law constant, and σ is the standard deviation of the Gaussian smoothing function (the detailed meaning of σ can be found elsewhere [102]). The plot of $\ln\left[I(q)\cdot q^4\right]$ versus q^2 exhibits a linear decay at large values of the scattering vector q, which may be fitted by a straight line with a slope of $-\sigma^2$ (Fig. 3-6c).

From this result, the thickness of the surface shell (T_s) with a reduced electron density profile can be calculated as [102]:

$$T_s=2\sqrt{3}\sigma\ . \qquad (3\text{-}7)$$

For the primary GNp, the thickness of the shells was found to be 2.8 nm. Considering the radii of the scattering unit determined above, the diameter of the cores is 6.3 nm. For the compacted GNp, the thickness of the shells is 1.7 nm.

The electron density (ρ_e) of the Fe_xSc_{100-x} glass can be estimated as:

$$\rho_e=\frac{N_e}{V_{MG}}=\frac{N_A\cdot\frac{x}{100}\cdot Z_{Fe}+N_A\cdot\frac{100-x}{100}\cdot Z_{Sc}}{V_{MG}}, \qquad (3\text{-}8)$$

where N_e is the total number of the electrons of Fe_xSc_{100-x} glass, V_{MG} is the volume of Fe_xSc_{100-x} glass. N_A is the total number of the atoms of Fe_xSc_{100-x} glass. Z_{Fe} and Z_{Sc} represent the number of electrons of one Fe atom (Z_{Fe} = 26) and one Sc atom (Z_{Sc} = 21), respectively.

The APD (ρ_f) of the Fe_xSc_{100-x} glass is given by:

$$\rho_f=\frac{V_t}{V_{MG}}=\frac{N_A\cdot\frac{x}{100}\cdot V_{Fe}+N_A\cdot\frac{100-x}{100}\cdot V_{Sc}}{V_{MG}}\ , \qquad (3\text{-}9)$$

where V_t is the total volume of the atoms of Fe_xSc_{100-x} glass, V_{Fe} and V_{Sc} represent the volume of one Fe atom and one Sc atom, respectively. $V_{Fe}=4/3\pi\langle R_{Fe}\rangle^3$, where R_{Fe} is equal to the 12-fold-coordinated Goldschmidt atomic radii of Fe [125]. R_{Fe}=127.4 pm, R_{Sc}=164.1 pm [126]. Thus, equation (3-8) can be reduced to:

$$\rho_e=\frac{(2100+5x)\cdot10^{24}}{1850-9.8x}\cdot\rho_f/cm^3. \qquad (3\text{-}10)$$

From equation (3-10), it is evident that there are two factors that may cause an electron density (ρ_e) gradient of the $Fe_{90}Sc_{10}$ GNp. The first factor is the variation of the Fe concentration (x) due to a surface segregation effect. The second factor is the variation of the APD (ρ_f).

Since the Fe concentration in the surface shells is larger than that in the cores of $Fe_{90}Sc_{10}$ GNp [127], the electron density of the shells is expected to be higher than the one in the cores (ρ_e increases as x increases). However, the electron density profile obtained from the SAXS data indicates the opposite, i.e., the electron density of the shells is found to be lower than the one of the cores. Consequently, the compositional variation due to the surface segregation effects cannot account for the experimentally observed electron density gradient of the $Fe_{90}Sc_{10}$ GNp. In other words, we are led to conclude that the lower electron density of the shells has to be caused by a lower APD.

If the cores of the primary $Fe_{90}Sc_{10}$ GNp have a similar APD to the corresponding MG and are considered to be not compactable at the employed pressures of only 500 MPa, then the volume of the primary shells before and after compaction are $V_p=4/3\pi[(11.9/2)^3-(6.3/2)^3]$ nm^3 and $V_c=4/3\pi[(10.8/2)^3-(6.3/2)^3]$ nm^3, respectively.

The APDs of the primary shells and the compacted shells, ρ_p and ρ_c, are given by $\rho_p=V_t/V_p$, $\rho_c=V_t/V_c$, respectively, where V_t is the total volume of the atoms of the shell. Thus, $\rho_p/\rho_c=V_c/V_p\approx70\%$, and subsequently $\rho_p\approx0.7\rho_c$. As the APD of the compacted shells is still lower than the one of the cores, it can be concluded that the primary shells have an atomic structure with a much lower APD than the particle cores. This reduced APD may originate from a large amount of extra free volume and under-coordinated atoms compared to the corresponding melt quenched glass.

Shells with reduced density of the GNp have been observed also in several computer simulations published by Hoang et al. [128-132] However, so far it has not been confirmed by experimental studies.

According to Hoang [131, 132], the atomic mechanism of glass formation in nanometer-sized droplets exhibits “heterogeneous vitrification” behavior, which differs from the “homogeneous vitrification” behavior of bulk glasses. In fact, the solid-like “glassy domains” are proposed to initiate in the interior of the droplets and simultaneously grow outward to the surfaces resulting in the GNp. During this glass formation process, the atoms diffuse inward to form the core region with APD larger than that of the corresponding melt quenched glasses, whereas the surface shells have an APD lower than that of the corresponding melt quenched glass.

3.1.3 Atomic structural model of $Fe_{90}Sc_{10}$ glassy nanoparticles and nanoglasses

Combing the chemical composition distribution with the atomic packing density, a proposed structural model of $Fe_{90}Sc_{10}$ GNp is shown in Fig. 3-7. It can be observed that the surface layer of the $Fe_{90}Sc_{10}$ GNp has a higher Fe concentration, while its atomic packing density is lower than the core. According to Hoang [128-132], the mean CN for atoms located in the shells of GNp is lower than the cores, which is in line with Liu et al. [133] that the low packing density area of MGs contain the loosely packed clusters with low CNs. Thus, it can be expected that the shells of the GNp may contain clusters with low CNs while the cores contain clusters with high CNs.

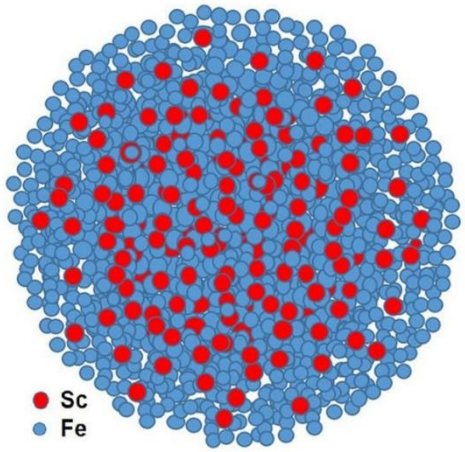

Figure 3-7. Proposed structural model of a $Fe_{90}Sc_{10}$ glassy nanoparticle. Fe concentration of the surface layers is higher than that of the interior regions due to the surface segregation; and the atomic packing density in the surface shell is lower than the one of the cores.

Since $Fe_{90}Sc_{10}$ NG are prepared by consolidation of $Fe_{90}Sc_{10}$ GNp, based on the results reported above about the structure of the $Fe_{90}Sc_{10}$ GNp, the following structural model of $Fe_{90}Sc_{10}$ NG is proposed and is shown in Fig. 3-8. The inhomogeneous elemental distribution and a fraction of free volume at the surface region of $Fe_{90}Sc_{10}$ GNp can be transferred into the NG during the consolidation of the GNp [6, 127]. During the consolidation process, the free volume within the low APD shells of primary $Fe_{90}Sc_{10}$ GNp may delocalize into the interfacial regions between the $Fe_{90}Sc_{10}$ GNp resulting in interfacial regions of lower APD in the $Fe_{90}Sc_{10}$ NG [11]. By applying different consolidation pressures, the volume fraction of the interfacial region of APD density in NG can be varied [6, 11]. Furthermore, since the low APD shells with different composition may contain the types of SRO (clusters), which are different from the types of SRO of the melt quenched glasses, it is most likely that

the SRO of low APD shells will also be decisive for the structure of the interfaces within the NG [10, 37, 51, 134-136].

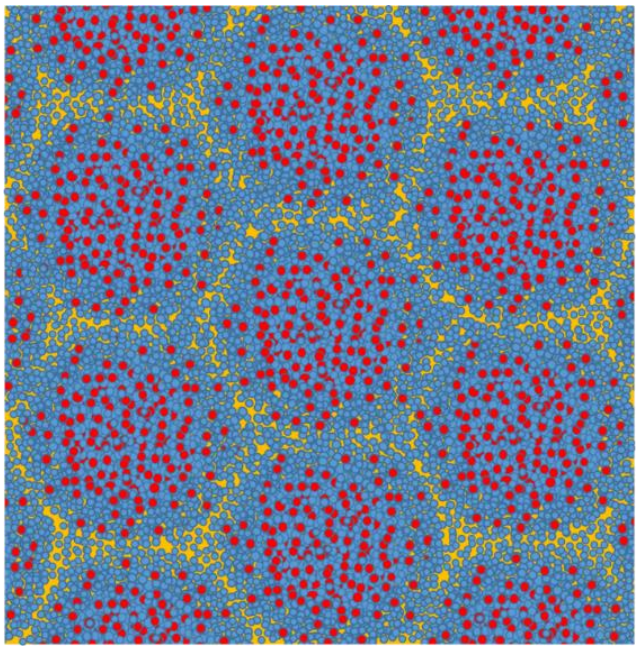

Figure 3-8. Proposed structural model of $Fe_{90}Sc_{10}$ nanoglass. The red spheres represent the Sc atoms, the blue spheres represent the Fe atoms. The chemical composition of the interfaces of the as-consolidated $Fe_{90}Sc_{10}$ nanoglass is controlled by the surface segregation effect of the primary $Fe_{90}Sc_{10}$ glassy nanoparticles. The yellow background represents the low density interfacial region.

3.2 Structural stability of $Fe_{90}Sc_{10}$ nanoglasses

The STEM images and ED patterns of the $Fe_{90}Sc_{10}$ NG specimens that were annealed in the transmission electron microscopy are displayed in Fig. 3-9. The STEM images (Fig. 3-9a) reveal that the specimens keep their granular appearance. In fact, no change in the size of the "nanograins" was noted during annealing indicating the stability of the nanostructure of $Fe_{90}Sc_{10}$ samples [7].

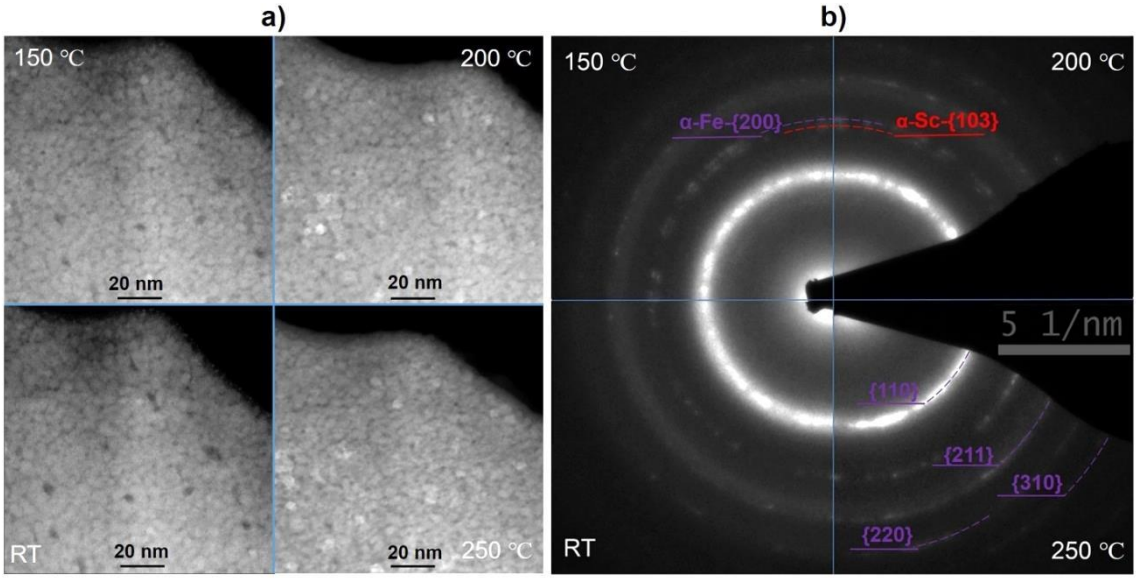

Figure 3-9. STEM images and ED patterns of $Fe_{90}Sc_{10}$ NG lamella under in-situ annealing. (a) STEM images, (b) ED patterns corresponding to the STEM images.

The ED patterns (Fig. 3-9b) corresponding to the STEM images show the structural evolution of the $Fe_{90}Sc_{10}$ NG samples. Briefly, the $Fe_{90}Sc_{10}$ NG lamella crystallized into a metastable nanocrystalline bcc-Fe (Sc) when it was heated from room temperature to 250 °C. During this process, some α-Sc nanocrystallites were semi-coherently precipitated from the bcc-Fe(Sc) nanocrystallites (crystalline cores) [137], which were indicated by the extra diffraction rings near the {200} diffraction rings of the bcc-Fe(Sc) nanocrystallites (see "150 °C" and "200 °C" ED patterns).

In order to ascribe the extra diffraction rings on the ED patterns (Fig. 3-9b-150 °C; Fig. 3-9b-200 °C) to the correct phase, the ED patterns were transformed into the intensity profiles as plotted in Fig. 3-10a. The extra rings corresponds to the humps near the {200} peaks of α-Fe (bcc-Fe). Moreover, there are small extra humps, which were indicated by the dashed circles can be observed in both the 150 °C and 200 °C intensity profiles. According to the positions of these humps in the intensity profiles, and combined with the atomic position

models, which were generated by Diamond software (Fig. 3-10b), the extra rings in the ED patterns can be indexed to the {103} lattices of **α**-Sc (hcp-Sc, PDF#17-0714).

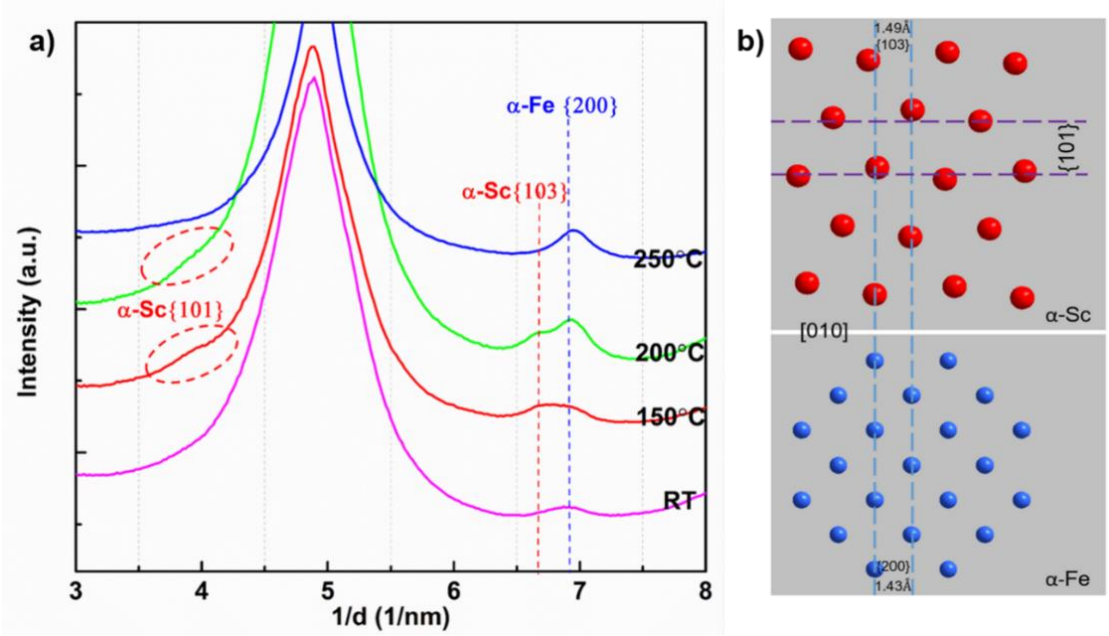

Figure 3-10. (a) Electron diffraction intensity profiles, which were translated from the ED patterns of $Fe_{90}Sc_{10}$ NG. (b) Atomic position models of the α-Sc and α-Fe lattices.

To clarify the underlying mechanism for the formation of the metastable **α**-Sc nanocrystallites, the Gibbs free energy of formation versus the composition diagram for the Fe-rich Fe-Sc amorphous alloys and the bcc-Fe(Sc) crystals was constructed (Fig. 3-11).

The molar Gibbs free energy of formation for a Fe-Sc alloy (ΔG) can be estimated by:

$$\Delta G = \Delta H - T\Delta S\,, \qquad (3\text{-}11)$$

The enthalpy of mixing ΔH can be calculated by Miedema's model [139-143]. The enthalpy of mixing ΔH_s for a bcc-Fe(Sc) crystals is:

$$\Delta H_S = \Delta H^c + \Delta H^e + \Delta H^s\,, \qquad (3\text{-}12)$$

where, ΔH^c, ΔH^e are chemical and elastic contributions, respectively. ΔH^s is the structural contribution , which is a small contribution and be neglected in the estimation [144]. The enthalpy of mixing ΔH_a for a Fe-Sc amorphous alloy can be estimated by:

$$\Delta H_a = \Delta H^c + \alpha\left(X_{Fe}\,T_{m,Fe} + X_{Sc}\,T_{m,Sc}\right)\,, \qquad (3\text{-}13)$$

where, α is a constant, $T_{m,Fe}$ is the melting temperature. The entropy of mixing for the Fe-Sc amorphous alloys and bcc-Fe(Sc) crystals can be given by the equation as:

$$\Delta S = -R\left(X_A \ln X_A + X_B \ln X_B\right), \qquad (3\text{-}14)$$

where, R is the gas constant.

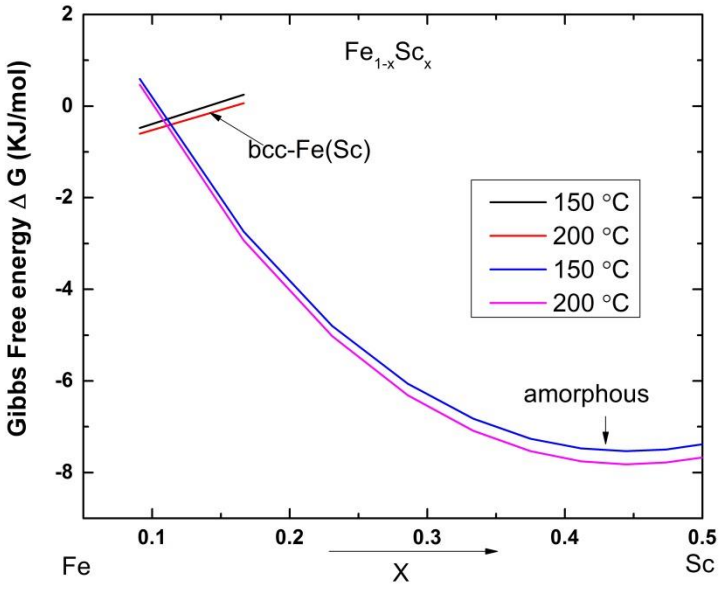

Figure 3-11. Theoretical calculated Gibbs free energy of formation versus the composition diagram for the Fe-rich Fe–Sc amorphous alloys and bcc-Fe(Sc) crystals at 150 °C (black lines) and at 200 °C (red lines).

In Fig. 3-11, the variation of the Gibbs free energy of formation versus the composition for the Fe-Sc amorphous alloys and the bcc-Fe(Sc) crystals at 150 °C and 200 °C are indicated by the black and red lines, respectively. For the $Fe_{90}Sc_{10}$ alloys at 150 °C and 200 °C, the Gibbs free energy of formation for the amorphous alloys is higher than that for the bcc-Fe(Sc) alloy, which implies that the polymorphous transformation of amorphous alloy to ultra-supersaturated bcc-Fe(Sc) crystal can occur by annealing. Additionally, in the case of $Fe_{90}Sc_{10}$ nanoglass, the stored energy of the interfaces and the extra potential energy that results from the high-pressure consolidation [74] should be considered, thus the Gibbs free energy of nanoglass should be higher than the normal glass.

The stability condition for a binary amorphous alloy can be estimated by [145]:

$$\psi = \frac{\partial^2 G}{\partial X_B^{\,2}} \quad . \qquad (3\text{-}15)$$

For Fe rich Fe-Sc amorphous alloys at 150 °C and 200 °C, Ψ>0, which means that any composition fluctuation will result in an increase of the free energy. Accordingly, the Fe-rich Fe-Sc amorphous alloys tend to form alloys with homogeneous composition instead of undergoing phase separation to precipitate α-Sc nanocrystallites, i.e., the metastable α-Sc nanocrystallites are not the decomposition product of the Fe-Sc amorphous alloys. In contrast, for bcc-Fe(Sc) crystals at 150 °C and 200 °C, precipitation of α-Sc can decrease the free energy of bcc-Fe(Sc) crystals result in more stable supersaturated solid solution (SSSS). In fact, the equilibrium solubility of Sc in bcc-Fe crystal is smaller than 0.7% [146]. Thus, Sc atoms would like to diffuse out of the lattices of the bcc-Fe(Sc) nanocrystallites (see Fig. 3-12 and Fig. 3-13b) resulting in formation of

more stable bcc-Fe(Sc) nanocrystallites. These Sc atoms semi-coherently precipitated on the planes of the bcc-Fe(Sc) nanocrystallites to form the α-Sc nanocrystallites [137] (See Fig. 3-10b, {200} planes of bcc-Fe(Sc) crystal may be the habit planes). The metastable α-Sc nanocrystallites might diffuse to the Sc-lacking interfaces at 250 °C due to the solute segregation effect, then nanocrystalline bcc-Fe(Sc) with Sc-enriched interfaces could be formed.

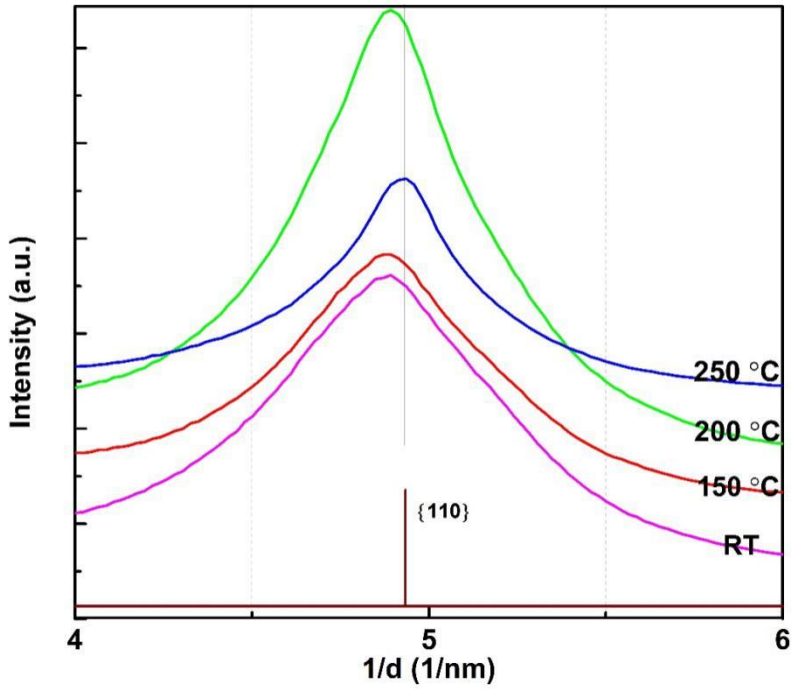

Figure 3-12. First peaks of the ED density profiles. The first peak of the ED density profile shifts towards higher angle, which suggests that some Sc atoms diffused out of the lattices of the bcc-Fe(Sc) nanocrystallites.

The Mössbauer spectra of the $Fe_{90}Sc_{10}$ NG pellet, which was annealed in an UHV tube-furnace are shown in Fig. 3-13a. The spectra of the as-prepared $Fe_{90}Sc_{10}$ NG pellet (Fig. 3-13a-RT) could be fitted with three components [7, 84], corresponding to the cores with the same structure as the corresponding melt-spun ribbons (green curve), interfaces with enhanced free volume (blue curve) and a small amount of bcc-Fe nanocrystallites (red curve). The areas under the three curves represent the volume fraction of these components.

After annealing at 150 °C for 2 hours, it was found that the volume fraction of the cores decreased and simultaneously the content of the bcc-Fe nanocrystallites increased (Fig. 3-13a-150 °C). The XRD analysis (Fig. 3-13b-150 °C) confirms the increased content of bcc-Fe nanocrystallites. No α-Sc nanocrystallites were detected by X-ray diffraction, which may be due to their small size and their small volume fraction. During annealing, the volume fraction of the interfaces was noted to increase, which is indicated by the increasing area under the blue curve.

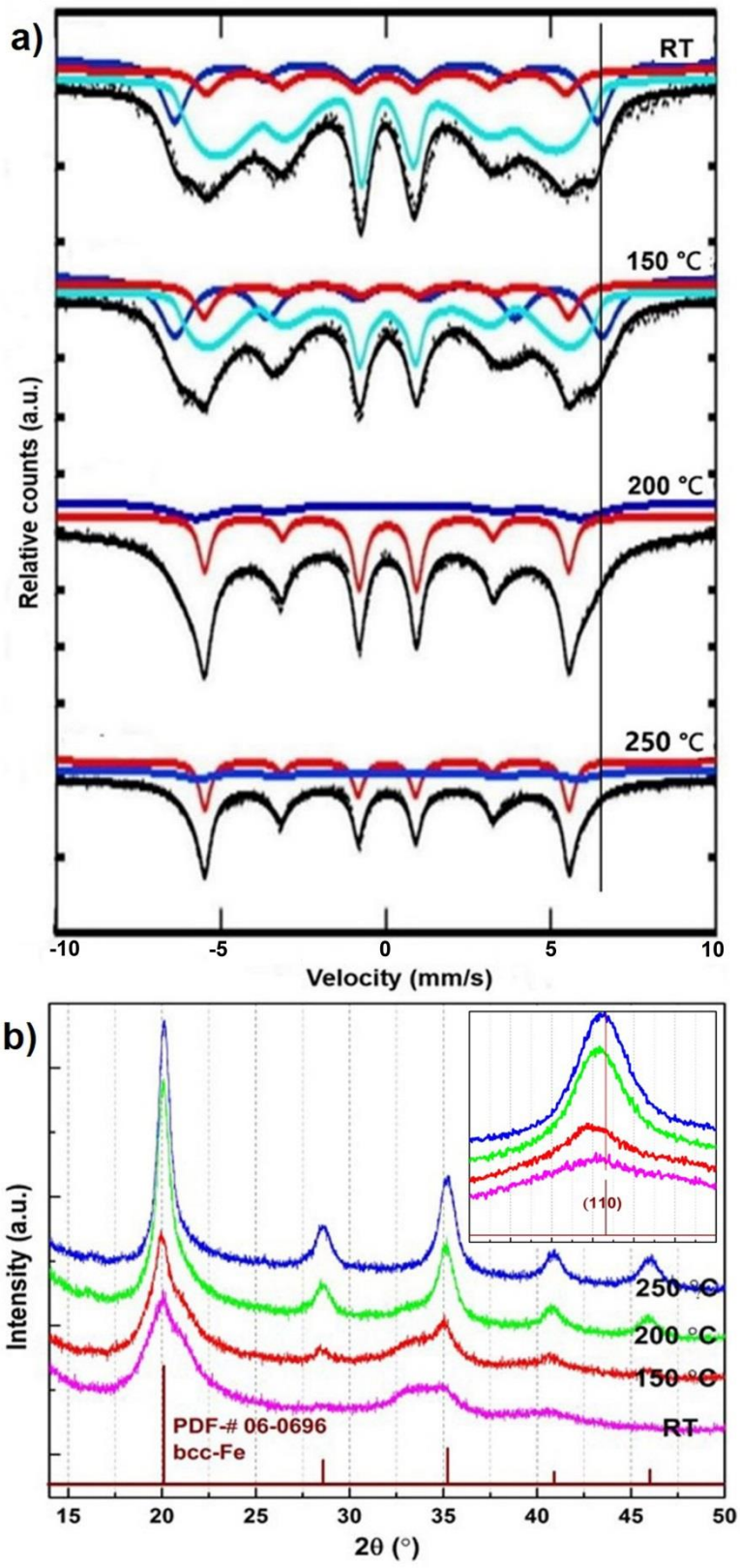

Figure 3-13. Mössbauer spectra and XRD patterns of $Fe_{90}Sc_{10}$ NG after *ex situ* annealing. (a) Low temperature Mössbauer spectra. (b) XRD patterns corresponding to the Mössbauer spectra. The original Mössbauer spectra were fitted with different curves. The red curves represent the bcc-Fe, the blue curve represent interfacial regions, while the green curves represent the cores.

During further annealing of the specimen, the area of the blue curve decreased (Fig. 3-13a-250 °C) which indicates that the volume fraction of the interfaces decreases. The same is indicated in the STEM image (Fig. 3-9a-250 °C), showing the "inter-grain" distance to become narrower. After annealing at 250 °C, the first peak of the XRD pattern shifts towards higher angle (see the insert in Fig. 3-13b), which suggests that some Sc atoms diffuse out of the lattices of bcc-Fe(Sc) nanocrystallites (cores) and segregate to the interfaces.

In general, the *in situ* and *ex situ* annealing specimens show similar crystallization process, i.e., $Fe_{90}Sc_{10}$ NGs crystallize into nanocrystalline bcc-Fe(Sc). These nanocrystalline bcc-Fe(Sc) can maintain their nanostructure and solubility for a long time after annealing below the critical temperature [147, 148]. One stability mechanism of these nanocrystalline bcc-Fe(Sc) may be due to their grain boundary energy, which was much reduced as a result of the solute segregation [92, 149].

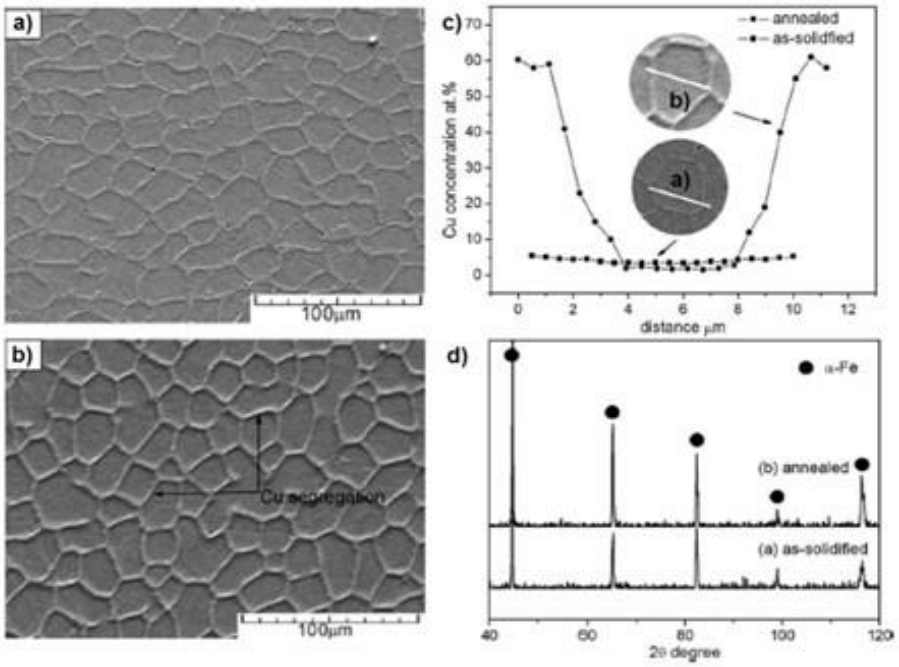

Figure 3-14. SEM images of the surface of the as-solidified $Fe_{96}Cu_4$ immiscible alloy (a), and SEM of $Fe_{96}Cu_4$ immiscible alloy after annealing at 800 °C for 60 minutes (b). Concentration profiles (c) and XRD patterns (d) of the as-prepared and as-solidified $Fe_{96}Cu_4$ immiscible alloy. [151]

Although the interfaces of these supersaturated bcc-Fe(Sc) were enriched with Sc, they might be hard to be identified from the XRD or ED patterns [150, 151]. A similar phenomenon has been observed in a $Fe_{96}Cu_4$ immiscible alloy, which was prepared using highly undercooled solidification (Fig. 3-14a) [151]. After annealing at 800 °C for 60 minutes, the grain boundaries of annealed $Fe_{96}Cu_4$ alloy are enriched with Cu (Figs. 3-14b and 3-14c), while only the single phase of α-Fe can be observed in the XRD pattern (Fig. 3-14d).

By combining the results reported so far, the structural model shown in Fig. 3-15 for the crystallization process of $Fe_{90}Sc_{10}$ NG was obtained. Specifically, Fig. 3-15a represents a part of the as-prepared $Fe_{90}Sc_{10}$ NG, which consists of cores (dark-blue spheres), interfaces (light-blue background) and some primary bcc-Fe(Sc)

nanocrystallites (grey sphere). The Sc concentration of the interfaces is lower than within the cores [127]. After annealing at 150 °C (Fig. 3-15b), the fraction of the interfaces increases, and some small metastable α-Sc nanocrystallites (red slices at the boundaries of grey spheres) are precipitated from the bcc-Fe(Sc) nanocrystallites [137]. Annealing at 200 °C (Fig. 3-15c) causes all the glassy cores within the $Fe_{90}Sc_{10}$ NG to crystallize into crystalline cores (bcc-Fe(Sc) nanocrystallites). The light-grey background represents the interfaces with enhanced atomic density. Increasing the annealing temperature to 250 °C (Fig. 3-15d), causes the metastable α-Sc nanocrystallites to dissolve and the volume fraction of the interfaces is reduced.

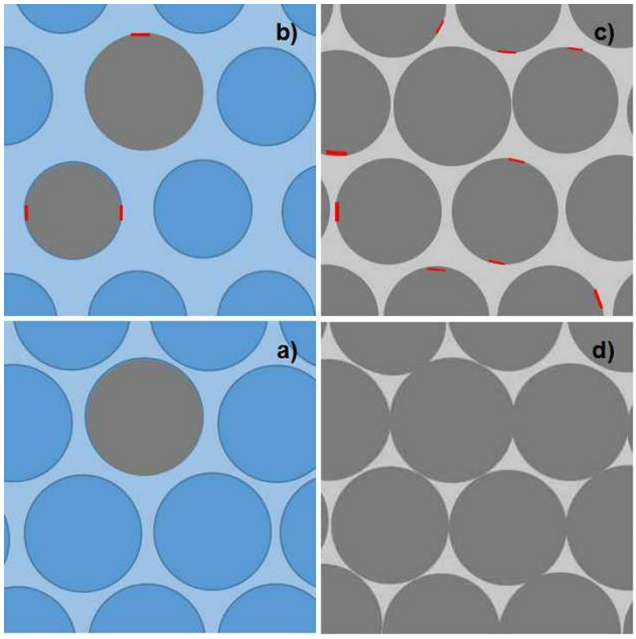

Figure 3-15. Schematic drawing of the structural evolution of $Fe_{90}Sc_{10}$ NG during low temperature annealing. (a) A part of as-prepared $Fe_{90}Sc_{10}$ NG, (b) after annealing at 150 °C for some time, (c) after annealing at 200 °C for some time, (d) after annealing at 250 °C for some time. Dark-blue spheres represent the glassy cores within the $Fe_{90}Sc_{10}$ NG, light-blue background represents the interfaces within the $Fe_{90}Sc_{10}$ NG. Dark-grey spheres represent the bcc-Fe(Sc) nanocrystallites (crystalline cores), light-grey background represents the interfaces within the nanocrystalline bcc-Fe(Sc). The red slices at boundaries of dark-grey spheres represent the metastable α-Sc nanocrystallites.

Figure 3-16a shows the radial distribution functions (RDFs) of the $Fe_{90}Sc_{10}$ NG calculated from the ED patterns using the method described in ref. [152]. Figure 3-16b displays the computer simulated RDFs of liquid Fe during cooling [153]. The similarity of both curves suggests that the structure of the as-prepared $Fe_{90}Sc_{10}$ NG resembles the structure of liquid Fe at 1250 K. This result agrees with the observations of Ghafari et al. [154]. They concluded that $Fe_{90}Sc_{10}$ melt-spun ribbons contain a high density of distorted bcc-Fe (bcc-Fe like) clusters on the basis of the similarity of RDFs of the $Fe_{90}Sc_{10}$ melt-spun ribbons and bcc-Fe crystals. Hirata et al. [155] deduced plausible structure models for Fe-based MQMG using ED intensity analysis with the help of reverse Monte Carlo simulation. In fact, they also proposed that bcc-Fe like clusters are the dominant feature of the SRO of Fe-based MQMG, and the ratio of bcc-Fe like clusters increases with increasing the Fe concentration.

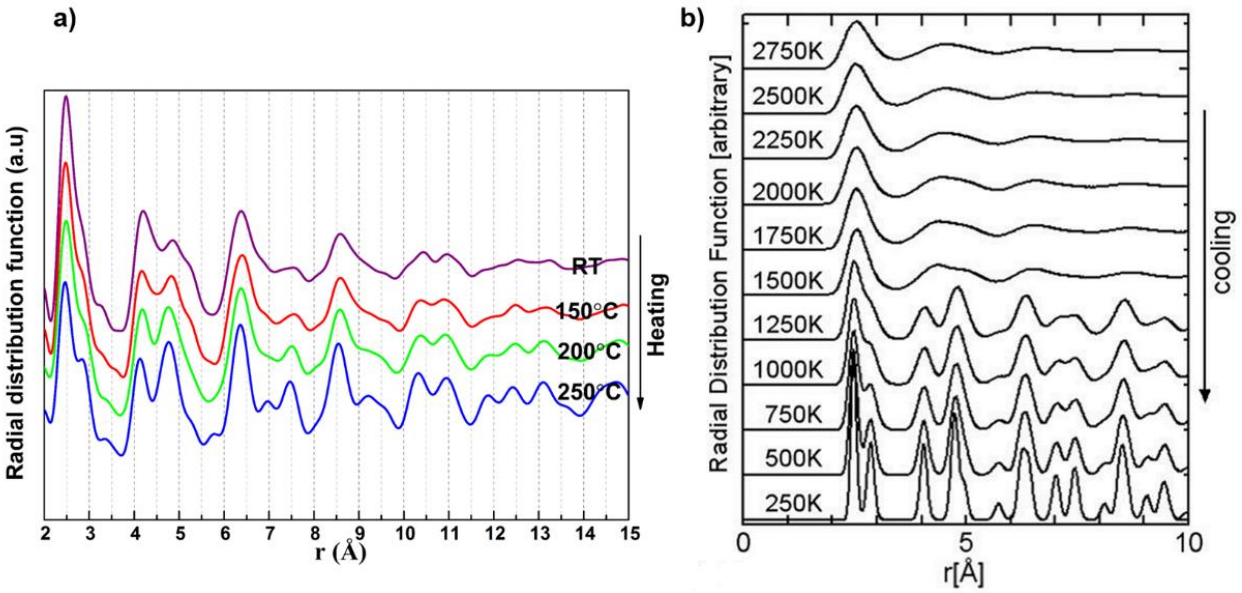

Figure 3-16. RDFs for the structural evolution of $Fe_{90}Sc_{10}$ NG during *in situ* annealing (a), and computers simulated RDFs for the structural evolution of liquid Fe during cooling (b) [153].

The similarity between the RDFs of NG during the heating process and RDFs of liquid Fe during the cooling process is also suggested by the following observation. As shown in Fig. 3-16b, with decreasing temperature, the shoulder of the first peak of the RDF at 1250 K gradually separates into two individual peaks. The newly formed peak corresponds to the second coordination sphere of the ordered bcc-Fe structure. In other words, the separation of the shoulder indicates an increasingly defined structure of bcc-Fe like clusters ultimately corresponding to the structure of an ordered bcc-Fe crystal. According to Shibuta [153] and Pan [156], the enlargement of the coordination number is a typical and necessary route from bcc-Fe like clusters to long-range ordered bcc-Fe crystal. For the $Fe_{90}Sc_{10}$ NG, the separation of the shoulder can also be observed. However, the shoulder does not separate fully, which may be due to a superposition of distances corresponding to Fe-Fe and Fe-Sc pairs [8].

It has been reported that low temperature crystallization of Fe-based MQMG is a polymorphous crystallization process by growing of clusters with critical size [147, 148, 157, 158]. These ordered clusters are formed during the quenching process and can serve as pre-existing nuclei that grow into crystallites by rearranging the atoms in short-range [159-162]. Thus, the structure of these crystallites are close to the structure of the ordered clusters. For example, after annealing at low temperature for a long time, $Fe_{80}P_{13}C_7$ and $Fe_{78}Si_{10}B_{12}$ MQMG can also be crystallized into the nanocrystalline bcc-Fe SSSS [147].

Accordingly, all of these results seem to suggest that the $Fe_{90}Sc_{10}$ NG mainly consists of bcc-Fe like clusters , and the low temperature crystallization processes of the $Fe_{90}Sc_{10}$ NG is initiated by rearranging the atoms of the bcc-Fe like clusters to form bcc-Fe (Sc) SSSS.

According to the atomic simulation and experimental results [8, 10, 12, 133, 163], the clusters within the interfaces of $Fe_{90}Sc_{10}$ NG may be loosely packed with lower CNs (CN<10). On the contrary, the SRO within the cores of $Fe_{90}Sc_{10}$ NG are closely packed with higher CNs (CN>10). As the CN of the clusters within interior cores of $Fe_{90}Sc_{10}$ NG is identical to the CN of the bcc-Fe like clusters within $Fe_{90}Sc_{10}$ melt-spun ribbons [8], and $Fe_{90}Sc_{10}$ melt-spun ribbons are mainly packed by bcc-Fe like clusters [154], it is reasonable for us to conclude that the cores of $Fe_{90}Sc_{10}$ NG are mainly packed of the bcc-Fe like clusters.

As described above, the low temperature crystallization of as-prepared $Fe_{90}Sc_{10}$ NG is proceeded by growing of quenched-in bcc-Fe like clusters into bcc-Fe(Sc) nanocrystallites. Since the atoms within the interfaces are less ordered, they need to undergo long-range diffusion to form ordered bcc-Fe [159]. Accordingly, the structural stability of interfaces is closely related to the diffusivity of the atoms.

At the beginning of the low temperature annealing, since the accumulated free volume can delocalize to spread out over the interfaces [6, 9, 10, 164, 165], the increase of the volume fraction of interfaces can be observed [6]. However, as the accumulated free volume is spread out during annealing, the diffusivity of atoms within interfaces may be not facilitated that much by the spread-out free volume [166]. In addition, as annealing continues, the average inter-atomic distances of the interfaces become smaller, which means the average potential energy of the interfaces become lower. Consequently, the diffusivity of the atoms become slower. Moreover, the Sc concentration of the cores is higher than that of the interfaces, and the enthalpy of mixing for Fe and Sc is negative [127].Therefore, due to the "solute drag" effect [92], the atoms within the cores are not prone to undergo diffusion to enlarge their inter-atomic distances.

Another factor for stabilizing the interfaces is attributed to their electronic structure. By using MS and magnetic Compton scattering, the high degree of sp hybridization of Fe atoms in the interfaces was confirmed [84]. The itinerant sp electrons definitely enhance the bond energy of Fe-Fe pairs and decrease the free energy of the interfaces. Thus, the reduced free energy slows down the diffusion of Fe atoms and enhances the structural stability of interfaces against the crystallization.

In conclusion, as indicated in Fig. 3-17, due to their special atomic and electronic structure, the thermal activation energy (ΔE) is not high enough for the interfaces to surmount the energy barrier (ΔE_1) to crystallize, thus the interfaces can keep stable at 150 °C for 2 hours without crystallization or spreading out the free volume over the entire sample. In contrast, the bcc-Fe like clusters within the cores just need little energy (ΔE_2) to arrange the atoms in short-range [167], i.e., $\Delta E > \Delta E_2$, thus the crystallization can be initiated first in the cores even though the interfaces have higher free energy. A similar phenomenon for magnetron-sputtered Au-based NG has been reported by Wang et al. [66], who used a high resolution transmission electron microscope to check the annealed sample and found that the nanocrystallites initiated first in the cores.

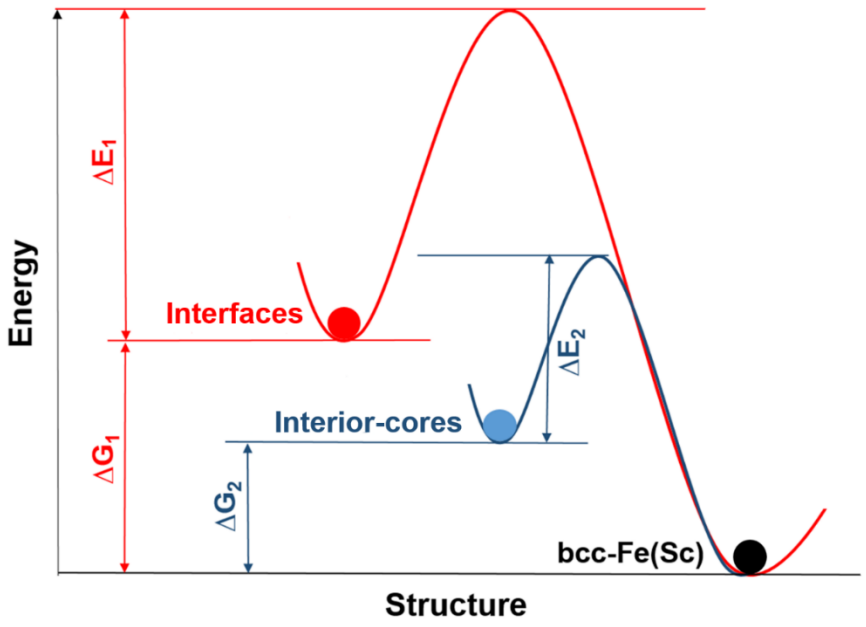

Figure 3-17. Schematic drawing of the free energy of the interfaces and the cores; energy barrier (ΔE_1) between the interfaces and the bcc-Fe (Sc) nanocrystallites; energy barrier (ΔE_2) between the cores and the bcc-Fe(Sc) nanocrystallites. Interfaces have higher free energy than the cores, which means that the driving force for the crystallization of the interfaces (ΔG_1) is higher than that of the cores (ΔG_2). However, the energy barrier for the crystallization of the interfaces (ΔE_1) is higher than that of the interfaces (ΔE_2), thus the nanocrystallites initiated first in the cores.

Finally, it should be pointed out that the above discussion is based on the "pure amorphous" NG without taking into account the effect of the primary bcc-Fe nanocrystallites. The STEM images reveal that the "glassy nanograins" crystallize individually into "crystalline nanograins" without changes in their size, and the number of "grain boundaries" also does not change. This means that the growth rate of primary bcc-Fe nanocrystallites is slow below 250 °C. The primary bcc-Fe nanocrystallites, which are either formed during quenching or high pressure consolidation by a primary crystallization mechanism, are precipitated from the amorphous matrix but with smaller solute concentration than the glass matrix [168]. In order to grow, the activation energy is needed to diffuse and redistribute the solute atoms near the primary nanocrystallites. Accordingly, at low annealing temperature, the growth rate of these primary nanocrystallites is limited. Therefore, for the sake of simplicity, the above analysis without considering too much of the primary bcc-Fe nanocrystallites is acceptable.

4 Conclusions and Outlook

An enrichment of Fe at the surfaces of $Fe_{90}Sc_{10}$ GNp was observed. This surface segregation was found to result in a chemically heterogeneous structure of $Fe_{90}Sc_{10}$ NG. The results of a theoretical study using a monolayer model of the surface segregation of Fe-Sc GNp were found to agree with the experimentally observed segregation effects.

Based on the lower electron density and the surface segregation behavior of the primary $Fe_{90}Sc_{10}$ GNp, a lower packing density of the outer shells of the GNp is detected. Then, according to the chemical composition and the atomic packing density variation of the primary GNp, a model for the atomic structure of $Fe_{90}Sc_{10}$ GNp is proposed. Some fraction of the free volume within the shells as well as the SRO may then be transferred from the primary $Fe_{90}Sc_{10}$ GNp by consolidation into the interfaces of the $Fe_{90}Sc_{10}$ NG. The interfaces within the $Fe_{90}Sc_{10}$ NG are loosely packed but with higher Fe concentration than the cores within the $Fe_{90}Sc_{10}$ NG.

Owing to their special atomic and electronic structure, the interfaces of $Fe_{90}Sc_{10}$ NG can remain stable even during annealing at 150 °C for 2 hours. In addition, it seems that the interfaces are more stable than the cores in that the crystallization starts within the cores to lead to the formation of nanocrystallites.

Although some fundamental work was carried out in this thesis project to gain a better understanding of NG, as a new topic, more questions about NG remain to be answered. In the near future, the research of NG will be carried out as follows.

By adjusting the diameter of the primary GNp, the volume fraction of the interfaces of $Fe_{90}Sc_{10}$ NG can be varied. As it has been shown that the interfacial component in NG exhibit rather different magnetic properties, i.e., ferromagnetic behavior at room temperature in NG, while conventional glass of same composition is paramagnetic, the variation of the interfacial content can be used to tailor the magnetic properties in a way not possible by any other means. The physical relationships between the diameter of the GNp, volume fractions of the interfaces and magnetic properties (such as the magnetization) of the NG should be elucidated, and these relationships will provide some insight into the tailoring of the properties of the NG.

At low temperature, the electronic contribution to the specific heat could be distinguished from the phonon contribution to the specific heat since they are comparable. Accordingly, low temperature heat capacity measurements of NG will be utilized as a powerful technique to characterize the atomic and electronic structure of solid materials.

Finally, the most significant problem that needs to be urgently addressed is to develop a simpler method than the IGC method to prepare high quality NG specimen. This may be the key to the door of a NG world.

Curriculum Vitae

Name:	Chaomin WANG
Date and Place of Birth:	21.09.1986, Anhui, China
Nationality:	Chinese

Education

09.2011-present	*Doctoral studies* in Materials Science Joint Research Laboratory for Nanomaterials, Technische Universität Darmstadt & Institute for nanotechnology, Karlsruhe Institute of Technology, Germany
11.2015-04.2016	Visiting student Herbert Gleiter Institute of Nanoscience Nanjing University of Science and Technology, China
09.2009-07.2011	*M. Sc.* in Inorganic Chemistry School of Chemistry and Chemical Technology Sun Yat-Sen University, China
09.2005-07.2009	*B. Tech.* in Applied Chemistry School of Petroleum and Chemical Technology Liaoning University of Petroleum and Chemical Technology, China

Publications Based On the Present Dissertation

[1] Chaomin Wang*, Di Wang, Xiaoke Mu, Sunkulp Goel, Tao Feng, Yulia Ivanisenko, Horst Hahn, and H. Gleiter, "Surface segregation of primary glassy nanoparticles of $Fe_{90}Sc_{10}$ nanoglass," *Materials Letters*, vol. 181, pp. 248-252, 2016.

[2] Chaomin Wang*, Xiaoai Guo, Yulia Ivanisenko, Sunkulp Goel, Hermann Nirschl, Herbert Gleiter*, and Horst Hahn*, "Atomic structure of $Fe_{90}Sc_{10}$ glassy nanoparticles and nanoglasses," *Scripta Materialia*, vol. 139, pp. 9-12, 2017.

[3] Chaomin Wang*, Tao Feng, Di Wang, Xiaoke Mu, Mohammad Ghafari, Ralf Witte, Aaron Kobler, Christian Kübel, Yulia Ivanisenko, Herbert Gleiter*, and Horst Hahn*, "Low temperature structural stability of $Fe_{90}Sc_{10}$ nanoglasses," Submitted to *Materials Research Letters*.

References

[1] H. Gleiter, "Our thoughts are ours, their ends none of our own: Are there ways to synthesize materials beyond the limitations of today? ," *Acta Materialia*, vol. 56, pp. 5875-5893, 2008.

[2] H. Gleiter, "Nanoglasses: a new kind of non-crystalline materials," *Beilstein Journal of Nanotechnology*, vol. 4, pp. 517-533, 2013.

[3] H. Gleiter, "The way from today's materials to new kinds of amorphous solids: Nano-glasses," *Journal of the Chemical Society*, vol. 80, pp. 55-75, 2014.

[4] H. Gleiter, T. Schimmel, and H. Hahn, "Nanostructured solids - From nano-glasses to quantum transistors," *Nano Today*, vol. 9, pp. 17-68, 2014.

[5] H. Gleiter, "Nanoglasses: A new kind of non-crystalline material and the way to an age of new technologies?," *Small*, vol. 12, pp. 2225-2233, 2016.

[6] J. X. Fang, U. Vainio, W. Puff, R. Wurschum, X. L. Wang, D. Wang, M. Ghafari, F. Jiang, J. Sun, H. Hahn, and H. Gleiter, "Atomic structure and structural stability of $Sc_{75}Fe_{25}$ nanoglasses," *Nano Letters*, vol. 12, pp. 458-463, 2012.

[7] R. Witte, T. Feng, J. X. Fang, A. Fischer, M. Ghafari, R. Kruk, R. A. Brand, D. Wang, H. Hahn, and H. Gleiter, "Evidence for enhanced ferromagnetism in an iron-based nanoglass," *Applied Physics Letters*, vol. 103, p. 073106, 2013.

[8] M. Ghafari, S. Kohara, H. Hahn, H. Gleiter, T. Feng, R. Witte, and S. Kamali, "Structural investigations of interfaces in $Fe_{90}Sc_{10}$ nanoglasses using high-energy x-ray diffraction," *Applied Physics Letters*, vol. 100, p. 243104, 2012.

[9] D. Sopu, K. Albe, Y. Ritter, and H. Gleiter, "From nanoglasses to bulk massive glasses," *Applied Physics Letters*, vol. 94, p. 191911, 2009.

[10] Y. Ritter, D. Şopu, H. Gleiter, and K. Albe, "Structure, stability and mechanical properties of internal interfaces in $Cu_{64}Zr_{36}$ nanoglasses studied by MD simulations," *Acta Materialia*, vol. 59, pp. 6588-6593, 2011.

[11] D. Danilov, H. Hahn, H. Gleiter, and W. Wenzel, "Mechanisms of nanoglass ultrastability," *Acs Nano*, vol. 10, 3241-3247, 2016.

[12] O. Adjaoud and K. Albe, "Interfaces and interphases in nanoglasses: Surface segregation effects and their implications on structural properties," *Acta Materialia*, vol. 113, pp. 284-292, 2016.

[13] M. K. Miller and P. K. Liaw, "Bulk metallic glasses," *Materials Science & Engineering R-Reports*, vol. 11, pp. 529-540, 2007.

[14] A. R. Yavari, "Bulk metallic glasses," *Materials Science & Engineering R Reports*, vol. 44, pp. 45-89, 2013.

[15] P. G. Debenedetti and F. H. Stillinger, "Supercooled liquids and the glass transition," *Nature,* vol. 410, p. 259-267, 2001.

[16] A. R. Yavari, J. J. Lewandowski, and J. Eckert, "Mechanical properties of bulk metallic glasses," *MRS Bulletin,* vol. 32, pp. 635-638, 2007.

[17] M. M. Trexler and N. N. Thadhani, "Mechanical properties of bulk metallic glasses," *Progress in Materials Science,* vol. 55, pp. 759-839, 2010.

[18] J. J. Lewandowski, W. H. Wang, and A. L. Greer, "Intrinsic plasticity or brittleness of metallic glasses," *Philosophical Magazine Letters,* vol. 85, pp. 77-87, 2005.

[19] L. Y. Chen, A. D. Setyawan, H. Kato, A. Inoue, G. Q. Zhang, J. Saida, X. D. Wang, Q. P. Cao, and J. Z. Jiang, "Free volume induced enhancement of plasticity in a monolithic bulk metallic glass at room temperature," *Scripta Materialia,* vol. 59, pp. 75-78, 2008.

[20] L. Y. Chen, Z. D. Fu, G. Q. Zhang, X. P. Hao, Q. K. Jiang, X. D. Wang, Q. P. Cao, H. Franz, Y. G. Liu, H. S. Xie, S. L. Zhang, B. Y. Wang, Y. W. Zeng, and J. Z. Jiang, "New class of plastic bulk metallic glass," *Physical Review Letters,* vol. 100, p. 075501, 2008.

[21] J. Shen, Y. J. Huang, and J. F. Sun, "Plasticity of a TiCu-based bulk metallic glass: effect of cooling rate," *Journal of Materials Research,* vol. 22, pp. 3067-3074, 2007.

[22] M. L. Falk and J. S. Langer, "Dynamics of viscoplastic deformation in amorphous solids," *Physical Review E,* vol. 57, pp. 7192-7205, 1998.

[23] X. D. Wang, Q. P. Cao, J. Z. Jiang, H. Franz, J. Schroers, R. Z. Valiev, Y. Ivanisenko, H. Gleiter, and H. J. Fecht, "Atomic-level structural modifications induced by severe plastic shear deformation in bulk metallic glasses," *Scripta Materialia,* vol. 64, pp. 81-84, 2011.

[24] J. W. Liu, Q. P. Cao, L. Y. Chen, X. D. Wang, and J. Z. Jiang, "Shear band evolution and hardness change in cold-rolled bulk metallic glasses," *Acta Materialia,* vol. 58, pp. 4827-4840, 2010.

[25] J. Jing, A. Kramer, R. Birringer, H. Gleiter, and U. Gonser, "Modified atomic structure in a Pd-Fe-Si nanoglass - a Mössbauer study," *Journal of Non-Crystalline Solids,* vol. 113, pp. 167-170, 1989.

[26] D. Sopu, Y. Ritter, H. Gleiter, and K. Albe, "Deformation behavior of bulk and nanostructured metallic glasses studied via molecular dynamics simulations," *Physical Review B,* vol. 83, 100202, 2011.

[27] K. Albe, Y. Ritter, and D. Sopu, "Enhancing the plasticity of metallic glasses: shear band formation, nanocomposites and nanoglasses investigated by molecular dynamics simulations," *Mechanics of Materials,* vol. 67, pp. 94-103, 2013.

[28] M. H. Cohen and D. Turnbull, "Molecular transport in liquids and glasses," *The Journal of Chemical Physics,* vol. 31, pp. 1164-1169, 1959.

[29] D. Turnbull and M. H. Cohen, "Free volume model of the amorphous phase: glass transition," *Journal of Chemical Physics,* vol. 34, pp. 120-125, 1961.

[30] D. Turnbull and M. H. Cohen, "On the free volume model of the liquid-glass transition," *Journal of Chemical Physics,* vol. 52, pp. 3038-3041, 1970.

[31] M. H. Cohen and G. S. Grest, "Liquid-glass transition, a free volume approach," *Physical Review B,* vol. 26, pp. 1077-1098, 1979.

[32] S. R. Elliott, "Medium-range structural order in covalent amorphous solids," *Nature,* vol. 354, pp. 445-452, 1991.

[33] C. Suryanarayana and A. Inoue, "Bulk metallic glasses," : CRS Press, pp. 218-219, 2010.

[34] D. B. Miracle, "A structural model for metallic glasses," *Nature Materials,* vol. 3, pp. 697-702, 2004.

[35] D. B. Miracle, "The efficient cluster packing model – an atomic structural model for metallic glasses," *Acta Materialia,* vol. 54, pp. 4317-4336, 2006.

[36] D. B. Miracle, E. A. Lord, and S. Ranganathan, "Candidate atomic cluster configurations in metallic glass structures," *Materials Transactions,* vol. 47, pp. 1737-1742, 2006.

[37] H. W. Sheng, W. K. Luo, F. M. Alamgir, J. M. Bai, and E. Ma, "Atomic packing and short-to-medium-range order in metallic glasses," *Nature,* vol. 439, pp. 419-425, 2006.

[38] A. Hirata, P. Guan, T. Fujita, Y. Hirotsu, A. Inoue, A. R. Yavari, T. Sakurai, and M. Chen, "Direct observation of local atomic order in a metallic glass," *Nature Materials,* vol. 10, pp. 28-33, 2011.

[39] A. Hirata, L. J. Kang, T. Fujita, B. Klumov, K. Matsue, M. Kotani, A. R. Yavari, and M. W. Chen, "Geometric frustration of icosahedron in metallic glasses," *Science,* vol. 341, pp. 376-379, 2013.

[40] V. V. Hoang and D. Ganguli, "Amorphous nanoparticles - experiments and computer simulations," *Physics Reports,* vol. 518, pp. 81-140, 2012.

[41] C. C. Koch, "Nanostructured materials: processing, properties and applications, 2nd Edition," Noyes Publications : William Andrew Publishing, pp. 47-90, 2002.

[42] M. Müller, "*Magnetische und strukturelle Charakterisierung von amorphen Eisen-Scandium-Legierungen*". *PhD Dissertation*, TU Darmstadt, p. 8, (2003).

[43] O. Franke, D. Leisen, H. Gleiter, and H. Hahn, "Thermal and plastic behavior of nanoglasses," *Journal of Materials Research,* vol. 29, pp. 1210-1216, 2014.

[44] X. L. Wang, F. Jiang, H. Hahn, J. Li, H. Gleiter, J. Sun, and J. X. Fang, "Plasticity of a scandium-based nanoglass," *Scripta Materialia,* vol. 98, pp. 40-43, 2015.

[45] S. Adibi, Z. D. Sha, P. S. Branicio, S. P. Joshi, Z. S. Liu, and Y. W. Zhang, "A transition from localized shear banding to homogeneous superplastic flow in nanoglass," *Applied Physics Letters,* vol. 103, p. 211905, 2013.

[46] S. Adibi, P. S. Branicio, Y. W. Zhang, and S. P. Joshi, "Composition and grain size effects on the structural and mechanical properties of CuZr nanoglasses," *Journal of Applied Physics,* vol. 116, p. 043522, 2014.

[47] Z. D. Sha, L. C. He, Q. X. Pei, Z. S. Liu, Y. W. Zhang, and T. J. Wang, "The mechanical properties of a nanoglass/metallic glass/nanoglass sandwich structure," *Scripta Materialia,* vol. 83, pp. 37-40, 2014.

[48] Z. D. Sha, L. C. He, Q. X. Pei, H. Pan, Z. S. Liu, Y. W. Zhang, and T. J. Wang, "On the notch sensitivity of CuZr nanoglass," *Journal of Applied Physics,* vol. 115, p.163507, 2014.

[49] S. Adibi, P. S. Branicio, and S. P. Joshi, "Suppression of shear banding and transition to necking and homogeneous flow in nanoglass nanopillars," *Scientific Reports*, vol. 5, p. 15611, 2015.

[50] Z. D. Sha, P. S. Branicio, Q. X. Pei, Z. S. Liu, H. P. Lee, T. E. Tay, and T. J. Wang, "Strong and superplastic nanoglass," *Nanoscale*, vol. 7, p. 17404-17409, 2015.

[51] D. Şopu and K. Albe, "Influence of grain size and composition, topology and excess free volume on the deformation behavior of Cu–Zr nanoglasses," *Beilstein Journal of Nanotechnology*, vol. 6, pp. 537–545, 2015.

[52] X. D. Wang, F. Jiang, H. Hahn, J. Li, H. Gleiter, J. Sun, and J. X. Fang, "Sample size effects on strength and deformation mechanism of $Sc_{75}Fe_{25}$ nanoglass and metallic glass," *Scripta Materialia*, vol. 116, pp. 95-99, 2016.

[53] N. Chen, R. Frank, N. Asao, D. V. Louzguine-Luzgin, P. Sharma, J. Q. Wang, G. Q. Xie, Y. Ishikawa, N. Hatakeyama, and Y. C. Lin, "Formation and properties of Au-based nanograined metallic glasses," *Acta Materialia*, vol. 59, pp. 6433-6440, 2011.

[54] Z. Śniadecki, D. Wang, Y. Ivanisenko, V. S. K. Chakravadhanula, C. Kübel, H. Hahn, and H. Gleiter, "Nanoscale morphology of Ni $_{50}Ti_{45}Cu_5$ nanoglass," *Materials Characterization*, vol. 113, pp. 26-33, 2016.

[55] N. Chen, D. V. Louzguine-Luzgin, and K. F. Yao, "A new class of non-crystalline materials: Nanogranular metallic glasses," *Journal of Alloys & Compounds*, vol. 707, pp. 371-378, 2017.

[56] Y. H. Liu, T. Fujita, A. Hirata, S. Li, H. W. Liu, W. Zhang, A. Inoue, and M. W. Chen, "Deposition of multicomponent metallic glass films by single-target magnetron sputtering," *Intermetallics*, vol. 21, pp. 105-114, 2012.

[57] S. V. Ketov, R. Joksimovic, G. Xie, A. Trifonov, K. Kurihara, and D. V. Louzguine-Luzgin, "Formation of nanostructured metallic glass thin films upon sputtering," *Heliyon*, vol. 3, p. e00228, 2017.

[58] N. Chen, D. V. Louzguine-Luzgin, G. Q. Xie, P. Sharma, J. H. Perepezko, M. Esashi, A. R. Yavari, and A. Inoue, "Structural investigation and mechanical properties of a representative of a new class of materials: nanograined metallic glasses," *Nanotechnology*, vol. 24, p. 045610, 2013.

[59] D. Zhao, C. L. Chen, K. F. Yao, X. T. Shi, Z. C. Wang, H. Hahn, H. Gleiter, and N. Chen, "Designing biocompatible Ti-based amorphous thin films with no toxic element," *Journal of Alloys & Compounds*, vol. 707, pp. 142-147, 2017.

[60] N. Chen, X. T. Shi, R. Witte, K. S. Nakayama, K. Ohmura, H. K. Wu, A. Takeuchi, H. Hahn, M. Esashi, and H. Gleiter, A. Inouea and D. V. Louzguinea-Luzgin "A novel Ti-based nanoglass composite with submicron–nanometer-sized hierarchical structures to modulate osteoblast behaviors," *Journal of Materials Chemistry B*, vol. 1, pp. 2568-2574, 2013.

[61] S. V. Ketov, X. T. Shi, G. Q. Xie, R. Kumashiro, A. Y. Churyumov, A. I. Bazlov, N. Chen, Y. Ishikawa, N. Asao, and H. K. Wu, D. V. Louzguinea-Luzgin "Nanostructured Zr-Pd metallic glass thin film for biochemical applications," *Scientific Reports*, vol. 5, p. 7799, 2015.

[62] L. Lu, M. L. Sui, and K. Lu, "Superplastic extensibility of nanocrystalline copper at room temperature," *Science,* vol. 287, p. 1463-1466, 2000.

[63] C. Guo, Y. Fang, B. Wu, S. Lan, G. Peng, X. Wang, H. Hahn, H. Gleiter, and T. Feng, "Ni-P nanoglass prepared by multi-phase pulsed electrodeposition," *Materials Research Letters,* vol. 5, pp. 293-299, 2016.

[64] A. Kartouzian, J. Antonowicz, T. Lünskens, A. Lagogianni, P. Heister, G. Evangelakis, and R. Felici, "Toward cluster-assembled metallic glasses," *Materials Express,* Vol. 4, pp. 228-234, 2014.

[65] A. Kartouzian and J. Antonowicz, "Metallic glasses from the bottom-up," *Metallic Glasses: Formation and Properties,* Chapter 1, 2016.

[66] J. Q. Wang, N. Chen, P. Liu, Z. Wang, D. V. Louzguine-Luzgin, M. W. Chen, and J. H. Perepezko, "The ultrastable kinetic behavior of an Au-based nanoglass," *Acta Materialia,* vol. 79, pp. 30-36, 2014.

[67] H. Shao, Y. Xu, B. Shi, C. Yu, H. Hahn, H. Gleiter, and J. G. Li, "High density of shear bands and enhanced free volume induced in $Zr_{70}Cu_{20}Ni_{10}$ metallic glass by high-energy ball milling," *Journal of Alloys & Compounds,* vol. 548, pp. 77-81, 2013.

[68] V. Y. Slesarenko, D. A. Gunderov, P. G. Ulyanov, and R. Z. Valiev, "Formation of amorphous states in $Ti_{50}Ni_{25}Cu_{25}$ alloy subjected to severe plastic deformation: Nanoglass issue," in *IOP Conference Series: Materials Science and Engineering,* vol. 5, pp. 12166-12170, 2014.

[69] R. A. Andrievski, "Metallic nano/microglasses: new approaches in nanostructured materials science," *Physics Uspekhi,* vol. 56, pp. 261-268, 2013.

[70] R. A. Andrievskii, "Nanoglasses and amorphous nanocrystalline materials: Some new approaches," *Bulletin of the Russian Academy of Sciences: Physics,* vol. 76, pp. 37-43, 2012.

[71] R. Würschum, M. Rollinger, H. Kisker, A. Raichle, B. Damson, and H. E. Schaefer, "Synthesis of nanoamorphous alloys by particle condensation and compaction," *Nanostructured Materials,* vol. 6, pp. 377-380, 1995.

[72] J. Weissmüller, R. Birringer, and H. Gleiter, "Nanostructured crystalline and amorphous solids," *Key Engineering Materials,* vol. 77-78, pp. 161-170, 1992.

[73] R. S. Averback, H. Hahn, H. J. Hofler, and J. C. Logas, "Processing and properties of nanophase amorphous metallic alloys: Ni-Ti," *Applied Physics Letters,* vol. 57, pp. 1745-1747, 1990.

[74] L. S. Kim, H. Chang, and R. S. Averback, "Nanophase processing of amorphous alloys ," *Journal of Alloys & Compounds,* vol. 194, pp. 245-249, 1993.

[75] J. Weissmüller, R. Birringer, and H. Gleiter, "Short-range disordered Si-Au alloy - evidence for a new phase?," *Physics Letters A,* vol. 145, pp. 130-136, 1990.

[76] N. Chen, D. Wang, T. Feng, R. Kruk, K. F. Yao, D. V. Louzguine-Luzgin, H. Hahn, and H. Gleiter, "A nanoglass alloying immiscible Fe and Cu at the nanoscale," *Nanoscale,* vol. 7, pp. 6607-6611, 2015.

[77] J. Weissmuller, "Reduced short-range order in amorphous silicon-gold alloys," *Journal of Non-Crystalline Solids,* vol. 142, pp. 70-80, 1992.

[78] A. Sturm and A. Wiedenmann, "Microstructure of nanostructured amorphous Si-Au alloys," *Journal De Physique Iv*, vol. 3, pp. 341-344, 1993.

[79] A. Wiedenmann, A. Sturm, and H. Wollenberger, "Small-angle neutron scattering studies of nanosized amorphous Si-Au alloys," *Materials Science and Engineering A-Structural Materials Properties Microstructure and Processing*, vol. 179, pp. 458-463, 1994.

[80] A. Sturm and A. Wiedenmann, "SANS investigation of internal interfaces in nanostructured Si-Au alloys," *Physica B Condensed Matter*, vol. 213, pp. 576-578, 1995.

[81] A. Sturm, A. Wiedenmann, and H. Wollenberger, "Nanostructured amorphous Si-Au alloys - structure and atomic correlations," *Materials Science and Engineering B-Solid State Materials for Advanced Technology*, vol. 32, pp. 295-306, 1995.

[82] A. Sturm and A. Wiedenmann, "Fractal internal interfaces in nanostructured amorphous Si-Au alloys," *Nanostructured Materials*, vol. 6, pp. 643-646, 1995.

[83] T. Campbell, R. K. Kalia, A. Nakano, F. Shimojo, K. Tsuruta, P. Vashishta, and S. Ogata, "Structural correlations and mechanical behavior in nanophase silica glasses," *Physical Review Letters*, vol. 82, pp. 4018-4021, 1999.

[84] M. Ghafari, H. Hahn, H. Gleiter, Y. Sakurai, M. Itou, and S. Kamali, "Evidence of itinerant magnetism in a metallic nanoglass," *Applied Physics Letters*, vol. 101, 243104, 2012.

[85] A. Léon, J. Rothe, H. Hahn, and H. Gleiter, "Short range order around Sc atoms in $Fe_{90}Sc_{10}$ nanoglasses using fluorescence X-ray absorption spectroscopy," *Revue De Métallurgie*, vol. 109, pp. 35-39, 2012.

[86] M. J. Osborne and D. J. Lacks, "Surface segregation in liquid mixtures with strong interspecies attraction," *Physical Review E*, vol. 70, p. 010501, 2004.

[87] S. Saw, S. Kamil, and C. Dasgupta, "Spatial modulation of the composition of a binary liquid near a repulsive wall," *Physical Review E*, vol. 91, p. 052406, 2015.

[88] P. Wynblatt and D. Chatain, "Anisotropy of segregation at grain boundaries and surfaces," *Metallurgical and Materials Transactions A-Physical Metallurgy and Materials Science*, vol. 37A, pp. 2595-2620, 2006.

[89] S. Overbury, P. Bertrand, and G. Somorjai, "Surface composition of binary systems. Prediction of surface phase diagrams of solid solutions," *Chemical reviews*, vol. 75, pp. 547-560, 1975.

[90] J. Q. Wang, N. Chen, P. Liu, Z. Wang, D. V. Louzguine-Luzgin, M. W. Chen, and J. H. Perepezko, "The ultrastable kinetic behavior of an Au-based nanoglass," *Acta Materialia*, vol. 79, pp. 30-36, 2014.

[91] J. Svoboda, F. D. Fischer, E. Gamsjäger, "Influence of solute segregation and drag on properties of migrating interfaces," *Acta Materialia*, vol. 50, pp. 967–977, 2002.

[92] J. Weissmüller, W. Krauss, T. Haubold, R. Birringer, and H. Gleiter, "Atomic structure and thermal stability of nanostructured Y-Fe alloys," *Nanostructured Materials*, vol. 1, pp. 439-447, 1992.

[93] Y. L. Guo, A. Morozov, D. Schneider, J. W. Chung, C. Zhang, M. Waldmann, N. Yao, G. Fytas, C. B. Arnold, and R. D. Priestley, "Ultrastable nanostructured polymer glasses," *Nature Materials*, vol. 11, p. 337-343, 2012.

[94] P. Krasnochtchekov, K. Albe, Y. Ashkenazy, and R. S. Averback, "Molecular dynamics study of the density scaling of inert gas condensation," *Journal of Chemical Physics*, vol. 123, p. 154314, 2005.

[95] C. G. Granqvist and R. A. Buhrman, "Ultrafine metal particles," *Journal of Applied Physics*, vol. 47, pp. 2200-2219, 1976.

[96] E. Kesälä, A. Kuronen, and K. Nordlund, "Molecular dynamics simulation of pressure dependence of cluster growth in inert gas condensation," *Physical Review B*, vol. 75, pp. 174121, 2007.

[97] A. Guinier, "X-ray diffraction in crystals, imperfect crystals, and amorphous bodies, " : W.H. Freeman, 1963.

[98] Z. L. Wang, Y. Liu, and Z. Zhang, "Handbook of nanophase and nanostructured materials，vol. 2-Characteriyation," : Tsinghua university, 2002.

[99] T. Egami and S. J. L. Billinge, "Underneath the Bragg peaks: structural analysis of complex materials, Vol. 7," : Elsevier Ltd, 2003.

[100] A. Hirata, P. Guan, T. Fujita, Y. Hirotsu, A. Inoue, A. R. Yavari, T. Sakurai, and M. Chen, "Direct observation of local atomic order in a metallic glass," *Nature Materials*, vol. 10, p. 28, 2011.

[101] P. W. Schmidt, D. Avnir, D. Levy, A. Höhr, M. Steiner, and A. Röll, "Small-angle x-ray scattering from the surfaces of reversed-phase silicas: Power-law scattering exponents of magnitudes greater than four," *Journal of Chemical Physics*, vol. 94, pp. 1474-1479, 1991.

[102] X. Guo, A. Gutsche, and H. Nirschl, "SWAXS investigations on diffuse boundary nanostructures of metallic nanoparticles synthesized by electrical discharges," *Journal of Nanoparticle Research*, vol. 15, p. 2058, 2013.

[103] P. W. Schmidt, "Small-angle scattering studies of disordered, porous and fractal systems," *Journal of Applied Crystallography*, vol. 24, pp. 414-435, 1991.

[104] W. J. Ruland, "Small-angle scattering of two phase systems: Determination and significance of systematic deviation from Porod's law," *Journal of Applied Crystallography*, vol. 4, pp. 70-73, 1971.

[105] U. Herr, J. Jing, R. Birringer, U. Gonser, and H. Gleiter, "Investigation of nanocrystalline iron materials by Mössbauer spectroscopy," *Applied Physics Letters*, vol. 50, pp. 472-474, 1987.

[106] B. Fultz, H. Kuwano, and H. Ouyang, "Average widths of grain boundaries in nanophase alloys synthesized by mechanical attrition," *Journal of Applied Physics*, vol. 77, pp. 3458-3466, 1995.

[107] D. Wang, X. K. Mu, C. M. Wang, T. Feng, A. Kobler, C. Kübel, H. Hahn, and H. Gleiter, "Understanding the complex structures in nanoglasses," *Electron Microscope Conference*, pp. 686-687, 2016.

[108] E. Guggenheim, "Statistical thermodynamics of the surface of a regular solution," *Transactions of the Faraday Society*, vol. 41, pp. 150-156, 1945.

[109] R. Defay, I. Prigogine, A. Bellemans, and D. H. Everett, "Surface tension and adsorption,": Longmans, 1966.

[110] W. Kauzmann, "The nature of the glassy state and the behavior of liquids at low temperatures," *Chemical Reviews*, vol. 43, pp. 219-256, 1948.

[111] J. C. Dyre, "Glasses: Heirs of liquid treasures," *Nature Materials,* vol. 3, pp. 749-750, 2004.

[112] P. D. Desai, "Thermodynamic properties of iron and silicon," *Journal of Physical and Chemical Reference Data,* vol. 15, pp. 967-983, 1986.

[113] O. H. Krikorian, "The vapor pressure of scandium metall," *The Journal of Physical Chemistry,* vol. 67, pp. 1586-1589, 1963.

[114] R.A. Swalin, Thermodynamics of Solids, 2nd ed., Wiley, New York, 1972.

[115] F. R. de Boer, R. Boom, W.C.M. Mattens, A.R. Miedema, A.K. Niessen, "Cohesion in metals: Transition metal alloys, " : Elsevier Science, New York, 1988.

[116] O. E. Awe and A. Onifade, "Effects of surface coordination of atoms on the surface properties of some liquid binary alloys," *Physics and Chemistry of Liquids,* vol. 50, pp. 579-595, 2012.

[117] J. D. Bernal, "Geometry of the structure of monatomic liquids," *Nature,* vol. 185, pp. 68-70, 1960.

[118] T. Hoar and D. Melford, "The surface tension of binary liquid mixtures: lead+tin and lead+indium alloys," *Transactions of the Faraday Society,* vol. 53, pp. 315-326, 1957.

[119] R. C. Tolman, "The effect of droplet size on surface tension," *Journal of Chemical Physics,* vol. 17, pp. 333-337, 1949.

[120] S. Y. Xiong, W. H. Qi, Y. J. Cheng, B. Y. Huang, M. P. Wang, and Y. J. Li, "Modeling size effects on the surface free energy of metallic nanoparticles and nanocavities," *Physical Chemistry Chemical Physics,* vol. 13, pp. 10648-10651, 2011.

[121] K. K. Nanda, "Liquid-drop model for the surface energy of nanoparticles," *Physics Letters A,* vol. 376, pp. 1647-1649, 2012.

[122] F. Aqra and A. Ayyad, "Surface free energy of alkali and transition metal nanoparticles," *Applied Surface Science,* vol. 314, pp. 308-313, 2014.

[123] O. Glatter and O. Kratky, "Small angle X-ray scattering," : Academic Press, pp. 346-352, 1982.

[124] X. Guo, A. Gutsche, M. Wagner, M. Seipenbusch, and H. Nirschl, "Simultaneous SWAXS study of metallic and oxide nanostructured particles," *Journal of Nanoparticle Research,* vol. 15, p. 1559, 2013.

[125] I. Bakonyi, "Atomic volumes and local structure of metallic glasses," *Acta Materialia,* vol. 53, pp. 2509-2520, 2005.

[126] E. T. Teatum, K. A. Gschneidner, and J. T. Waber, "Compilation of calculated data useful in predicting metallurgical behavior of the elements in binary alloy systems," *Report LA-2345 Los Alamos scientific laboratory of the University of California,* p. 11, 1968.

[127] C. M. Wang, D. Wang, X. K. Mu, S. Goel, T. Feng, Y. Ivanisenko, H. Hahn, and H. Gleiter, "Surface segregation of primary glassy nanoparticles of $Fe_{90}Sc_{10}$ nanoglass," *Materials Letters,* vol. 181, pp. 248-252, 2016.

[128] V. V. Hoang and T. Odagaki, "Molecular dynamics simulations of simple monatomic amorphous nanoparticles," *Physical Review B,* vol. 77, p. 125434, 2008.

[129] V. V. Hoang, "Molecular dynamics simulation of liquid and amorphous Fe nanoparticles," *Nanotechnology,* vol. 20, p. 295703, 2009.

[130] V. V. Hoang and N. H. Cuong, "Local icosahedral order and thermodynamics of simulated amorphous Fe," *Physica B Condensed Matter,* vol. 404, pp. 340-346, 2009.

[131] V. V. Hoang and T. Q. Dong, "Free surface effects on thermodynamics and glass formation in simple monatomic supercooled liquids," *Physical Review B Condensed Matter,* vol. 84, p. 174204, 2011.

[132] V. V. Hoang, "Atomic mechanism of vitrification process in simple monatomic nanoparticles," *European Physical Journal D,* vol. 61, pp. 627-635, 2011.

[133] X. J. Liu, G. L. Chen, X. Hui, T. Liu, and Z. P. Lu, "Ordered clusters and free volume in a Zr–Ni metallic glass," *Applied Physics Letters,* vol. 93, p. 011911, 2008.

[134] D. Şopu, Y. Ritter, H. Gleiter, and K. Albe, "Deformation behavior of bulk and nanostructured metallic glasses studied via molecular dynamics simulations," *Physical Review B,* vol. 83, p. 100202, 2011.

[135] K. J. Laws, D. B. Miracle, and M. Ferry, "A predictive structural model for bulk metallic glasses," *Nature communications,* vol. 6, p. 8123, 2015.

[136] Y. Ritter and K. Albe, "Chemical and topological order in shear bands of $Cu_{64}Zr_{36}$ and $Cu_{36}Zr_{64}$ glasses," *Journal of Applied Physics,* vol. 111, p. 103527, 2012.

[137] M. Nageswararao, H. Herman, and C. J. Mcmahon, "On the decomposition of supersaturated Fe-Sb, Fe-Sn, and Fe-Sb-Ni solid solutions, " *Metal Science,* vol. 10, pp. 249-252, 1976.

[138] A. T. Dinsdale, "SGTE data for pure elements," *Calphad-computer Coupling of Phase Diagrams & Thermochemistry,* vol. 15, pp. 317-425, 1991.

[139] A. R. Miedema, P. F. De Châtel, and F. R. De Boer, "Cohesion in alloys - fundamentals of a semi-empirical model," *Physica B+C,* vol. 100, pp. 1-28, 1980.

[140] J. M. López and J. A. Alonso, "Semiempirical theory of solid solubility in metallic alloys," *Physica Status Solidi,* vol. 76, pp. 675-682, 1983.

[141] J. A. Alonso, L. J. Gallego, and J. A. Somoza, "Construction of free energy diagrams of amorphous alloys," *Il Nuovo Cimento D,* vol. 12, pp. 587-595, 1990.

[142] B. X. Liu, W. S. Lai, and Z. J. Zhang, "Solid-state crystal-to-amorphous transition in metal-metal multilayers and its thermodynamic and atomistic modelling," *Advances in Physics,* vol. 50, pp. 367-429, 2001.

[143] J. M. López and J. A. Alonso, "The atomic size-mismatch contribution to the enthalpy of formation of concentrated substitutional metallic solid solutions," *Physica Status Solidi,* vol. 85, pp. 423-428, 2010.

[144] S. Q. Xi, K. S. Zuo, X. G. Li, G. Ran, J. E. Zhou, "Study on the solid solubility extension of Mo in Cu by mechanical alloying Cu with amorphous Cr(Mo)," *Acta Materialia,* vol. 56, pp. 6050-6060, 2008.

[145] D. H. Kim, W. T. Kim, E. S. Park, N. Mattern, J. Eckert, "Phase separation in metallic glasses," *Progress of Materials Science,* vol. 58, pp. 1103-1172, 2013.

[146] H. Okamoto, "Fe-Sc (Iron-Scandium) ," *Journal of Phase Equilibria and Diffusion,* vol. 33, p. 80, 2012.

[147] T. Masumoto, H. Kimura, A. Inoue, and Y. Waseda, "Structural stability of amorphous metals," *Materials Science & Engineering,* vol. 23, pp. 141-144, 1976.

[148] T. Kulik, "Nanocrystallization of metallic glasses," *Journal of Non-Crystalline Solids,* vol. 287, pp. 145-161, 2001.

[149] F. Liu and R. Kirchheim, "Nano-scale grain growth inhibited by reducing grain boundary energy through solute segregation," *Journal of Crystal Growth,* vol. 264, pp. 385-391, 2004.

[150] F. Q. Guo and K. Lu, "Formation of a single α-Fe nanophase during mechanically driven crystallization of an FeMoSiB metallic glass," *Nanostructured Materials,* vol. 7, pp. 509-517, 1996.

[151] Z. Chen, F. Liu, X. Q. Yang, C. J. Shen, and F. Yu, "Analysis of controlled-mechanism of grain growth in undercooled Fe-Cu alloy," *Journal of Alloys & Compounds,* vol. 509, pp. 7109-7115, 2011.

[152] X. K. Mu, S. Neelamraju, W. Sigle, C. T. Koch, N. Totò, J. C. Schön, A. Bach, D. Fischer, M. Jansen, and P. A. V. Aken, "Evolution of order in amorphous-to-crystalline phase transformation of MgF_2," *Journal of Applied Crystallography,* vol. 46, pp. 1105-1116, 2013.

[153] Y. Shibuta and T. Suzuki, "A molecular dynamics study of the phase transition in bcc metal nanoparticles," *Journal of Chemical Physics,* vol. 129, p. 144102, 2008.

[154] M. Ghafari, H. Gleiter, T. Feng, K. Ohara, and H. Hahn, "Are transition metal-rich metallic glasses made up of distorted BCC clusters?," *Journal of Material Sciences & Engineering,* vol. 5, p. 1000299, 2016.

[155] A. Hirata and Y. Hirotsu, "Structure analyses of Fe-based metallic glasses by electron diffraction," *Materials,* vol. 3, pp. 5263-5273, 2010.

[156] S. P. Pan, S. D. Feng, J. W. Qiao, W. M. Wang, and J. Y. Qin, "Crystallization pathways of liquid-bcc transition for a model iron by fast quenching," *Scientific Reports,* vol. 5, p. 16956, 2015.

[157] T. Kulik, J. Ferenc, and H. Matyja, "Low temperature nanocrystallization of iron-based amorphous alloys," *Materials Science Forum,* vol. 235-238, pp. 421-426, 1997.

[158] Y. Waseda, H. Okazaki, and T. Masumoto, "Current views on the structure and crystallization of metallic glasses," *Journal of Materials Science,* vol. 12, pp. 1927-1949, 1977.

[159] X. L. Wang, J. Almer, C. T. Liu, Y. D. Wang, J. K. Zhao, A. D. Stoica, D. R. Haeffner, and W. H. Wang, "In situ synchrotron study of phase transformation behaviors in bulk metallic glass by simultaneous diffraction and small angle scattering," *Physical Review Letters,* vol. 91, p. 265501, 2003.

[160] X. J. Liu, G. L. Chen, X. D. Hui, H. Y. Hou, K. F. Yao, and C. T. Liu, "Growth mechanism from nano-ordered clusters to nanocrystals in a deeply undercooled melt of Zr-Ni-Ti metallic glass," *Journal of Applied Physics,* vol. 102, p. 145502, 2007.

[161] X. J. Liu, G. L. Chen, H. Y. Hou, X. Hui, K. F. Yao, Z. P. Lu, and C. T. Liu, "Atomistic mechanism for nanocrystallization of metallic glasses," *Acta Materialia,* vol. 56, pp. 2760-2769, 2008.

[162] K. F. Kelton, A. L. Greer, D. M. Herlach, and D. Holland-Moritz, "The Influence of order on the nucleation Barrier," *MRS Bulletin,* vol. 29, pp. 940-944, 2004.

[163] C. M. Wang, X. A. Guo, Y. Ivanisenko, S. Goel, H. Nirschl, H. Gleiter, H. Hahn, "Atomic structure of $Fe_{90}Sc_{10}$ glassy nanoparticles and nanoglasses," *Scripta Materialia,* vol. 139, pp. 9-12, 2017.

[164] A. R. Yavari, A. L. Moulec, A. Inoue, N. Nishiyama, N. Lupu, E. Matsubara, W. J. Botta, G. Vaughan, M. D. Michiel, and Å. Kvick, "Excess free volume in metallic glasses measured by X-ray diffraction," *Acta Materialia*, vol. 53, pp. 1611-1619, 2005.

[165] F. Spaepen, "Les Houches *Lectures* XXXV *on Physics of Defects*, " Amsterdam: North Holland Press, pp. 136-174, 1981.

[166] X. P. Tang, R. Busch, W. L. Johnson, and Y. Wu, "Slow atomic motion in Zr-Ti-Cu-Ni-Be metallic glasses studied by NMR," *Physical Review Letters*, vol. 81, p. 5358, 1998.

[167] F. E. Luborsky, ": Butterworths, pp. 160-162, 1983.

[168] Y. Zhang, K. Hono, A. Inoue, A. Makino, and T. Sakurai, "Nanocrystalline structural evolution in $Fe_{90}Zr_7B_3$ soft magnetic material," *Acta Materialia*, vol. 44, pp. 1497-1510, 1996.